

NUMERICAL MODELING OF RIVER MIGRATION INCORPORATING EROSIONAL
AND DEPOSITIONAL BANK PROCESSES

BY

ESTHER C. EKE

DISSERTATION

Submitted in partial fulfillment of the requirements
for the degree of Doctor of Philosophy in Civil Engineering
in the Graduate College of the
University of Illinois at Urbana-Champaign, 2013

Urbana, Illinois

Doctoral Committee:

Professor Gary Parker, Chair
Professor Marcelo H. Garcia
Professor Bruce Rhoads
Professor Jasim Imran, University of South Carolina
Professor David Mohrig, University of Texas at Austin

ABSTRACT

Understanding the nature of morphologic changes of meandering rivers has long attracted the attention of the scientific community, in the fields of fluvial geomorphology, hydraulic engineering and river restoration. Several meander evolution models developed over the years have provided a deeper insight into meander dynamics. In almost all these models however, a river width that remains constant in space and in time is imposed as a user-specified parameter, without any consideration of the processes that establish this width. Consistent width variation patterns found in most meandering rivers are largely ignored by these models. Perhaps even more importantly, the questions as to how river width is selected and how width variation interacts with meander evolution remain unanswered.

This dissertation implements a model framework for meander migration where both bank processes (erosion and deposition) are considered independently, interacting via the intervening channel. In this framework, bank erosion is modeled as erosion of purely non-cohesive bank material damped by natural armoring due to basal slump blocks and channel deposition is modeled as a function of vegetal encroachment. Since banks are allowed to move independently, channel width is allowed to vary locally as a result of differential bank migration. In this dissertation, a fully nonlinear depth-averaged iterative scheme with coupled flow and in-channel bed morphodynamics is developed and implemented so as to capture width variation. Both the migration model and the in-channel morphodynamics model have been coupled adopting a slow planform evolution approximation i.e. in-channel morphodynamics are assumed to be steady state at the time scale of planimetric evolution.

A series of numerical studies have been conducted across a wide range of cases, from the simplified case of a straight channel, to constant curvature bend flow, and then to a freely meandering river up to and beyond cut-off. The results show the general tendency for a channel to arrive at an equilibrium/quasi-equilibrium width from any initial width configuration, and delineate phase-plane trajectories for bank interaction which include bank push and bar pull. Co-evolution of local curvature, width and bed slope is demonstrated for the case of a freely meandering river and general metrics for predicting width variation patterns in meandering river systems are outlined. Simulations have been done with realistic field numbers and results are in general agreement with observed natural trends.

ACKNOWLEDGEMENTS

First of all, I would like to thank Almighty God for making all of this possible. For a minute there, I thought I would never graduate!

I would like to express profound gratitude to my advisor Prof Gary Parker for giving me the opportunity to be a part of this project. Thank you for all the guidance and support you have shown and for the many times that you have gone beyond the role of an advisor and have acted as a father figure to me. It has been a great pleasure working under you and I hope that I can be an inspiration to someone someday in the same way that you have been to me.

My research was wholly funded by the National Center for Earth-Surface Dynamics (NCED). I would like to acknowledge their financial support and also express gratitude for the opportunities provided through the support of the Center which included participation in Summer Institutes and workshops, participation in numerous international conferences, access to data and source code from other researchers as well opportunities to regularly interact and collaborate with fellow NCED-ians.

I would also like to thank our collaborators in Hokkaido University for their contributions to this research, in particular Professor Yasuyuki Shimizu, Professor Izumi and Kazutake Asahi. I am grateful for the opportunity to participate in the IRIC workshop held in the University of Illinois and also for the opportunity to visit Japan and share my work with other graduate students doing relevant research

I appreciate the guidance and support of my Ph.D. committee, Professor Marcelo H. Garcia, Professor Bruce Rhoads, Professor Jasim Imran and Professor David Mohrig.

I would like to give special thanks to my parents, Silas and Roli Eke for their constant prayers, my siblings Ngozi, Chidi and Chima, and my other brothers and sisters in Christ from ECWA Ayilara, Kings Assembly and the TCBC small group at the Offner's. You have all been a part of this journey from the beginning and I am grateful for all the support and prayers.

Finally, I have to specially thank my colleagues and friends who regularly had useful suggestions and ideas and who showed support in more ways than one: Enrica Viparelli, Tzu-Hao Yeh, Matthew Czapiga, Andrew Rehn, Chuan Li, Rossella Luchi, Alessandro Frascati, Davide Motta, John Sartori, Laide and Yemisi Lawal, Ifeyinwa Onyenekwu and Munirat Adebimpe. I cannot thank you guys enough.

PUBLICATIONS ARISING FROM THIS DISSERTATION

Paper submissions included in thesis

1. Eke, E.C, Parker, G., Shimizu, Y. 2013 Numerical modeling of erosional and depositional bank processes in migrating river bends with self-formed width: morphodynamics of bar push and bank pull, Journal of Geophysical Research, submitted. (Chapter 2)
2. Eke, E.C, Parker, G., Sun, T., Imran, J., Shimizu Y. 2013 Co-evolution of width and sinuosity in meandering rivers, Journal of Fluid Mechanics, submitted. (Chapter 3)
3. Eke, E.C, Parker, G, Imran, J., Yi, A 2013 Long term evolution of meandering rivers with width variation. (Chapter 4)

Paper submissions relevant to thesis but not forming part of it

1. Li, C., Czapiga, M. J., Eke, E. C., Viparelli, E. and Parker G. 2013, River bankfull geometry: Shear velocity is viscosity-dependent but grain size-independent, Nature Geosciences, submitted. (included in Appendix B)

Conference publications and abstracts arising from dissertation research

1. Eke, E., Parker G., 2010. Meander migration modeling accounting for the effect of riparian vegetation. Abstract, AGU Fall meeting, San Francisco, California, Dec. 13-17.

2. Eke, E., Parker G., 2011. Meander migration modeling with the incorporation of erosional and depositional bank processes. Abstract, EWRI Conference, ASCE, Palm Springs, May 22-26.
3. Eke E., Shimizu Y., Parker G., 2011. Numerical modeling of meander migration incorporating erosional and depositional bank processes. Proceedings, River, Coastal and Estuarine Morphodynamics Conference, Beijing, China, September 6 – 8
4. Eke, E., Shimizu, Y., Parker, G., 2011. Theoretical and numerical modeling of river meander migration with freely-adjustable width. Abstract, GSA annual meeting, Minneapolis, Minnesota, October 9-12.
5. Parker G., Eke E., 2011. Hydraulic geometry of meandering, alluvial and sand-bed streams: the roles of washload, vegetation and natural bank armoring. Abstract, AGU Fall meeting, San Francisco, California, Dec. 5-9.
6. Parker, G., Eke E., Asahi K., Shimizu Y., Nelson J., 2012. Vegetal encroachment on point bar deposits as a control on width variation in meandering rivers. Abstract, AGU Fall meeting, San Francisco, California, Dec. 3-7.
7. Eke, E., Parker G., 2013. Numerical modeling of alluvial river migration: understanding the evolution of width. Abstract, EWRI Conference, ASCE, Cincinnati, May 19-23.

TABLE OF CONTENTS

Chapter 1 INTRODUCTION.....	1
1.1 Research Motivation	1
1.2 Research Objective	3
1.3 Thesis Structure	4
Chapter 2 NUMERICAL MODELING OF EROSIONAL AND DEPOSITIONAL BANK PROCESSES IN MIGRATING RIVER BENDS WITH SELF-FORMED WIDTH: MORPHODYNAMICS OF BAR PUSH AND BANK PULL	5
2.1 Introduction.....	6
2.2 The Bank Model Shock Condition	11
2.3 Relation for Bank Erosion	14
2.4 Relation for Bank Deposition	25
2.5 Formative Shields Number and Bankfull Geometry	27
2.6 Nonlinear in-channel morphodynamic model	31
2.7 Channel evolution in time	39
2.8 Model Implementation.....	42
2.9 Discussion.....	51
2.10 Conclusions.....	53
Tables	57
Figures	59
Chapter 3 COEVOLUTION OF WIDTH AND SINUOSITY IN MEANDERING RIVERS.....	76
3.1 Introduction.....	77
3.2 Observed patterns of width variation in meandering rivers	82
3.3 Width of an equivalent straight channel: bankfull geometry	87

3.4	Model formulation for a meandering channel	91
3.5	Numerical Experiments	108
3.6	Discussion.....	125
3.7.	Conclusions.....	128
	Tables	131
	Figures	134
Chapter 4 LONG TERM EVOLUTION OF MEANDERING RIVERS WITH WIDTH VARIATION		157
4.1.	Introduction.....	157
4.2	River migration modelling incorporating river width adjustment	161
4.3	Long term meander evolution incorporating channel width adjustment	165
4.4	Width adjustment in response to a cut-off	169
4.5	Conclusions.....	171
	Figures	174
Chapter 5 CONCLUSIONS AND FUTURE WORK		184
REFERENCES		188
Appendix A: NONLINEAR FLOW MODEL SOLUTION.....		209
Appendix B: RIVER BANKFULL GEOMETRY: SHEAR VELOCITY IS VISCOSITY-DEPENDENT BUT GRAIN SIZE-INDEPENDENT		215

Chapter 1

INTRODUCTION

1.1 Research Motivation

Meandering rivers are perhaps one of the more common channel forms; so common that they exist in many environments from alluvial environments to incisional bedrock and glacial meltwater systems. Even in submarine systems, turbidity currents form gigantic meandering channels on submarine fans at the base of the continental slope (Imran et al, 1999). Understanding the morphology and evolution of meandering rivers is an undertaking of interest to the scientific community and of great practical importance particularly for the urban planner, the bridge designer and local landowners with farmlands that fall within meander belts. The study of meandering has proved invaluable to the oil and gas industry in understanding the porosity distribution in reservoir formations created by ancient meandering systems (Henriquez et al, 1990) and has also offered invaluable insight to stream restoration and river re-meandering efforts.

Scientific interest in meandering rivers has existed for a long time (e.g. Einstein, 1926), and a considerable amount of effort has been made towards provide a mechanistic framework for the quantitative determination of many key parameters in meander development. These efforts have led to the development of models that establish the intrinsic ability of meander trains to evolve from incipient meander formation to neck cutoff.

The standard model for meander migration links the rate of channel shift to in-channel hydrodynamics through an erosion law. The most commonly used law is that presented by

Hasegawa (1977) and Ikeda et al (1981) commonly known as the HIPS model. The HIPS model, though frequently used, suffers from the lack of a physical basis which makes calibration tedious. In addition, the model explicitly assumes a spatially and temporally constant river channel width; providing no information on how this width is obtained and largely ignoring field observations which clearly show that channel width is not spatially constant in most natural rivers (Brice, 1982 and Lagasse et al., 2004). Recent research efforts have begun to quantify the effect of width variation in meandering rivers (e.g. Luchi et al, 2011) but the question on how to quantitatively describe and predict the spatial and temporal width variation patterns found in nature still remains.

In this study, we attempt to provide a more physically based approach to modelling bank migration which can answer the question on how a river chooses its width. Local channel width is determined as a balance between erosional and depositional bank processes, so that channel widening is characterized by net erosion and channel narrowing by net deposition. An understanding of the co-evolution of meander planform and width variation must, then be predicated on a deeper understanding of the processes of both bank erosion and deposition.

There is extensive literature geared towards understanding the processes of bank erosion (e.g. Darby and Thorne, 1996; Darby et al., 2007; Langendoen and Simon, 2008) and significant effort has been invested into qualitatively describing bank encroachment and the impact of vegetation on planform dynamics and vice versa (e.g. Perucca et al, 2005,2007; Allmendinger et al 2005). However, little effort has been made to incorporate these findings into a framework that can be applied directly to two-dimensional models of long term meander migration.

1.2 Research Objective

The research objective, therefore, is to develop a generalized numerical framework for meandering rivers that more realistically incorporates both bank erosion and bank deposition processes in predicting channel planform evolutionary patterns. In this study, we present a simplified approach to capture both bank processes independently; channel erosion as the migration of a purely cohesionless channel bank damped by natural armoring such as the basal slump blocks (e.g. Parker et al, 2011 and Dulal et al., 2010) and channel deposition as a function of vegetation encroachment and sediment trapping. In developing and applying this generalized framework, we shed some light on certain key research questions:

- *How can one quantitatively describe bank erosion/deposition?*

In this study, we outline simple models to describe bank process and we are able to describe bank-to-bank interaction, including the processes of bank pull and bar push.

- *How do we establish the river equilibrium width and what does it look like?*

In this study we consider the case of the straight channel, the spatially constant curvature bend and the freely meandering river and show that “equilibrium” can range from a definite value for a straight channel, to an asymptotic state for a simple bend where width very slowly declines in time to a statistical equilibrium which is established through a balance between channel narrowing during channel elongation and channel widening during cut-offs.

- *What are the necessary and sufficient conditions under which channels may develop towards the pattern of width variation observed in nature?*

For a given river system with a known discharge and sediment supply, we show systematic trends that describe tendencies in width variation and to assess key parameters in determining these tendencies.

1.3 Thesis Structure

This thesis has been structured as a series of journal manuscripts. Each chapter is a separate manuscript which has either been submitted or is in preparation. The articles have been organized here-in to show a logical progression of the research from the development of the model framework to its application to systems of progressively increasing complexity. In Chapter 2, we develop a complete formulation for channel bank erosion and deposition. In order to clearly delineate the interaction between channel migration and width selection, application of the model is restricted to spatially constant-curvature bend flow. The case of a straight channel is recovered as centerline curvature becomes vanishing. In Chapter 3 we extend the model application to a simplified periodic channel to focus is on studying the spatial and temporal coevolution of width and sinuosity in meandering rivers. Chapter 4 applies the model to long term evolution simulations involving multiple cut-offs to study the behavior during and after cut-off and to examine planform evolution towards statistical equilibrium. General conclusions and future work are presented in Chapter 5, Appendix A contain the nonlinear flow model solution and Appendices B contains a paper submission relevant to the thesis but in which I am not the primary co-author.

Chapter 2

NUMERICAL MODELING OF EROSIONAL AND DEPOSITIONAL BANK PROCESSES IN MIGRATING RIVER BENDS WITH SELF-FORMED WIDTH: MORPHODYNAMICS OF BAR PUSH AND BANK PULL

Abstract

Meandering rivers display active communication between bank erosion and bank deposition processes. How does this occur? How does the river select its width? To answer these questions, we implement a model for meander migration where both bank processes (erosion and deposition) are considered independently, interacting via the intervening channel. Bank erosion is modeled as erosion of purely non-cohesive bank material damped by natural slump block armoring; channel deposition is modeled via flow-retarded vegetal encroachment. Both processes are tied to a slope-dependent channel forming Shields number; banks with near-bank Shields number below this value undergo deposition, and those above it undergo erosion. Channel-forming Shields number must increase with slope, as dictated by available data and model performance. The model is coupled with a nonlinear flow and bed morphodynamic model, and is applied to the simplified cases of a straight channel, and a channel bend with spatially constant but temporally varying curvature. Straight channel modeling shows that a channel arrives at an equilibrium width from any initial condition. The model was implemented for a bend under the constraint of constant centerline elevation difference over the reach. Under this constraint, the river always approaches an asymptotic state where width reduces slowly in time and where bank erosion and deposition

occur at nearly equal rates. Before this state is reached, however, the river follows a phase-plane trajectory with four possible regimes: a) both banks erode, b) both banks deposit, c) both banks migrate outward, but with a faster depositing inner bank (bar push), and d) both banks migrate outward, but with a faster eroding outer bank (bank pull). The trajectory of migration on the phase plane, including bar push and bank pull, depends on initial conditions (overwide or overnarrow channel) and two parameters, one controlling the rate of depositional migration and the other controlling the rate of erosional migration. All input parameters have specific physical meaning, and the potential to be measured in the field. The model is applied to conditions for a reach of the Vermillion River, Minnesota, USA. It is easily generalized to the evolution of fully meandering rivers.

2.1 Introduction

What can be characterized as the standard model for meander migration describes the spatial-temporal development of the river planform in terms of a nonlinear integro-differential equation that specifies migration speed normal to channel centerline (Seminara et al., 2001, Seminara, 2006). An erosion rule is used to relate this migration speed to near-bank hydrodynamics. The bank erosion law in most existing models is either that proposed by Hasegawa (1977) and Ikeda, Parker and Sawai (1981), i.e. the HIPS model as defined in Parker et al. (2011), or some variation. In the HIPS model, the local value of the rate of channel shift is determined by the flow field perturbation evaluated near the banks using the relation:

$$\dot{y} = E\Delta U \quad (2.1)$$

where U denotes half the streamwise velocity difference between the two banks, and E is a dimensionless coefficient. In this formulation, the streamwise velocity in question is a near-bank value that is evaluated just outside of the flow field constituting the bank boundary layer. This simple but useful model has been extensively used, and remains in use by many researchers today (e.g. Frascati and Lanzoni, 2010). The major issues with the HIPS formulation are twofold. (1) The lack of a physical basis for the coefficient E makes it impossible to estimate its value except through calibration with field data (e.g. Abad and Garcia, 2006). To this end, there have been extensive research efforts which have almost exclusively focused on modeling the relevant biogeotechnical properties of bank erosion (e.g. Darby and Thorne, 1996; Darby et al., 2007; Langendoen and Simon, 2008) These findings have on occasion, been directly applied to meander migration models (e.g. Mosselman, 1998; Darby et al., 2002; Rinaldi et al, 2008; Duan and Julien, 2010; Motta et al., 2012). (2) The explicit assumption of a constant river channel width makes it impossible to predict channel widening, chute cutoffs and the general width variation patterns observed in nature (Parker et al., 2011). This systematic variation in width has been documented by Brice (1982), Lagasse et al. (2004) and more recently characterized by Peyret (2011) and Zolezzi et al. (2012).

Change in local channel width is determined as a balance between erosional and depositional bank processes, so that channel widening is characterized by net erosion and channel narrowing by net deposition. The rate of bank erosion is controlled by a number of factors such as cohesive bank properties, root character and density of the adjacent floodplain and the breakdown or removal of slump blocks or other natural armoring along the banks (e.g. tree stumps) (Thorne, 1990; Stott, 1997; Micheli and Kirchner 2002). In streams with vegetated floodplains, bank

deposition is commonly (but not universally; see Matsubara et al., 2012) associated with sediment trapping by vegetation encroaching from the active floodplain onto e.g. a point bar, so stabilizing the deposit (e.g. Tal and Paola, 2010, Braudrick et al., 2009). The rates of bank erosion and deposition, which can vary widely along a meandering reach, are influenced by curvature, local differences in bank properties and in the density of vegetation on the floodplain (e.g. Hooke, 1980; Pizzuto, 1994; Stott, 1997).

2.1.1 Runaway bank erosion and the need for natural armoring

The necessity for some sort of bank protection, particularly in alluvial systems, has been underlined by the failure to generate single-thread, high-amplitude meandering channels in purely cohesionless sand-rich floodplains at laboratory scale. Such systems are unable maintain single thread channels, as shown in figure 2 of Parker (1976), and eventually become braided channels over time. This widening to a braided state is caused by a process that we term “runaway widening”, by which an eroding bank retreats far faster than the opposite bank can advance. This process is illustrated more specifically below. Successful generation of relatively high-sinuosity, single-thread meandering channels in otherwise cohesionless sand in the laboratory has been attained only with the use of cohesive material (Smith, 1998; Dulal and Shimizu, 2010, van Dijk et al, 2013), or model vegetation consisting of live alfalfa sprouts. (Tal and Paola, 2010; Braudrick et al, 2009). Cohesive material or vegetation did not stop erosion in these experiments, but rather moderated it to the point that runaway widening did not occur.

In many alluvial rivers, the structures of floodplain deposits can be simplified to a lower non-cohesive layer emplaced by the incorporation of point bar material in the floodplain as the

channel migrates, and an upper, “cohesive” layer including fine-grained overbank deposits and vegetal roots (Figure 2.1). Runaway widening is prevented by a) natural armoring of the non-cohesive toe of an eroding bank by slump blocks, root wads, or sediment induration, and b) vegetal encroachment onto point bars. The former mechanism ensures that an eroding bank does not erode too fast, and the latter mechanism enables coherent migration of a depositing bank. The model presented here focuses on the two mechanisms of slump block armoring and vegetal encroachment.

2.1.2 Slump blocks as a natural armoring mechanism

Slump blocks are chunks of failure material typically scattered along the base of the eroding bank, often near bend apexes where near-bank flow velocities are high. They are produced via cantilever or rotational failure when the lower, cohesionless part of the river bank is fluvially eroded and the upper, cohesive layer is thus compromised. Several studies have documented the existence of these slump blocks (Thorne and Lewin, 1979; Murgatroyd and Teran 1983; Stott, 1997; Evans and Warburton 2001, Micheli and Kirchner 2002) and have indicated that these failed blocks provide bank protection by both consuming and diverting flow energy that may otherwise be available to scour the lower bank region (Wood et al., 2001). This creates a semi-stable state where further bank retreat is reliant on the removal of basal accumulation of slump block material by high flow events (Thorne and Tovey, 1981). Studies have also shown that these individual slump blocks can persistently provide protection over many years (Micheli and Kirchner, 2002). However, much of the documentation has consisted of qualitative descriptions, and relatively little has been done to quantify their effectiveness as natural armoring against fluvial erosion.

2.1.3 The role of vegetation in lateral bank accretion

The effects of floodplain vegetation on river morphodynamics can be seen at all spatial scales. In particular, at the cross-sectional scale, floodplain vegetation causes deflection of the main flow towards the center of the main channel (Tsujiimoto, 1999), enhances bank advance (Hupp and Simon, 1991; Gurnell et al., 2006) and reduces bank retreat, leading to width reduction, (Eschner et al., 1983; Beeson and Doyle, 1995; Huang and Nanson, 1997; Simon and Collison, 2002; Allmendinger et al., 2005). With regard to lateral deposition, vegetation acts in two ways: to provide a nucleus for sediment trapping (Hickin, 1984); and to stabilize non-cohesive sediment that has deposited on e.g. a point bar. Although effort has been invested into qualitatively describing bank encroachment and the impact of vegetation on planform dynamics and vice versa (Perucca et al, 2005,2007; Allmendinger et al 2005), these findings have not yet been incorporated into a framework that can be applied directly to two-dimensional models of long term meander migration.

2.1.4 Modeling of bend migration with channel width variation

This paper implements the recently proposed framework presented in Parker et al. (2011), in which a meandering river selects its own width as it migrates. In the framework of Parker et al. (2011), width selection is achieved by means of a balance between erosional and depositional bank processes. This work goes beyond the original framework by proposing specific parameterizations for the bank erosion model and by specifying a closure relationship to capture deposition processes. It builds on a joint research effort including the work of Dulal et al. (2010), Eke et al. (2011), Parker et al. (2012) and more recently by Asahi et al. (submitted).

In order to clearly delineate the interaction between channel migration and width selection, application of the model is restricted to spatially constant-curvature bend flow herein. The case of a straight channel is recovered as centerline curvature becomes vanishing. Model parameters are loosely constrained using data from selected river reaches. The analysis presented here thus represents a first but major step toward the modeling of migration-width interaction in fully meandering rivers.

2.2 The Bank Model Shock Condition

The framework presented in Parker et al (2011) divides the river cross-section into 3 distinct regions: a central channel region and two bank regions, as shown in figure 2.2. The central channel region at a meander bend is defined as the region between the deepest portion of the channel (i.e. the thalweg) and the tip of the active point bar. By active point bar, we refer to the portion of the convex bar where active transport occurs under formative (bankfull) conditions. This definition corresponds to the outer convex bar of Goodwin and Steidtmann (1981). The convex inner bank is the fairly steep region between the active point bar and the vegetation line, also referred to as the inner accretionary bank (see Bluck, 1971; Campbell and Hendry, 1987; Page et. al, 2003). The concave inner bank is more clearly defined as the region between the thalweg and the vegetation line.

A simplified cross-section is adopted, as shown in figure 2.3, in which the non-cohesive bank regions have specified constant transverse bank slopes, and the overlying cohesive layer is of uniform thickness and properties. The tilde superscript here indicates dimensioned parameters. Note that this notation does not specify whether a bank is migrating toward or away from the

channel centerline; this is determined internally by the model as outlined below. It suffices to note that the bank region corresponds to an inner accretionary bank in the former case, and a cut bank in the latter case.

As outlined in Parker et al (2011), we can describe the morphodynamics of bank regions in terms of a simplified “shock” condition based on an integral approach (e.g. Swenson, 2002). This approach involves integrating the 2D non-steady conservation of sediment transport equation over the bank region i.e. from $\tilde{n} = \tilde{n}_{t,j}$ to $\tilde{n} = \tilde{n}_{T,j}$ while simplifying the complexities of the shape of the bank region to a specified constant transverse signed bank slope $S_{s,j}$ such that the bed elevation along the bank is defined as:

$$\tilde{y}_{b,j}(\tilde{n}, \tilde{t}) = \tilde{y}_{bT,j} + S_{s,j} (\tilde{n} - \tilde{n}_{t,j}(\tilde{t})) \quad (2.2)$$

where the subscript “j” indicates the equation can refer to either the left or right bank (j = LB or RB), subscript “t” refers to the bank toe or bed region adjacent to the bank, and the subscript “T” refers to the top of the non-cohesive layer as shown in figure 2.3 (see Parker et al., 2011 as well as Eke et al, 2011 for details). The resulting general form for bank migration given as

$$\frac{\partial \tilde{n}_{t,j}}{\partial \tilde{t}} \equiv \dot{n}_j = \frac{1}{(S_{s,j} + S_{st,j})} \left[\frac{\frac{\partial}{\partial \tilde{s}} \left(\int_{n_{t,j}}^{n_{r,j}} \tilde{q}_{sb,j} d\tilde{n} \right) - \tilde{q}_{fb,j} (1 + \tilde{n}_{t,j} \tilde{C})}{\tilde{B}_{b,j} (1 + \bar{n}_j \tilde{C}) (1 - \}_{pb,j})} + \frac{\partial \tilde{y}_{b,j}}{\partial \tilde{t}} \Big|_{\tilde{n}=\tilde{n}_{t,j}} \right] \quad (2.3)$$

Where

$$S_{st,j} = \frac{\mathfrak{D}\tilde{y}_b}{\mathfrak{D}\tilde{n}} \Big|_{\tilde{n}=\tilde{n}_{t,j}} ; \quad \tilde{B}_{b,j} = \tilde{n}_{T,j} - \tilde{n}_{t,j}; \quad \bar{n}_j = \frac{1}{2}(\tilde{n}_{T,j} + \tilde{n}_{t,j}) \quad (2.4)$$

Here \tilde{C} is the dimensioned local curvature, \tilde{t} is time, \tilde{s} is the streamwise coordinate, $\beta_{b,j}$ is the porosity of the non-cohesive bank sediment, $\tilde{q}_{sb,j}$ is the longitudinal sediment transport of non-cohesive material within the bank region and $\tilde{q}_{fb,j}$ is the transverse transport rate of non-cohesive sediment at the junction of the bank and bed regions i.e. $\tilde{q}_{fb,j} = q_{nb,j} \Big|_{\tilde{n}=\tilde{n}_{t,j}}$. Hence the normal velocity of the toe of the bank (i.e. the bank migration rate) is related to the rate of bed aggradation/degradation, longitudinal gradient of sediment transport rate and transverse sediment transport rate, all evaluated at the junction, and channel geometry. As shown in figure 2.3, the transverse coordinate \tilde{n} is defined as increasing towards the right bank, so that at the toe of the left bank $\tilde{n} = \tilde{n}_{t,LB} = -\tilde{b}(\tilde{t})$, and at the toe of the right bank $\tilde{n} = \tilde{n}_{t,RB} = \tilde{b}(\tilde{t})$, where \tilde{b} is the half-channel width.

We can simplify equation (2.3) by assuming $S_{s,j} \gg S_{st,j}$ (slope of the bank region is much larger than the slope of the bed region adjacent to the bank) and neglecting the streamwise variation of the bank-integrated streamwise non-cohesive sediment transport. The latter assumption is justified based on the tendency for slump blocks (eroding bank) or encroaching vegetation (accreting bank) to hinder the downstream transport of non-cohesive sediment. Thus, the integral condition for channel migration simplifies to:

$$\begin{aligned}
\dot{n}_j &= \frac{-\tilde{q}_{fb,j} (1 + \tilde{n}_{t,j} \tilde{C})}{\tilde{H}_{b,j} (1 + \tilde{n}_j \tilde{C}) (1 - \beta_{pb,j})} + \frac{1}{S_{s,j}} \left. \frac{\partial \tilde{y}_{b,j}}{\partial \tilde{t}} \right|_{\tilde{n}=\tilde{n}_{t,j}} \\
&= \tilde{r}_{E/D} + \frac{1}{S_{s,j}} \left. \frac{\partial \tilde{y}_{b,j}}{\partial \tilde{t}} \right|_{\tilde{n}=\tilde{n}_{t,j}}
\end{aligned} \tag{2.5}$$

The first term on the RHS of the above equation represents channel migration as a result of sediment transport toward the channel center (erosion) or away from it (deposition), which we here relate to the flow field at or near the channel bank, while the second term represents channel migration due to net aggradation or degradation of the channel bed near the bank toe. Quantification of the first term must be done differently depending on whether the bank is eroding or depositing. We propose sample relations for bank erosion and deposition in the following sections. Our relations are defined such that the model of migration itself determines whether a bank is eroding and depositing, without external specification.

2.3 Relation for Bank Erosion

The framework according to Parker et al (2011) specifies a closure for bank erosion in terms of a default transverse removal based on the assumption of purely non-cohesive, loose bank sediment by bedload transport, and with this default removal rate damped by natural armoring due to slump blocks (see figure 2.3). Thus, the transverse bedload supply rate of non-cohesive sediment from the eroding bank $\tilde{q}_{fb,E}$ is taken to be equal to the supply rate estimated for a purely noncohesive bank $\tilde{q}_{nnon,E}$, damped by a multiplicative armoring coefficient $K_{armor} \leq 1$ modeled as a function of slump block characteristics;

$$\tilde{q}_{fb,E} = K_{armor} \tilde{q}_{nnon,E} \tag{2.6}$$

The effective erosion rate for the said bank is given as follows;

$$i_{\sim E} = K_{armor} I_f i_{\sim non,E} \quad (2.7)$$

$$i_{\sim non,E} = - \frac{1}{(1 - \beta_{pb,E})} \frac{\tilde{q}_{mon,E} (1 + \tilde{n}_{t,E} \tilde{C})}{\tilde{H}_{b,E} (1 + \tilde{n}_E \tilde{C})} \quad (2.7b)$$

In the above relations the subscript ‘‘E’’ denotes the eroding bank and I_f is a flood intermittency factor corresponding to an estimate of the fraction of time that the river is morphodynamically active. The non-cohesive bedload supply from the eroding bank is modeled by a linear dependence on the local bed slope i.e.

$$\tilde{q}_{mon,E} = \Phi_b S_b S_{s,E} \sqrt{Rg \tilde{D}_s} \tilde{D}_s \quad (2.8)$$

where Φ_b is the dimensionless streamwise bedload intensity (Einstein number) along the bank, here estimated using the approximation of the original bedload transport relation of Einstein (1950) due to Parker (1979);

$$\Phi_b = 11.2 (\tau_{b,E}^*)^{1.5} \left[1 - \frac{\tau_c^*}{\tau_{b,E}^*} \right]^{4.5} \quad (2.9)$$

and

$$S_b = \frac{1 + \tilde{S}_{\sim}}{\sim} \sqrt{\frac{\tau_c^*}{\tau_{b,E}^*}} \quad (2.10)$$

Also μ = Coulomb friction coefficient, C_L = lift coefficient and $\tau_c^* = 0.03$ is the critical value of the Shields number at the threshold of motion. The above formulation is due to Parker (1979); similar but alternative relations are given in Garcia (2008). The bank Shields number $\tau_{b,E}^*$ is take to be a fraction of Shields number acting on the bed immediately adjacent to the bank i.e.:

$$\tau_{b,E}^* = \{ \tau_s^* \}_{\bar{n}=\bar{n}_{r,j}} \quad (2.11)$$

where τ_s^* is the streamwise Shields number, defined in the channel region and $\{$ is an order-1 dimensionless parameter which typically varies between 0.40 and 0.80 (e.g., Lane, 1955). This assumption is due to the absence of a submodel for bank shear stress in the present model.

2.3.1 Runaway bank erosion

To illustrate the need for an armor coefficient, we consider the case of a straight channel with purely non-cohesive banks. In such a case, the armor factor $K_{armor} = 1$ and the mean annual erosion rate is effectively

$$\tilde{i}_E = I_f \tilde{i}_{non,E} \quad (2.12)$$

where $\tilde{i}_{non,E}$ is calculated according to (2.8) – (2.11). We present sample calculations for three rivers to show that in the absence of some kind of natural armoring, the migration rate of a *straight* bank due to bank erosion would be substantially greater than is actually *observed at bends* of the rivers.

The rivers in question are the Vermillion River near Empire, Minnesota, USA (Lauer and Parker, 2008); the Trinity River near Dayton Lakes, Texas, USA (Peyret, 2011); and the Wabash River near Grayville, Illinois, USA (Konsoer et al., 2012). The bankfull characteristics of these reaches, i.e. bankfull discharge \tilde{Q}_{bf} , bankfull width \tilde{B}_{bf} , bankfull depth \tilde{H}_{bf} and bankfull Shields number \dagger_{bf}^* , along with bed slope S , characteristic bed material size \tilde{D}_s are given in Table 2.1. Also included for each reach is an estimate of the flood intermittency I_f was (somewhat arbitrarily but for the sake of illustration) estimated as the fraction of time that the river was above 55 percent of bankfull flow. The parameter $i'_{non,E,s}$ in Table 2.1 corresponds to the unprotected erosion rate computed from (12) assuming a straight reach. For conservative estimates, we have here assumed the bank porosity $\}_{pb} = 0.3$, $\{ = 0.6$ and the channel bank side slope $S_s = 1$ (45°). The parameter $i'_{E,obs,bend}$ corresponds to a characteristic observed, high bank migration rate near one or more bend in the reach. It is seen from the table that the ratio $i'_{non,E,s} / i'_{E,obs,bend}$ takes the respective values 103, 47 and 6.3 for the Vermillion River, Trinity River and Wabash River.

In the absence of any form of armoring, the rates of bank erosion predicted in *straight reaches* would be 1 to 2 orders of magnitude higher than the values *observed near the outside of bends*. It is this feature that we refer to as runaway bank erosion, and it is also why a bank armoring coefficient is necessary to moderate bank erosion. In the next section, we propose a parameterization of this armor factor as a function of slump block characteristics.

2.3.2 Quantifying an armoring coefficient

A formulation for quantifying K_{armor} was outlined in Parker et al, (2011), where the armor factor K_{armor} is related to the extent of slump block cover as follows:

$$K_{armor} = \text{Fcn} \left(\frac{\tilde{A}_c}{\tilde{D}_c \tilde{B}_{bw,E}} \right) \quad (2.13)$$

Here, \tilde{A}_c is the volume per unit length of slump block material armoring the bank region, \tilde{D}_c is a characteristic size of the slump blocks and

$$\tilde{B}_{bw,E} = \tilde{H}_{b,E} \sqrt{1 + (S_{s,E})^{-2}} \quad (2.14)$$

is the arc width of the zone available to be covered by slump blocks (Figure 2.4). In (2.14), $\tilde{H}_{b,E}$ is the height of the non-cohesive layer of the eroding bank from the thalweg to the bottom of the cohesive layer and $S_{s,E}$ is side slope of the non-cohesive layer of the eroding bank (Figure 2.4). In the idealized case of cubical blocks completely tiling the bank, \tilde{A}_c would be equal to $\tilde{D}_c \tilde{B}_{bw,E}$. In (2.13), Fcn denotes an as yet unevaluated function, but which can be expected to have the properties:

$$\begin{aligned} K_{armor} &\rightarrow 1 \quad \text{as} \quad \frac{\tilde{A}_c}{\tilde{D}_c \tilde{B}_{bw,E}} \rightarrow 0 \\ K_{armor} &\rightarrow 0 \quad \text{as} \quad \frac{\tilde{A}_c}{\tilde{D}_c \tilde{B}_{bw,E}} \rightarrow | \end{aligned} \quad (2.15)$$

where $|$ would be unity for perfect brick-shaped tiling.

The precise form of (2.13) is not known, but in the absence of detailed analysis, a linear relationship for F_{cn} is proposed here as the simplest formulation that quantifies the phenomenon of slump block armoring: $\beta = 1$, and

$$K_{armor} = 1 - \frac{\tilde{A}_c}{\tilde{D}_c \tilde{B}_{bw,E}} \quad (2.16)$$

Slump block armor is created by erosion of the non-cohesive material in the lower layer of figure 2.4 as the channel migrates, a process which causes pieces of the cohesive layer to fail onto it. The production rate of slump block volume per unit streamwise distance is thus given as

$$\tilde{q}_c = \tilde{H}_{c,E} \left| \tilde{\tau}'_E \right| (1 - \beta_{pc,E}) \quad (2.17)$$

where $\tilde{H}_{c,E}$ is the thickness of the cohesive layer at the eroding bank and $\beta_{pc,E}$ denotes the porosity of the cohesive material. It is assumed here that slump block volume decreases in situ by decay or transport and subsequent disintegration. Letting \tilde{T}_c denote a characteristic slump block residence time, the time rate of change of slump block volume per unit streamwise distance can be expressed in terms of the difference between the rate of slump block production and the rate of slump block decay i.e.,

$$\frac{d\tilde{A}_c}{d\tilde{t}} = \tilde{q}_c - \frac{\tilde{A}_c}{\tilde{T}_c} = \tilde{H}_{c,E} \left| \tilde{\tau}'_E \right| (1 - \beta_{pc,E}) - \frac{\tilde{A}_c}{\tilde{T}_c} \quad (2.18)$$

For practical purposes, we consider herein the quasi-equilibrium case where the processes delivering cohesive material to the base and removing it from there are in balance, so that $\frac{d\tilde{A}_c}{dt} = 0$

. We then find that

$$\tilde{A}_c = \tilde{H}_{c,E} |i'_E| (1 - \beta_{pc,E}) \tilde{T}_c \quad (2.19)$$

and thus,

$$K_{armor} = 1 - \frac{\tilde{H}_{c,E} |i'_E| (1 - \beta_{pc,E}) \tilde{T}_c}{\tilde{D}_c \tilde{B}_{bw,E}} \quad (2.20)$$

Substituting (2.20) into (2.7) and rearranging, the erosion rate is given as follows:

$$i'_E = \frac{I_f |i'_{non,E}|}{\left(1 + \frac{\tilde{H}_{c,E} (1 - \beta_{pc,E}) \tilde{T}_c |i'_{non,E}|}{\tilde{D}_c \tilde{B}_{bw,E}} \right)} \quad (2.21)$$

$$i'_E = \frac{I_f |i'_{non,E}|}{\left(1 + \frac{1}{u} \right)}, \quad u = \frac{\tilde{D}_c \tilde{B}_{bw,E}}{\tilde{H}_{c,E} (1 - \beta_{pc,E}) \tilde{T}_c |i'_{non,E}|} \quad (2.21a,b)$$

The case of the erosion of purely non-cohesive bank material is recovered from (2.21) by setting $\tilde{T}_c = 0$.

Scale estimates suggest that in general, u can be expected to be a small compared to unity as long as \tilde{T}_c is on the order of a year or more. This is illustrated in figure 2.5, based on the case of the Vermillion River near Empire, Minnesota, USA. The inputs to the computation are as follows:

$i_{non,E}^{\sim}$ is estimated as $i_{non,E,s}^{\sim}$ from table 2.1, \tilde{D}_c , $\tilde{H}_{c,E}$, $\}_{pc,E}$ and $S_{s,E}$ are estimated from the parameters given in table 2.2 (replace the subscript “LB” or “RB” with “E”), and $\tilde{B}_{bw,E}$ is computed from (2.14). For this case, $u = 0.04$ for $\tilde{T}_c = 1$ year. Thus under the assumption $u \ll 1$, (2.21) can be reduced to the form:

$$i_E^{\sim} = \frac{\tilde{D}_c \tilde{B}_{bw,E}}{\tilde{H}_{c,E} (1 - \}_{pc,E}) \tilde{T}_c} \text{sgn}(i_{E,non}^{\sim}) \quad (2.22)$$

This case corresponds to the rate of migration of an eroding bend when erosion is entirely mediated by slump block armoring. A comparison of (2.21b) and (2.22) reveals that δ has the following physical meaning: it represents the ratio of the migration rate when erosion is completely mediated by slump block armoring to that which would prevail were the bank composed of purely non-cohesive material.

The armoring coefficient is thus:

$$K_{armor} = \frac{1}{\left(1 + \frac{1}{u}\right)} = u - u^2 + \dots \quad (2.23)$$

which we have shown to be small compared to unity for reasonable values of \tilde{T}_c

The above analysis, i.e. for $\delta \ll 1$, corresponds to bank erosion which is completely dominated by the decay time for slump blocks. The more general form of the analysis, however,

encompasses the full range of bank erosion that is totally determined by the removal of non-cohesive sediment to that which is totally dominated by slump block decay.

2.3.3 Slump block decay as function of bank shear stresses

If all the parameters in (2.22) were specified constants, then the bank erosion rate would not be a function of flow conditions, and thus would be decoupled from channel curvature itself. Such a model would be unable to reproduce channel meandering. This, however, is not likely the case. More specifically, slump blocks subject to a higher bank shear stress for a longer time should have a shorter decay time, thus leading to a higher migration rate.

The general assumption is that slump blocks decay by surface erosion via fluvial processes, causing a reduction in the size of the failed elements until they can be fluvially entrained. Few attempts have been made to characterize this. For example, Gabet (1998) tried to estimate the rate of surface erosion of slump blocks using erosion pins, and Simon et al. (1999) explored the potential for fluvial entrainment of the failure elements by comparing the critical shear stress of the blocks and the average boundary shear stress of the flow during peak flow events. In spite of these attempts, the residence time of these failure blocks remains ill-quantified. Estimates range from a few months to many years.

In the present model, we implement a first quantification by assuming that the characteristic slump block lifetime correlates inversely with the Shields number $\tau_{b,E}^*$ adjacent to an eroding bank, which as expressed in (2.11) is directly related to the near-bank channel bed shear stress. In addition, we assume that slump block lifetime also correlates inversely with flood

intermittency I_f , so that more frequent flooding results in a smaller decay time. We propose the following inverse power form:

$$\tilde{T}_c = \tilde{T}_{cref} \frac{I_{f,ref}}{I_f} \left(\frac{\dagger_{b,E}^*}{\dagger_{form}^*} - 1 \right)^{-1} \quad (2.24)$$

where \tilde{T}_{cref} refers to a reference decay time, $I_{f,ref}$ is a reference intermittency and \dagger_{form}^* is a threshold/formative Shield's number below which the bank is unable to erode. The above relation is meant to apply only in the regime $\dagger_{b,E}^* \geq \dagger_{form}^*$; the regime $\dagger_{b,E}^* \leq \dagger_{form}^*$ is taken as depositional rather than erosional, as described below. In the above equation, the characteristic slump block time equals the reference value when $\dagger_{b,E}^* = 2\dagger_{form}^*$ and $I_f = I_{f,ref}$

In (2.24), \dagger_{form}^* serves simply to describe the lower bound for bank erosion. As seen below, it also serves as the upper bound for bank deposition. It has, however, a larger meaning: it sets the formative Shields number for bankfull flow in a straight channel (Parker et al., 2007, Wilkerson and Parker, 2011). More elaboration on this is provided below.

While the model presented here is able to capture the direct effect of armoring on bank erosion in terms of cover, it fails to capture the indirect effect of reduced bank shear stress due to increased bank roughness associated with slump blocks or thick bank vegetation (e.g. Kean and Smith, 2006). The present model can be extended to include the effect of slump block roughness at a later date.

Substituting (2.24) into (2.21), we find that

$$i_{E}^{\sim} = \frac{I_f i_{non,E}^{\sim}}{\left(1 + \left(\frac{\ddagger_{b,E}^*}{\ddagger_{form}^*} - 1 \right)^{-1} I_{f,ref} \frac{|i_{non,E}^{\sim}|}{i_{Eref}^{\sim}} \right)} \quad (2.25)$$

where

$$i_{Eref}^{\sim} = \frac{\tilde{D}_c \tilde{B}_{bw,E}}{\tilde{H}_{c,E} (1 - \}_{pc,E}) \tilde{T}_{cref}} \quad (2.26)$$

is a lumped reference erosion rate that is a function of slump block properties. In its simplified form for $\delta \ll 1$,

$$i_{E}^{\sim} = i_{Eref}^{\sim} \frac{I_f}{I_{f,ref}} \left(\frac{\ddagger_{b,E}^*}{\ddagger_{form}^*} - 1 \right) \text{sgn}(i_{E,non}^{\sim}) \quad (2.27)$$

The simplified equation above is similar in form to the HIPS erosion law, (e.g. Ikeda et al., 1981) according to which increasing near-bank bed shear stress results in an increasing bank erosion rate. It is even more similar to the proposed relation of Howard (1992) and is in keeping with excess shear stress relations typically used for fine-grained materials (e.g. Motta et al., 2012). The difference here is that the erosion coefficient i_{Eref}^{\sim} includes parameters that are at least in principle measurable, and incorporates a physically based model rather than simply representing a calibration parameter as in many previous models.

2.4 Relation for Bank Deposition

In modeling lateral bank deposition, the role of vegetation in trapping and stabilizing depositing sediment must be taken into account. The growth of vegetation is suppressed during inundation, but this vegetation can trap finer sediment, including wash load and the finer part of the bed material load traveling in suspension. During times when the river is not in flood, vegetation can stabilize the sediment deposited within it as roots take hold. In addition, vegetation can encroach on the point bar, stabilize the bed material load that has accreted there, and create conditions that are favorable to the trapping of finer sediment during subsequent high flows. If the near-bank shear stress is high enough during a flood, however, the flow can physically remove the vegetation, or suppress emplacement and sprouting of seedlings.

Here we capture the above effects in the simplest way that can reproduce the essential features. We assume that there is a default rate of transverse migration \tilde{r}_{veg} of the inner accretional bank toward the channel center associated with flows that are insufficient to suppress vegetation growth, i.e. during the fraction of time $1 - I_f$. We then suppress this encroachment rate as the near-bank bed shear stress increases. We quantify this effect in terms of the Shields number $\dagger_{b,D}^*$ based on the streamwise shear stress acting on the bed immediately adjacent to the bank, i.e.

$$\dagger_{b,D}^* = \left\{ \dagger_s^* \Big|_{\tilde{n}=\tilde{n}_{t,j}} \right. \quad (2.28)$$

The rate of channel migration directed toward the channel centerline associated with channel deposition \tilde{r}_D is then given as

$$\tau_{D}^{\sim} = \tau_{veg}^{\sim} (1 - I_f) \left(1 - \frac{\tau_{b,D}^*}{\tau_{form}^*} \right) \quad (2.29)$$

Again, the subscript D denotes a depositing bank. The above equation applies only when $\tau_{b,D}^* \leq \tau_{form}^*$. The parameter τ_{veg}^{\sim} is as yet a poorly-constrained parameter, but can be determined by means of direct field measurements of default encroachment rates.

Three points are worth mentioning here. First, the above formulation, i.e. (2.27) for $\tau_b^* \geq \tau_{form}^*$ and (2.29) for $\tau_b^* \leq \tau_{form}^*$, where τ_b^* is the appropriate near-bank Shields number, does not specify that one bank is eroding and the opposite bank is depositing. Depending on the flow, both banks could erode, both could deposit, or one bank could erode and the other deposit. It is this flexible formulation that allows for the evolution of channel width as the channel migrates.

Second, the parameter τ_{form}^* should correspond to the reach-averaged bankfull Shields number τ_{bf}^* of the channel, in that this parameter can be specifically related to the mechanics by which reach-averaged channel hydraulic geometry is determined (Parker et al., 2007; Wilkerson and Parker, 2011). As a first approximation, we set τ_{form}^* as a constant input parameter, but we later demonstrate empirically that τ_{form}^* varies with reach-averaged channel slope.

Third, the entire model is meant to apply to flood flows that may be somewhat below or above bankfull, but during which time the channel, as well as the processes that cause or set up bank erosion and deposition are active.

2.5 Formative Shields Number and Bankfull Geometry

The purpose of hydraulic geometry relationships is to relate a river's form to a single representative discharge. The representative discharge, or channel forming discharge, as defined by Copeland et al. (2005), is a single discharge that over a long period of time would theoretically “produce the same channel geometry as the natural long-term hydrograph”. Standard practice is to estimate the channel forming discharge with the bankfull discharge \tilde{Q}_{bf} , that is, the discharge at which flow just spills from the channel onto the floodplain (Wolman and Leopold, 1957).

In the bankfull hydraulic geometry relationships, the dependent variables of concern are typically bankfull width \tilde{B}_{bf} , bankfull depth \tilde{H}_{bf} , and streamwise bed slope S . Several studies have attempted to come up with predictive relationships for bankfull geometry, from simple linear regression analyses (e.g. Leopold and Maddock, 1953) to more complex dimensionless variants of this incorporating more physics (Parker et al., 2007; Wilkerson and Parker, 2011). A simple way to describe bankfull characteristics is in terms of a bankfull Shields's number \dagger_{bf}^* (Parker, 2004) as shown below.

Here we consider a channel, the bed morphodynamics of which is dominated by bedload transport. The continuity, momentum and bedload transport equations can be expressed, respectively, as follows assuming normal-flow straight-channel:

$$\tilde{Q}_o = \tilde{U}_o \tilde{B}_o \tilde{H}_o \quad (2.30)$$

$$C_f \tilde{U}_o^2 = g \tilde{H}_o S_o \quad (2.31)$$

$$\tilde{Q}_{so} = 11.2\tilde{B}_o (\dagger_o^*)^{1.5} \left[1 - \frac{\dagger_c^*}{\dagger_o^*} \right]^{4.5} \sqrt{Rg\tilde{D}_s\tilde{D}_s} \quad (2.32)$$

where the subscript “o” denotes reference straight channel configuration and \tilde{Q}_{so} is the volume of bedload sediment transport rate. Here “normal flow” refers to steady, uniform flow. It should be noted that while (2.32) could be an arbitrary relation for sediment transport, the form specified here is identical to (2.9), i.e. is the bedload transport relation of Parker (1979). Under normal flow conditions, bed shear stress varies with the depth-slope product, and thus the Shields number of the flow is given as:

$$\dagger_o^* = \frac{\tilde{H}_o S}{R\tilde{D}_{50}} \quad (2.33)$$

Applying (2.30)~(2.32) to bankfull conditions, and adopting the transformation $\tilde{Q}_o \rightarrow \tilde{Q}_{bf}$; $\tilde{Q}_{so} \rightarrow \tilde{Q}_{sbf}$, $\dagger_o^* \rightarrow \dagger_{bf}^*$ etc., we can specify bankfull geometry in terms bankfull Shields number, bankfull discharge and volume bedload transport rate at bankfull discharge by rearranging the above equations as follows:

$$S = \frac{R\dagger_{bf}^{*3/2}}{11.2C_f^{1/2} (\dagger_{bf}^*)^{1.5} \left[1 - \frac{\dagger_c^*}{\dagger_{bf}^*} \right]^{4.5}} \left(\frac{\tilde{Q}_{sbf}}{\tilde{Q}_{bf}} \right) \quad (2.34)$$

$$\tilde{B}_{bf} = \frac{\tilde{Q}_{sbf}}{11.2 (\dagger_{bf}^*)^{1.5} \left[1 - \frac{\dagger_c^*}{\dagger_{bf}^*} \right]^{4.5} \sqrt{Rg\tilde{D}_s\tilde{D}_s}} \quad (2.35)$$

$$\tilde{H}_{bf} = \frac{11.2(\dagger_{bf}^*)^{1.5} \left[1 - \frac{\dagger_c^*}{\dagger_{bf}^*} \right]^{4.5} C_f^{1/2} \tilde{D}_s}{\dagger_{bf}^{*/2}} \left(\frac{\tilde{Q}_{bf}}{\tilde{Q}_{sbf}} \right) \quad (2.36)$$

Thus for a given bankfull discharge, bedload transport rate at bankfull flow, grainsize, friction coefficient, and bankfull Shields number, we can compute equilibrium channel width, depth and slope from the above equations.

The assumption that a river adjusts itself in such a way as to maintain a specified bankfull Shields number is one that has been variously adopted and justified (see Paola, 1992, Parker et al, 1998). However, Li et al. (2013) have used the databases of Parker et al. (2007) and Wilkerson and Parker (2011) to show that bankfull Shields number is an increasing function of bed slope, over a range of characteristic bed material sizes from coarse silt to cobbles. This trend is indicated in figure 2.5(a). Figure 2.5(b) illustrates the following similarity collapse of the data in figure 2.5(a) due to Li et al. (submitted, Appendix B)

$$\dagger_{bf}^* = 1270(D^*)^{-1} S^{0.54} \quad (2.37)$$

where

$$D^* = \left(\frac{\sqrt{Rg\tilde{D}_s\tilde{D}_s}}{\epsilon} \right)^{2/3} \quad (2.38)$$

is a dimensionless grain size and ϵ denotes the kinematic viscosity of water.

Thus for a given bankfull discharge, grain size, friction coefficient and slope, we can estimate the equilibrium channel characteristics from the equations (2.34)- (2.37) above.

We illustrate application of the above relations by considering an example of a small, actively meandering river, i.e. the Vermillion River near Empire, Minnesota, USA (Lauer and Parker, 2008). This reach is of significance in the present analysis because it provides the input parameters for the calculations of river bend migration given below. The following parameters apply: $\tilde{D}_s \sim 2$ mm, $\tilde{H}_{bf} = 0.88$ m, $\tilde{B}_{bf} = 15$ m, $S = 0.00058$ and $\tilde{Q}_{bf} = 10$ m³/s. The friction coefficient C_f computed from these numbers is 0.0087, and the bankfull Shields number \dagger^*_{bf} is 0.155.

Assuming that C_f , \tilde{D}_s , R and \dagger^*_{bf} are given, (2.34)-(2.36) specify 3 equations relating the 5 parameters \tilde{H}_{bf} , \tilde{B}_{bf} , S , \tilde{Q}_{bf} and \tilde{Q}_{sbf} . For example, the specifications $\tilde{Q}_{bf} = 10$ m³/s and $S = 0.00058$ yields the values for \tilde{H}_{bf} , \tilde{B}_{bf} , and \tilde{Q}_{sbf} of 0.88m, 14.9m, 1.4×10^{-3} m³/s.

Now the analysis given above ignores the fact that the Vermillion River is meandering. That is, it treats the river as if it were a straight bankfull channel with a bed slope $S = 0.00058$. The analysis is easily extended to an overwidened, overnarrowed or meandering channel by interpreting \dagger^*_{bf} as the formative Shields number \dagger^*_{form} in the relations for bank erosion (2.27) and bank deposition (2.29).

In a straight channel at bankfull flow, the near-bank Shields number \dagger^*_b is equal to \dagger^*_{form} at both banks, and they neither erode nor deposit. If the straight channel is overwidened compared

to the value consistent with \dagger^*_{form} , \dagger^*_b will fall below \dagger^*_{form} , and the channel will narrow by deposition in accordance with (2.29). If the straight channel is overnarrowed compared to the value consistent with \dagger^*_{form} , \dagger^*_b will fall above \dagger^*_{form} , and the channel will widen by erosion in accordance with (2.27). And finally, if the channel is sinuous, \dagger^*_b may fall above \dagger^*_{form} at one bank and below it at the opposite bank, resulting in channel shift. This is the basis for the analysis for bend shift given below.

Figures 2.6(a) and 2.6(b) also include a point representing the Vermillion River. The figure indicated that should the channel become more sinuous, downstream bed slope S would drop, and so \dagger^*_{form} would increase. It turns out that inclusion of this effect is important for the analysis given below; its neglect results in a bend that overnarrows as it migrates outward.

2.6 Nonlinear in-channel morphodynamic model

The standard quasi-steady approximation for bed morphodynamics (de Vries, 1965) allows for a remarkable simplification of the problem. According to the approximation, the characteristic adaptation time for the bed to changed flow is much larger than the characteristic adaptation time for the flow to changed bed. Under appropriate constraints, this condition allows neglect of time variation terms in the flow hydraulics. That is, the flow is treated as quasi-steady, and time variation is accounted for only in the Exner equation of sediment mass conservation.

Here we use a somewhat similar approximation in treating migrating bends. We assume that the characteristic time of planform migration is at least an order of magnitude more than the characteristic time of bed response to changed planform. As a result, we treat both the hydraulics

and bed morphodynamics as quasi-steady, and account for time variation only through the relations governing channel migration.

The full 2.5D equations governing channel hydrodynamics/morphodynamics in meandering channels can be found in, for example, Camporeale et al. (2007). These equations are 2.5D in the sense that depth-averaged parameters such as streamwise and transverse flow velocity U and V , respectively, satisfy the fully nonlinear 2D St. Venant equations, but a linear correction for vertical structure is used to characterize secondary flow in bends. These equations can be applied, within limits, to a meandering channel of arbitrary shape. Here, however, a simpler configuration is considered so as to allow a clear view of the role of bank erosion and deposition on channel migration.

This simpler configuration consists of bend flow, i.e. fully developed flow in a channel with curvature that is constant in the streamwise direction but varies in time, i.e. such that all the streamwise derivatives vanish i.e. $\frac{\partial}{\partial s} \rightarrow 0$ and in addition, the depth-averaged transverse velocity $V = 0$. The bend can change in both width and curvature, according to the dynamics of the inner and outer banks (both of which may either erode or deposit) and their interaction with the morphodynamics of the central region of the channel. This configuration is illustrated in figure 2.7.

In the case of constant centerline curvature, the dimensionless steady-state depth-averaged equations of motion for a general fluid flow in intrinsic curvilinear coordinates can be simplified to:

$$\frac{2CU\{\}}{1+nC} + \frac{1}{H} \frac{\partial HU\{\}}{\partial n} = \frac{1}{(1+nC)} \frac{1}{Fr_o^2} S\chi_o - \frac{\chi_o \dagger_s}{H} \quad (2.39)$$

$$\frac{C(\mathbb{E} - U^2)}{1+nC} + \frac{1}{H} \frac{\partial H\mathbb{E}}{\partial n} = -\frac{1}{Fr_o^2} \frac{\partial \langle}{\partial n} - \frac{\chi_o \dagger_n}{H} \quad (2.40)$$

and the steady state Exner equation of bed sediment conservation is given as:

$$\frac{\partial q_n (1+nC)}{\partial n} = 0 \quad (2.41)$$

where U denotes dimensionless depth-averaged streamwise flow velocity, H denotes dimensionless depth, C denotes dimensionless channel centerline curvature, \langle denotes dimensionless water surface elevation, S is the streamwise channel slope which is by definition dimensionless, \dagger_s and \dagger_n are dimensionless streamwise and transverse bed shear stresses respectively and q_n is the dimensionless transverse volume sediment transport rate per unit width.

These are related to their dimensioned counterparts as:

$$\begin{aligned} (s, n) &= \frac{(\tilde{s}, \tilde{n})}{\tilde{b}_o}; \quad U = \frac{\tilde{U}}{\tilde{U}_o}; \quad C = \tilde{b}_o \tilde{C}; \quad (H, \langle) = \frac{(\tilde{H}, \tilde{\langle})}{\tilde{H}_o}; \\ (\dagger_s, \dagger_n) &= \frac{(\tilde{\dagger}_s, \tilde{\dagger}_n)}{\dots \tilde{U}_o^2}; \quad q_n = \frac{\tilde{q}_n}{\sqrt{Rg\tilde{D}_s \tilde{D}_s}} \end{aligned} \quad (2.42)$$

where \tilde{D}_s denotes the dimensioned grain size, g is the acceleration due to gravity and the submerged specific gravity of sediment is denoted as R ($= 1.65$ for quartz). The relevant scales for the non-dimensionalization are the dimensioned reference flow velocity \tilde{U}_o , flow depth \tilde{H}_o

and channel half-width \tilde{b}_o , all referenced to a straight channel defined here as the straight channel with streamwise slope S_o and a width equal to the mean width of the meandering channel. The Froude number Fr_o and ratio of half-width to depth χ_o of the base flow are given as

$$Fr_o = \frac{\tilde{U}_o}{\sqrt{g\tilde{H}_o}}; \quad \chi_o = \frac{\tilde{b}_o}{\tilde{H}_o} \quad (2.43)$$

Finally, the parameters $\{$ and \mathfrak{E} in (2.39) and (2.40) are defined below:

$$\{ = \int_0^1 TV_s dz; \quad \mathfrak{E} = \int_0^1 V_s^2 dz \quad (2.44)$$

where V_s denotes the dimensionless, curvature-induced secondary flow defined such that

$\int_0^1 V_s dz = 0$ and approximated according to Ikeda and Nishimura, (1986):

$$V_s = \frac{UH}{r\chi_o\sqrt{C_f}} CG(z) \quad (2.45)$$

In the above equation, r is an eddy viscosity coefficient, C_f is a dimensionless bed friction coefficient, T represents a structure function corresponding to the vertical distribution of streamwise flow velocity in a reference straight channel (here we have adopted the Engelund (1974) function) and G is the normalized secondary flow structure function defined in Johannesson and Parker (1989)

2.6.1 Bed shear stresses and sediment transport

The dimensionless bed shear stress components can be expressed as:

$$(\dagger_s, \dagger_n) = C_f U \left(U, \frac{V_s(0)}{T(0)} \right) \quad (2.46)$$

Note that the lateral shear stress \dagger_n here is purely due to secondary flows V_s .

The transverse bedload transport is modeled by a linear dependence on the local bedslope such that

$$q_n = \Phi \left(\frac{\dagger_n^*}{\dagger_s^*} - \frac{s}{\chi_o} \frac{\partial y}{\partial n} \right) \quad (2.47)$$

where Φ is the bedload intensity here estimated using the relation of Parker (1979) described in (2.9) (but with $\Phi_b \rightarrow \Phi$), \dagger_s^* and \dagger_n^* are the two components of the Shields stress vector given as:

$$(\dagger_s^*, \dagger_n^*) = \frac{Fr_o^2}{RD_s} (\dagger_s, \dagger_n) \quad (2.48)$$

and s is as defined in (2.10)

2.6.2 Boundary conditions

The lateral boundary condition associated with governing equations is the no penetration boundary condition for sediment transport. By assuming a zero flux of sediment at the banks, we are

assuming that over the characteristic time scale of bed morphodynamics, sediment transfer due to bank erosion/deposition is negligible. This quasi-steady assumption holds in general for typical natural rivers with cohesive or armored banks that migrate at a characteristic time scale that is long compared to the morphodynamic response time of the bed. However, for a generalized model that can also capture purely non-cohesive systems, full coupling between bed and bank transport, with non-vanishing transverse sediment transport at the banks, would be necessary.

Finally, the imposed integral conditions for the conservation of water and sediment discharge within the channel are as follows:

$$\int_{-1}^1 UHdn = 2 \quad (2.49)$$

$$\int_{-1}^1 q_s dn = 2\Phi_o \quad (2.50)$$

where Φ_o is the streamwise bedload transport rate Φ for the reference straight channel of width $2b_o$. Assuming that the channel width does not change, the integral conditions in (2.49) and (2.50) assume that the water discharge and sediment discharge in the channel respectively, is held constant regardless of sinuosity. As a result, the average channel slope S becomes a free variable represented by the deviation s_{do} from the reference straight channel slope S_o such that

$$S = S_o (1 + s_{do}) \quad (2.51)$$

Nonlinear effects imply that in the case of a bend with the same average width, the same sediment transport rate is realized at an average bed slope that differs from the case of a straight channel. In

keeping with (2.51), we also define *constant* deviatoric velocity and depth parameters, u_{do} and h_{do} respectively, which allow total velocity and flow depth in the case with a bend of same average width to average to different values than in the case of a straight channel. Thus

$$H_{mean} = 1 + h_{do}; \quad U_{mean} = 1 + u_{do} \quad (2.52)$$

2.6.3 Nonlinear solution

As outlined in Imran et al (1999) and Camporeale et al. (2007), one way to iteratively solve for the steady flow and morphodynamics in a meandering channel with specified banks involves expressing each morphodynamic variable as the sum of a uniform flow and a deviation due to the effect of channel curvature Thus, local variables are expressed as follows:

$$\begin{aligned} U &= U_{mean} + u_d = 1 + u_{do} + u_d \\ H &= H_{mean} + h_d = 1 + h_{do} + h_d \\ \zeta &= \zeta_{mean} + \zeta_d = \zeta_r - S_o (1 + s_{do}) x_o s + \zeta_d \\ y &= \zeta - H = \zeta_{mean} - H_{mean} + y_d; \quad y_d = \zeta_d - h_d \end{aligned} \quad (2.53)$$

where y_r is a reference bed elevation and the deviations are defined such that:

$$\int_{-1}^1 u_d dn = 0 \quad \int_{-1}^1 h_d dn = 0 \quad \int_{-1}^1 \zeta_d dn = 0 \quad \int_{-1}^1 y_d dn = 0 \quad (2.54)$$

Substituting into the governing equations and applying the boundary and integral condition, we arrive at an implicit nonlinear solution to the governing equations expressed in integral form as follows:

$$\langle_d = Fr_o^2 C t_{20} n + \int_{-1}^n R_2 dn - \frac{1}{2} \int_{-1}^1 \int_{-1}^n R_2 dndn \quad (2.55)$$

$$y_d = -ACn + \int_{-1}^n R_3 dn - \frac{1}{2} \int_{-1}^1 \int_{-1}^n R_3 dndn \quad (2.56)$$

$$u_d = \frac{1}{2} \left(Fr_o^2 t_{20} + A - 1 \right) nC + \frac{1}{2} \left(\int_{-1}^n R_2 dn - \frac{1}{2} \int_{-1}^1 \int_{-1}^n R_2 dndn - R_3 + R_1 - \frac{1}{2} \int_{-1}^1 R_1 dn \right) \quad (2.57)$$

$$u_{do} = R_4 \quad (2.58)$$

$$h_{do} = R_5 - R_4 \quad (2.59)$$

$$s_{do} = 3R_4 - R_5 - \frac{1}{2} \int_{-1}^1 R_1 dn \quad (2.60)$$

where R_1, R_2, R_3, R_4 , and R_5 are nonlinear residuals given as:

$$R_1 = 1 - \frac{2CU\{}}{\chi_o C_f} - \frac{(1+nC)}{H\chi_o C_f} \frac{\partial HU\{}}{\partial n} - \frac{U^2}{H} (1+nC) + 2(u_d + u_{do}) + nC - h_d \quad (2.61)$$

$$R_2 = -Fr_o^2 \frac{G(0)}{t} C(U^2 - 1) - Fr_o^2 C \left[\frac{(\mathbb{E} - U^2)}{1+nC} + 1 \right] - Fr_o^2 \frac{1}{H} \frac{\partial H\mathbb{E}}{\partial n} \quad (2.62)$$

$$R_3 = -AHUC + AC \quad (2.63)$$

$$R_4 = -\frac{1}{2M} \int_{-1}^1 R_q dn \quad (2.64)$$

$$R_5 = -u_{do}h_{do} - \frac{1}{2} \int_{-1}^1 u_d h_d dn \quad (2.65)$$

In (2.64), R_q denotes the nonlinear residual of the dimensionless bedload intensity ie.:

$$\Phi = \Phi_o \left[1 + M(u_{do} + u_d) + R_q \right] \quad (2.66)$$

while $M = 2 \frac{\ddagger_o^*}{\Phi_o} \left(\frac{\partial \Phi}{\partial \ddagger^*} \right) \Big|_o$, $A = -\frac{1}{rs\sqrt{C_f}} \frac{G(0)}{T(0)}$ and $t_{20} = 1 - \left(r\sqrt{C_f} \right)^{-1} \frac{G(0)}{T(0)}$

If these nonlinear terms are neglected, the problem has a linear solution corresponding to very small curvature, e.g. as presented in Johannesson and Parker (1989). The nonlinear solution of this system of equations is obtained iteratively starting from an initial linear solution. This iterative scheme represents a generalization of that of Smith and McLean (1984) and Imran et al. (1999). They applied the method for flow over a specified bed; here we include bed morphodynamics as well.

The case of a straight channel is recovered by setting centerline curvature $C = 0$ in the above formulation.

2.7 Channel evolution in time

The model as outlined above a) computes flow and morphodynamics in the central region of the channel (Figure 2.1) using the quasi-steady formulation above, and b) moves the banks according to the shock condition (2.5), and (2.25) for an eroding bank or (2.29) for a depositing bank. As

previously noted, this procedure is justified when the time scale for bank adjustment is much larger than that for bed and flow adjustment.

Implementation of the model requires two global constraints. One choice of constraints is that of constant streamwise water and sediment discharge, as specified in (2.49) and (2.50). It is indeed possible to run the present model under these constraints. There is, however, an alternative pair of constraints for spatially uniform bend flow that is more informative, i.e. constant streamwise water discharge and constant rate of centerline elevation drop per unit angle change. The second constraint takes the form $\partial \tilde{z}_c / \partial \theta = \text{constant} < 0$, where \tilde{z}_c is centerline elevation and θ angle in the horizontal plane, as illustrated in figure 2.7. This configuration for a time-evolving, spatially constant curvature channel treats analogously to it a spiral staircase, the steps of which can either grow outward or shrink inward in the horizontal. Consider a modeled reach extending over a horizontal angle difference $\Delta \theta$. Under the constraint of constant elevation drop $\Delta \tilde{z}$ over this reach as centerline radius of curvature \tilde{R}_c changes, centerline bed slope S_c over this reach must vary as

$$S_c(\tilde{t}) = \frac{\Delta \tilde{z}}{\tilde{R}_c(\tilde{t}) \Delta \theta} \quad (2.67)$$

Note that from (2.67), an outwardly-migrating channel undergoes an increase in radius of curvature, and decrease in slope as it does so. Under this constraint, in the limiting case of $\tilde{R}_c \rightarrow \infty$, i.e. a straight channel, $S_c \rightarrow 0$.

The model is also implemented for a straight channel, for which $\tilde{R}_c = \infty$. The relevant constraints for this case are constant streamwise water discharge and constant centerline bed slope S_c .

The algorithm for channel evolution is as follows. At each time step of the simulation, given the channel geometry:

- the nonlinear flow and relative bed elevation are evaluated iteratively from the equations in the previous section;
- near-bank Shields stresses are computed, and for a specified formative Shields number, the migration rate of each bank is computed according to (2.5), (2.25) and (2.29);
- the time rate of change of the location of the channel centerline (change in the radius of curvature \tilde{R}_c) and the width of the channel region are computed as

$$\frac{\partial \tilde{R}_c}{\partial \tilde{t}} = \frac{1}{2} (\dot{n}_{LB} + \dot{n}_{RB}) \quad (2.68)$$

$$\frac{d\tilde{b}_o}{d\tilde{t}} = \frac{1}{2} (\dot{n}_{RB} - \dot{n}_{LB}) \quad (2.69)$$

from which new values of \tilde{R}_c and \tilde{b}_o are computed;

- A new reference slope is computed from the constraint (2.67) and the reference water depth and velocity are computed as;

$$\tilde{H}_o = \left(\frac{C_f \tilde{Q}_o^2}{4\tilde{b}_o^2 \tilde{g} S_o} \right)^{1/3} ; \quad \tilde{U}_o = \left(\frac{\tilde{g} \tilde{Q}_o S_o}{C_f 2\tilde{b}_o} \right)^{1/3} \quad (2.70)$$

- After updating channel geometry, the above steps are repeated, so allowing the channel to evolve.

2.8 Model Implementation

2.8.1 Model Input Parameters

We implement the model with a parameter set that is based on a reach of the meandering Vermillion River, Minnesota USA, shown in figure 2.8 (Lauer and Parker, 2008). As shown in tables 2.1 and 2.2, the following estimated have been used: bankfull discharge $\tilde{Q}_{bf} = 10 \text{ m}^3/\text{s}$, flood intermittency $I_f =$ reference flood intermittency $I_{f,ref} = 0.05$, bankfull width $\tilde{B}_{bf} = 15 \text{ m}$, bankfull depth $\tilde{H}_{bf} = 0.88 \text{ m}$, mean channel slope $S_o = 0.00058$ and characteristic bed grain size $\tilde{D}_s = 2 \text{ mm}$. (Input values of I_f that differ from $I_{f,ref}$ allow a first quantification of change in flood frequency on the bank erosion rate.)

These parameters yield estimates of formative (bankfull) Shields number $\tau_{form}^* = 0.155$ and bed friction coefficient $C_f = 0.0087$. Figure 2.6(a,b) compares the formative Shields number of the Vermilion River with existing hydraulic datasets of Parker et al. (2007) and Wilkerson and Parker (2011), and shows that the formative Shields number falls within the range for rivers of similar scale and characteristics. Other input parameters are as shown in table 2.2, along with a justification for the values selected. Of particular importance are the base values for \tilde{i}_{veg} and \tilde{i}_{Eref}

(i.e. \tilde{r}_{vegB} and \tilde{r}_{ErefB}) which are 0.79 m/yr and 1.45 m/yr, respectively. The model is applied to two case scenarios: Set 1 runs are for a straight channel (centerline curvature $C = 0$), while Set 2 runs are for the case of a channel with spatially constant centerline curvature $C > 0$.

In the reach of the Vermillion River studied by Lauer and Parker (2008), channel migration rates vary from 0 to about 1.2 m/yr, Table 2.1 reflects an overall characteristic value of 0.75 m/yr. In the present study, values of input parameters relating to vegetal encroachment and slump block armoring have been selected to allow for migration rates that are within this range. Specific justification is given in table 2.2. In the modeling presented below, bank migration rates vary from 0 to 0.82 m/yr.

2.8.2 Straight Channel Runs

Any model of meander migration (or the simpler case of bend migration considered here) that predicts width variation must be able to do so for the case of a straight channel as well. An overwide channel must narrow so as to reach its formative state in accordance with (2.34), (2.35) and (2.36), and an overnarrow channel must commensurately widen. Here we study these cases. It should be noted that the form of the quasi-steady formulation applied above, i.e. quasi-steady central region morphodynamics, precludes the formation of such features as alternate bars, and permits a focus on width variation itself.

The straight channel represents a solution at zeroth order in curvature. Since the formative Shields number has been set as equal to the Shields number corresponding to bankfull flow, it follows that for specified bankfull discharge \tilde{Q}_{bf} and bed slope S , a channel with width \tilde{B}_{bf} depth

\tilde{H}_{bf} and sediment load \tilde{Q}_{sbf} computed from (2.34), (2.35) and (2.36) should in the absence of any external forcing, experience neither erosion nor deposition at either bank.. For a somewhat wider (narrower) channel, however, both banks will respond to this deviation in accordance with (2.25) and (2.29) and become depositional (erosional) until channel width is adjusted to its equilibrium state. Both banks move at equal rates and in opposing directions so that the net centerline migration is zero.

Figure 2.9(a) illustrate the process of relaxation toward formative conditions over time for: a) an equilibrium channel (i.e. the default case for which nothing happens); b) a channel with half the equilibrium width, i.e. $\tilde{B}_i / \tilde{B}_{bf} = 0.5$, where \tilde{B}_i is initial width: and c) a channel with twice the equilibrium width, i.e. $\tilde{B}_i / \tilde{B}_{bf} = 2.0$. In cases b) and c), the initial depth \tilde{H}_i has been computed from (2.70). Figure 2.9(b) shows the evolution of the Shield's ratio ($\dagger_o^* / \dagger_{form}^*$), where \dagger_o^* = Shields number at any given time, as well as channel width in time for the three cases in 2.9(a)

The time of adjustment \tilde{t}_{adj} required to reach the equilibrium is here defined as the time required for $\left| \left(\dagger_o^* - \dagger_{form}^* \right) / \dagger_{form}^* \right| \leq \epsilon$, where ϵ is a tolerance here chosen to be 0.001. For the cases $\tilde{B}_i / \tilde{B}_{bf} = 0.5$ and 2.0 in figure 2.10, this time was 43.0 years and 57.6 years. This parameter is a function of how much the initial width deviates from equilibrium, and also the two parameters \tilde{i}_{veg} and \tilde{i}_{Eref} that capture bank deposition and erosion rates, respectively.

Figure 2.10(a) shows the effect of varied degree of initial overnarrowing relative to bankfull, i.e. values of $\tilde{B}_i / \tilde{B}_{bf}$ ranging from 0.25 to 0.95, and values of \tilde{i}_{Eref} varying from 0.5

i_{ErefB}^{\sim} to $4 i_{ErefB}^{\sim}$, on the time to equilibrium. As might be expected, the adjustment time a) increases with decreasing values of $\tilde{B}_i / \tilde{B}_{bf}$, i.e. increasing degrees of initial overnarrowing, and b) decreases with increasing reference bank erosion rate i_{Eref}^{\sim} . Figure 2.10(b) shows a corresponding plot for illustrating the effect of varying degrees of initial overwidening, i.e. values of $\tilde{B}_i / \tilde{B}_{bf}$ ranging from 1.05 to 2.0, and values of i_{veg}^{\sim} varying from $0.5 i_{vegB}^{\sim}$ to $4 i_{vegB}^{\sim}$, on the time to equilibrium. Again, the result is as expected; larger values of $\tilde{B}_i / \tilde{B}_{bf}$ correspond to larger adjustment times, and larger values of i_{veg}^{\sim} correspond to smaller adjustment times.

The results of figures 2.10(a) and 2.10(b) can be collapsed into self-similar forms. In figure 2.10(c), the fraction deviation of initial width from bankfull $|\tilde{B}_i - \tilde{B}_{bf}| / \tilde{B}_{bf}$ is plotted against a dimensionless adjustment time t_{adj} , where

$$t_{adj} = \tilde{t}_{adj} i_{ref}^{\sim} / \tilde{B}_{bf} \quad , \quad i_{ref}^{\sim} = \begin{cases} i_{Eref}^{\sim} & , \quad \tilde{B}_i < \tilde{B}_{bf} \\ i_{veg}^{\sim} & , \quad \tilde{B}_i > \tilde{B}_{bf} \end{cases} \quad (2.71)$$

It is seen in the figure that the results for initially overnarrowed channels, which adjust purely by bank erosion collapse to one line, and the results for initially overwidened channels, which adjust purely by bank deposition collapse to another line.

The sensible results for the case of width evolution obtained for straight channels justifies the extension to channel migration and width evolution in bends, as described below.

2.8.3 Runs for Migrating Bends with Spatially Constant Curvature

The introduction of curvature forcing causes a deviation from the straight channel solution, so that the centerline radius of curvature \tilde{R}_c evolves according to (2.68) and channel half-width \tilde{b}_o evolves according to (2.69). It is important to realize that there is no dynamic equilibrium width for this case. Instead, the channel reaches an asymptotic state at which the channel very slowly narrows as it migrates outward, with both banks migrating at almost the same rate.

This asymptotic slow outward narrowing is dictated by (2.67), (2.33) and (2.34). In order to maintain a constant elevation difference Δz between the upstream and downstream end of the modeled reach, channel centerline bed slope S_c must decrease as centerline radius of curvature \tilde{R}_c increases, in accordance with (2.69). For constant water discharge, (2.34) dictates that decreasing slope results in decreasing sediment feed rate, and (2.35) dictates that a decreasing feed rate results in decreasing width.

The asymptotic state is most easily visualized as a convergence line in a plot of migration rates in phase space. We consider figure 2.11, in which the left bank is the inner bank and the right bank is the outer bank. The left and right bank migration rates are \dot{n}_{LB} and \dot{n}_{RB} , respectively, where each takes a positive value when it is directed to the right of channel centerline. The convergence line is defined by the condition $\dot{n}_{LB} = \dot{n}_{RB}$. Depending upon the initial conditions, \dot{n}_{LB} and \dot{n}_{RB} can take arbitrary values, either larger or smaller than zero. After a sufficient amount of time, however, both become positive (corresponding to outward migration), and both then decrease slowly toward

zero, with the condition $\dot{n}_{LB} = \dot{n}_{RB}$ being very nearly, but never precisely satisfied, so that the channel continues to narrow. This is illustrated in figure 2.11.

Figure 2.11 shows five possible regimes. When $\dot{n}_{LB} < 0$ and $\dot{n}_{RB} < 0$, the channel migrates inward. When $\dot{n}_{LB} < 0$ and $\dot{n}_{RB} > 0$, both banks erode. When $\dot{n}_{LB} > 0$ and $\dot{n}_{RB} < 0$, both banks deposit. The two most important cases are when $\dot{n}_{LB} > \dot{n}_{RB} > 0$ and $\dot{n}_{RB} > \dot{n}_{LB} > 0$. In the former case, the channel migrates outward, with the inner deposition rate exceeding the outer erosion rate. This is the case of *bar push*: erosion at the outer bank is being forced by a more rapidly accreting point bar. In the latter case, the channel migrates outward, with the outer erosion rate exceeding the inner deposition rate. This is the case of *bank pull*: deposition at the point bar is being forced by a more rapidly eroding outer bank. An introduction to these concepts can be found in Stillwater Sciences (2007). Five lines in figure 2.11, each starting from a circle corresponding to initial migration rates, illustrate how a channel evolves toward the asymptotic state.

Figure 2.12A illustrate the process of relaxation toward symptotic conditions over time for: a) an equilibrium channel; b) a channel with half the equilibrium width, i.e. $\tilde{B}_i / \tilde{B}_{bf} = 0.75$, and c) a channel with twice the equilibrium width, i.e. $\tilde{B}_i / \tilde{B}_{bf} = 2.0$. Figure 2.12B shows results for a bend with an initial curvature $C_i = 0.05$, and initial widths \tilde{B}_i equal to the reference bankfull value \tilde{B}_{bf} for a straight channel, and also the initial values $0.75\tilde{B}_{bf}$ and $2\tilde{B}_{bf}$. The parameters $\tilde{\tau}_{Eref}$ and $\tilde{\tau}_{veg}$ are the base values given in table 2.2. The formative Shields number \dagger_{form}^* is held at the value 0.16 given in table 2.2, and not allowed to vary according to (2.37). Figure 2.12B (a) shows the evolution of $\dagger_o^* / \dagger_{form}^*$, where \dagger_o^* , which is computed from (2.33), is the Shields number that a

straight channel would have at the current centerline slope of the bend at any given time. Figure 2.12B (b) shows the evolution of channel width. The images on the right-hand side of the figure correspond to expanded views of the left-hand side figure to allow visualization of the early stage of evolution.

As in Figure 2.9, in the two cases where the initial channel is wider (narrower) than the reference straight-channel value \tilde{B}_{bf} , the channel goes through a rapid adjustment phase where the channel narrows (widens). This phase has a duration of about 50 years. After this adjustment, the Shields number \dagger_o^* converges to a value close to \dagger_{form}^* , and stays very near it up to 5000 years. Width, on the other hand, declines monotonically, such that by 5000 years, \tilde{B} drops to $0.69 \tilde{B}_{bf}$ for the case $\tilde{B}_i = 2\tilde{B}_{bf}$, and $0.48 \tilde{B}_{bf}$ for the case $\tilde{B}_i = \tilde{B}_{bf}$. Indeed, for the case $\tilde{B}_i = 0.75\tilde{B}_{bf}$, the channel becomes so narrow that the numerical model fails after 1900 years.

This problem was first recognized in simulations of fully meandering channels (shown in Chapter 3). More specifically, when \dagger_{form}^* is held constant, the channel tends to narrow to an unreasonably small value, with concomitant model failure, before cutoff is achieved. Increasing sinuosity, however, corresponds to declining centerline slope. We found the problem could be resolved in terms of (2.37) and the information in figure 2.6; \dagger_{form}^* should decline as centerline slope S_c declines.

Figure 2.13 shows a comparison of model runs using a constant value $\dagger_{form}^* = 0.16$ (as per table 2.2) versus runs using the relation

$$\dagger_{form}^* = 0.16 \left(\frac{S_c}{S_{ci}} \right)^{0.54} \quad (2.72)$$

where S_{ci} is the initial centerline slope, as per (2.37). In the figure, $\tilde{B}_i = \tilde{B}_{bf}$; three initial dimensionless curvatures $C_i = 0.025, 0.5$ and 0.1 are considered. The results on the left panel are for case of constant \dagger_{form}^* , and those on the right panel are for \dagger_{form}^* varying according to (2.72). Width still declines monotonically with time when \dagger_{form}^* is allowed to vary with slope, as dictated by the condition (2.67). The decline is, however, much more modest, and calculations can be extended for far longer than 5000 years before slope drops so low that the width becomes unrealistically low. With this in mind, (2.72) is adopted for all calculations below.

Figure 2.14 shows a plot on the $\dot{n}_{LB} - \dot{n}_{RB}$ phase plane of the results of calculations for three different initial widths corresponding to $\tilde{B}_i = 0.75\tilde{B}_{bf}$, $\tilde{B}_i = \tilde{B}_{bf}$ and $\tilde{B}_i = 2\tilde{B}_{bf}$. Dimensionless curvature C is 0.05; i_{veg}^{\sim} and i_{Eref}^{\sim} take their base values of table 2.2. When $\tilde{B}_i = \tilde{B}_{bf}$, the channel begins close to the convergence line, and approaches it via bank pull: the right (outer) bank migrates outward faster than the left (inner) bank (as defined in figure 2.11). Once the convergence line is reached, the channel narrows slowly as slope declines, with very nearly equal migration rates that fall barely in the bar push zone.

When $\tilde{B}_i = 0.75\tilde{B}_{bf}$, figure 2.14 indicates that the overnarrow initial channel first undergoes erosion at both banks, and then approaches the convergence line via bank pull (figure 2.11). When $\tilde{B}_i = 2\tilde{B}_{bf}$, the overwide channel first undergoes deposition at both banks, and then

approaches the convergence line via bar push, such that the left (inner) bank migrates faster than the right (outer) bank (figure 2.11).

Figure 2.15 illustrates the effect of variation in the values of i'_{Eref} and i'_{veg} on phase plane evolution. In the calculations, $\tilde{B}_i = \tilde{B}_{bf}$ and $C_i = 0.1$. In figure 2.15a, i'_{veg} is held at the base value of table 2.2, and i'_{Eref} is varied from 0.5 to 4 times the base value. Note in figure 2.15a that the starting value of \dot{n}_{LB} i.e. inner bank migration migration rate, takes the same positive value, corresponding to deposition, for all values of i'_{Eref} . In all cases evolution toward the convergence line is by means of bank pull; the larger the value of i'_{Eref} , the farther the channel starts from the convergence line and the longer is the trajectory over which bank pull brings it to the convergence line. Although the region of bar push is not reached, it is seen that decreasing values of i'_{Eref} bias channel evolution in the direction of bar push.

In figure 2.15b, i'_{Eref} is held at the base value of table 2.2, and i'_{veg} is varied from 0.5 to 4 times the base value. The starting value of \dot{n}_{RB} i.e. outer bank migration migration rate, takes the same positive value, corresponding to erosion, for all values of i'_{veg} . For the cases $i'_{veg} = 0.5, 1$ and 2 times the base value, the channel migrates outward via bank pull; for the case $i'_{veg} = 4$ times the reference value, the channel evolves via bar push. Evidently for the same value of i'_{Eref} , increasing i'_{veg} biases evolution from bank pull toward bar push.

Figure 2.15 captures a trend that prevails in general: for the same reference erosion rate, increasing reference deposition rate biases evolution in the direction of bar push, and increasing reference erosion rate biases channel evolution in the direction of bank pull.

Figure 2.16 illustrated the effect of varying initial dimensionless curvature C_i on channel evolution. The cases $C_i = 0.025, 0.05$ and 0.1 are considered. The three lines corresponding to bank pull are computed using the reference values of $\tilde{\tau}_{veg}$ and $\tilde{\tau}_{Eref}$. The three lines corresponding to bar push are computed using the reference value of $\tilde{\tau}_{Eref}$, and a value of $\tilde{\tau}_{veg}$ that is four times the reference value (a value specifically chosen to give bar push in all cases). The effect increasing initial curvature is to increase the initial values of \dot{n}_{LB} and \dot{n}_{RB} ; otherwise, the pattern of evolution on the phase plane is very similar.

2.9 Discussion

This paper is focused on natural armoring due to vegetated slump blocks. This form of natural armoring is common along the banks of relatively small-scale meandering rivers (e.g. the Embarras River, Illinois, USA, Engel and Rhoads, 2012). In the case of larger rivers, natural armoring may be dominated by tree stumps and root wads (e.g. the Wabash river, Illinois/Indiana, USA, Konsoer et al., 2012). In the model outlined here, armoring is accomplished by direct cover of non-cohesive bank material. The model should in the future be adapted to include the armoring effect due to drag extraction on the armor elements themselves, which reduces the shear stress on the non-cohesive material in between (Kean and Smith, 2006). This adaptation is likely to play a stronger role in the case of tree stumps and root wads than it does in the case of vegetated slump blocks.

Here it is assumed that armoring is stronger as slump block density increases. This is likely true at the macroscopic scale considered here. At the scale of the slump blocks themselves, however, they may locally deflect the flow toward an unprotected bank, therefore occasionally increasing the rate of bank erosion.

The simplified case of bends with spatially constant centerline curvature is considered here; the bend migrates, and its width evolves in time. In Chapter 3, we generalize this formulation to fully meandering channels, and studied channel evolution up to and beyond cutoff.

In the formulation herein, a quasi-steady assumption is used to treat bed morphodynamics. Such a formulation precludes the formation of free bars (e.g. Seminara, 2006). This simplification facilitates direct focus on bend-driven processes. The recent model of meander migration due to Asahi et al. (2013), which is also based on the framework of Parker et al. (2011), allows the formation of free bars. It is similar to the present model in the way it treats eroding banks. Depositing banks, however, are treated differently. In Asahi et al. (2013), the speed of vegetal encroachment is not specified. Instead a two-step hydrograph is used, and a point is assumed to be vegetally stabilized if it has not been inundated for a specified amount of time. Here the effect of hydrograph variation is built into the relations (2.24) and (2.29); slump block lifetime is inversely proportional to the fraction of time the river is in flood, and the vegetal encroachment rate is proportional to the fraction of time that the river is not in flood.

The model of Asahi et al. (2013) has not yet been applied at field scale. The present model is specifically applied at the scale of the Vermillion River, Minnesota, USA. The former model appears to be more suited to gravel-bed rivers in which vegetation only slowly encroaches onto

point bars. This results in a high degree of width variation as the channel evolves. The present model is more suited to sand-bed rivers in humid regions, where vegetation encroachment tends to keep up with the bankline of bankfull flow. This results in a lower, but still substantial variation of width as the channel evolves. In the future, both models should be amalgamated into a unified formulation, particularly in regard to vegetal encroachment.

2.10 Conclusions

In order to overcome the constraint of constant, specified width associated with the older HIPS-based models of meander migration, this paper implements the framework for self-driven width variation of Parker et al (2011), and specifies closures that account for both erosional and depositional bank processes. The closure for bank erosion is based on slump-block mitigated natural armoring; it covers the range from vanishing armoring (purely non-cohesive bank) to a limit where slump block armoring is so dominant that non-cohesive bank processes can be neglected. This natural armoring prevents runaway erosion of unprotected banks, and thus the runaway widening to the braided state, that is characteristic of experiments on meandering in purely non-cohesive material.

The closure for bank deposition is based on a default rate of vegetal encroachment onto the point bar. The encroachment rate decreases below this value with increasing near-bank shear stress at the bed. Both models are linked to each other through a threshold channel forming Shields number. This Shields number specifies the bankfull hydraulic geometry of a straight channel. If the bed Shields number near a bank exceeds the channel-forming value, the bank erodes; otherwise it deposits.

The model in its final form has, three major input parameters which govern bank erosion and depositional processes: a reference erosion rate i_{Eref}^{\sim} that is a function of measurable bank and slump block parameters, such as characteristic slump block lifetime; a reference deposition rate i_{veg}^{\sim} specifying a nominal rate of vegetal encroachment in the absence of floods; and the channel-forming Shields number \dagger^*_{form} that sets both bankfull geometry and the threshold between bank erosion to bank deposition.

To complete the model of channel migration, the bank submodels have been linked to an in-channel morphodynamic submodel from which near-bank shear stresses are computed. Here we have used a nonlinear flow and bed morphodynamic model based on the iterative solution proposed in Camporeale et al. (2007). The coupling between in-channel and bank processes has been simplified by assuming a quasi-steady condition such that the time scale of bank morphodynamics is significantly larger than in-channel flow and bed morphodynamics.

The full model has been applied to the simplified cases of evolution of a straight reach, and evolution of a bend with spatially constant curvature. Input parameters are based on a reach of the Vermillion River, MN, USA. The values for the reference erosion and deposition rates i_{Eref}^{\sim} and i_{veg}^{\sim} used in the model have been chosen such that they reproduce observed migration rates.

The straight-channel simulations verify that the model overcomes the limitations of the HIPS formulation. It is able to predict the process of channel narrowing (widening) to equilibrium bankfull conditions for an overwide (overnarrow) initial channel.

The bend flow simulations were performed under the constraint that the centerline elevation difference over the modeled reach remains constant. This dictates a centerline slope that declines as the channel migrates outward, so mimicking the reduction in slope experienced by a meandering channel as it increases its sinuosity due to migration. In this configuration, a final equilibrium is replaced by an asymptotic state where both banks are moving very slowly in the same direction and at nearly the same rate, and bankfull width very slowly declines.

The use of a constant, specified formative Shields number in the bend modeling brings to light a persistent problem: the channel undergoes excessive narrowing. We resolve this problem by appealing to data, which show a clear tendency for bankfull Shields number to increase with slope. A slope-dependent relation based on the regression fit of Li et al (submitted, see Appendix B) proves sufficient to resolve the problem.

For the bend case, the model identifies 5 regimes of channel evolution towards an asymptotic state. To define them we consider a bend for which the outer bank is on the right-hand side. At the asymptotic state, the migration rate of the left, inner bank \dot{n}_{LB} is nearly equal to that of the right, outer bank \dot{n}_{RB} , both being very small, positive numbers. Thus both banks are moving very slowly at nearly the same rate and in the same outward direction. The five regimes of evolution toward the asymptotic state are as follows: inward migration ($\dot{n}_{LB} < 0, \dot{n}_{RB} < 0$); both banks erode ($\dot{n}_{LB} < 0, \dot{n}_{RB} > 0$); both banks deposit ($\dot{n}_{LB} > 0, \dot{n}_{RB} < 0$); outward migration with bar push ($\dot{n}_{LB} > \dot{n}_{RB} > 0$); and outward migration with bank pull $\dot{n}_{RB} > \dot{n}_{LB} > 0$.

The model shows how, depending upon the choice of $\tilde{\tau}_{Eref}$ and $\tilde{\tau}_{veg}$, an overwide initial channel can first undergo narrowing through deposition at both banks, narrow further by bar push, and then reach the asymptotic state. An overnarrow initial channel can first undergo widening through erosion at both banks, continue widening via bank pull, and then reach the asymptotic state. Increasing $\tilde{\tau}_{Eref}$ pushes the system toward bank pull, and increasing $\tilde{\tau}_{veg}$ pushes it toward bar push.

This work represents a first step towards understanding the evolution of width in meandering river systems. It has been applied to a fully meandering channel up to and beyond cutoff (Chapter 4). The present analysis is intended to provide deeper insight into how the model works, which otherwise might be obscured in the case of an evolving meandering channel with a complex planform.

Acknowledgements

This research represents a contribution of the National Center for Earth-surface Dynamics, a Science and Technology Center funded by the US National Science Foundation (agreement EAR-0120914). The authors gratefully acknowledge the assistance of E. Viparelli, J.W. Lauer, and K. Asahi in performing this research. The terms “bar push” and “bank pull” were introduced to the authors by W.E. Dietrich.

Tables

<i>Parameter</i>	<i>Vermillion</i>	<i>Trinity</i>	<i>Wabash</i>
\tilde{Q}_{bf} (m^3/s)	10	700	4000
\tilde{B}_{bf} (m)	15	190	285
\tilde{H}_{bf} (m)	0.88	3.85	6.4
S	0.00058	0.000124	0.00012
\tilde{D}_s (mm)	2	0.35	0.74
\ddagger_{bf}^*	0.16	0.83	0.53
I_f	0.05	0.18	0.08
$\tilde{r}_{non,E,s}$ (m/yr)	76.9	107.4	48.7
$\tilde{r}_{E,abs,bend}$ (m/yr)	0.75	2.3	7.75

Table 2.1. Estimates of bank erosion rate assuming flood conditions

Variable	Value	Units	Description
$\tilde{H}_{b,LB}; \tilde{H}_{b,RB}$	1	m	Non-cohesive bank height, approximated from bankfull depth (Lauer and Parker, 2008)
$\tilde{H}_{c,LB}; \tilde{H}_{c,RB}$	0.5	m	Cohesive layer thickness, equated to mean elevation difference between banks Δy (Lauer and Parker, 2008) Total cut-bank height (i.e. 1.5m) is approx. to mean total station bank height measurement along a select reach of the river.
S	0.00058		Initial centerline slope
$S_{s,LB}; S_{s,RB}$	2; -2		Channel bank slope
$\} _{pc,LB}; \} _{pc,RB}$	0.6		Cohesive layer porosity
$\} _{pb,LB}; \} _{pb,RB}$	0.4		Non-cohesive layer porosity
\tilde{D}_c	0.5	m	Characteristic size of slump blocks, average of measured 14 slump blocks within
l_f, I_{frefl}	0.05		Flood intermittency
\tilde{i}_{vegB}	0.79	m/yr	Base case natural rate of vegetal encroachment, rule of thumb 5% of bankfull width. Estimate in line with bar deposition rate D_{bar} / bankfull depth estimates from Lauer and Parker (2008)
$\tilde{i}_{E,refB}$	1.47	m/yr	Base case reference erosion rate computed from (2.26) assuming a reference slump block lifetime $T_{cref} = 2$ yrs

Table 2.2. Summary of input parameters for numerical modeling

Figures



Figure 2.1. Images of the meandering Vermillion River, Minnesota, USA. Left: an eroding bank armored by slump blocks. Right: Contact between the upper cohesive layer with roots of vegetation and lower non-cohesive layer.

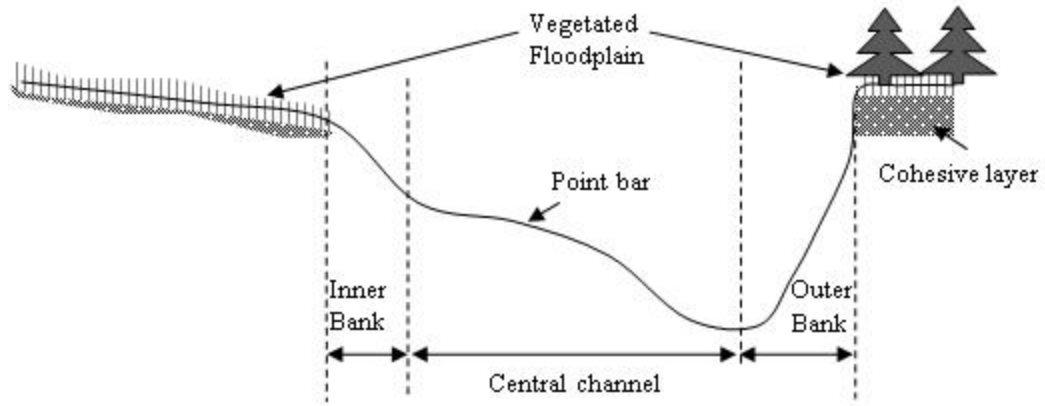


Figure 2.2: Definition sketch of channel cross-section.

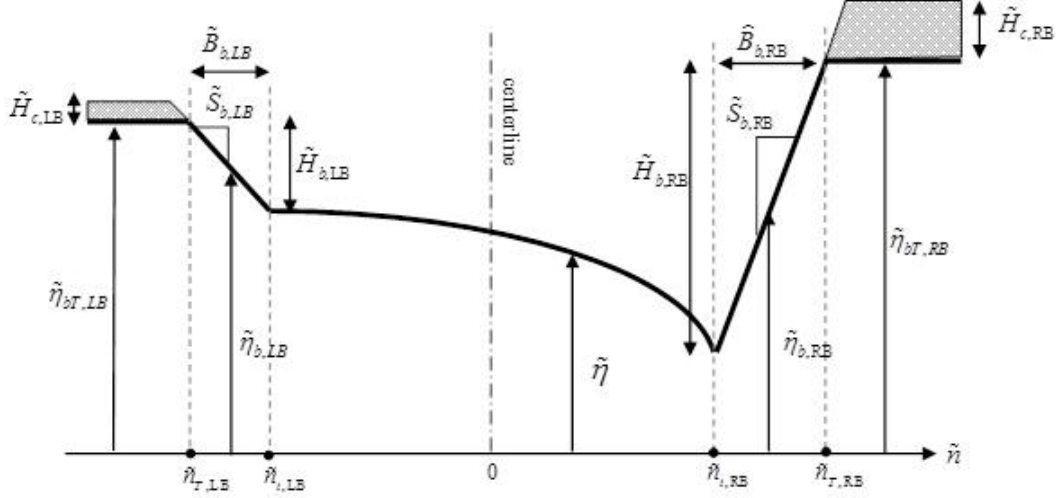


Figure 2.3: Definition sketch of model channel cross-section. The shaded portion here represents the cohesive layer. All other parts of the cross-section are considered non-cohesive. For each bank j (LB for left bank and RB for right bank), $\tilde{H}_{b,j}$, $\tilde{H}_{c,j}$, $\tilde{S}_{b,j}$, and $\tilde{B}_{b,j}$ denote, respectively, the cohesive layer thickness, the non-cohesive bank height, non-cohesive bank slope and non-cohesive lateral bank width (measured from the bank toe at $\tilde{n} = \tilde{n}_{t,j}$ to the vegetation line at $\tilde{n} = \tilde{n}_{T,j}$, where \tilde{n} is the transverse coordinate). $\tilde{y}_{b,j}$ denotes the bed elevation along the bank with $\tilde{y}_{b,j} = \tilde{y}_{bt,j}$ at $\tilde{n} = \tilde{n}_{t,j}$ and $\tilde{y}_{b,j} = \tilde{y}_{bT,j}$ at $\tilde{n} = \tilde{n}_{T,j}$. The tildes denote dimensioned parameters.

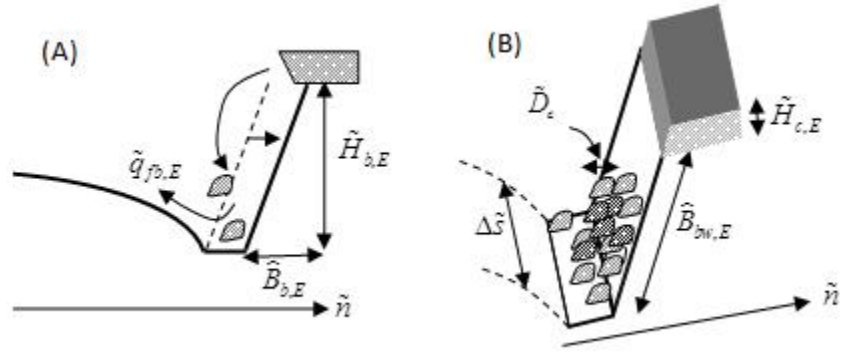


Figure 2.4: (a) Schematic of erosion process: $\tilde{q}_{fb,E}$ denotes the transverse non-cohesive sediment load delivered into the channel region, $\tilde{H}_{b,E}$ denotes the thickness of the non-cohesive layer and $\tilde{B}_{b,E}$ denotes the width of the non-cohesive layer. (b) Definition sketch of armoring parameters.

The key armoring parameters denoted are the thickness of the cohesive layer that creates the slump blocks $\tilde{H}_{c,E}$, the arc width of the zone available to be covered by slump blocks $\tilde{B}_{bw,E}$ and the characteristic size of the slump blocks \tilde{D}_c which scales with the cohesive layer thickness $\tilde{H}_{c,E}$

. \tilde{s} and \tilde{n} denote the streamwise and transverse coordinates respectively, the subscript “E” denotes that the bank is eroding and the tildes indicates dimensioned parameters.

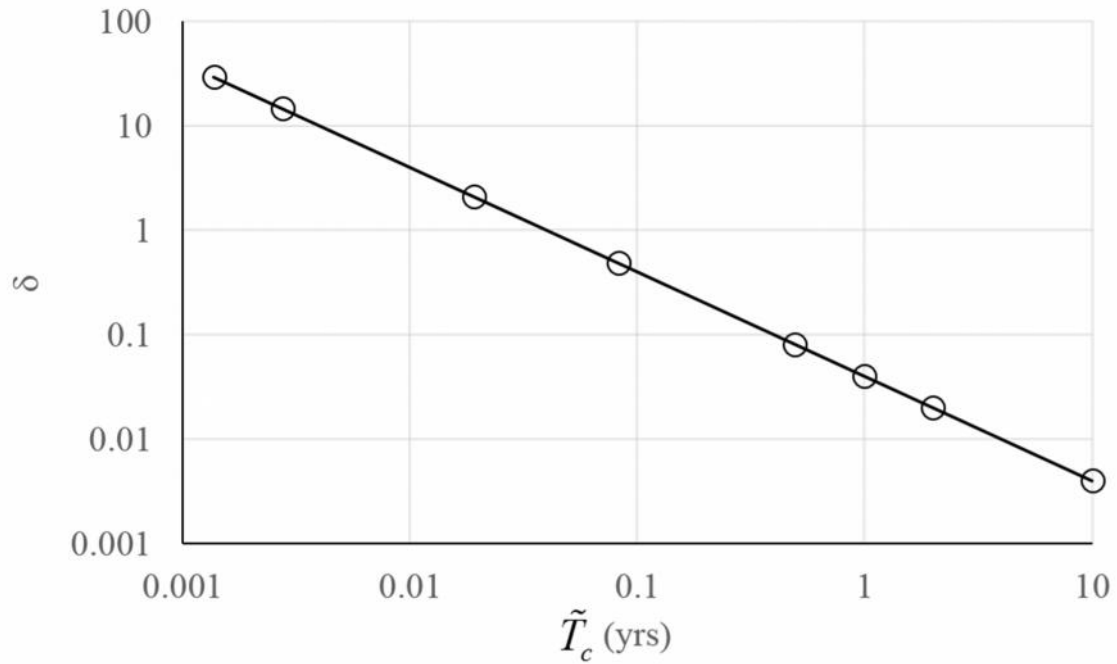


Figure 2.5: Dimensionless parameter δ reduces with increasing slump block residence time \tilde{T}_c .

Here δ is the ratio of the bank migration rate under the condition of complete slump block control to that for a completely non-cohesive bank.

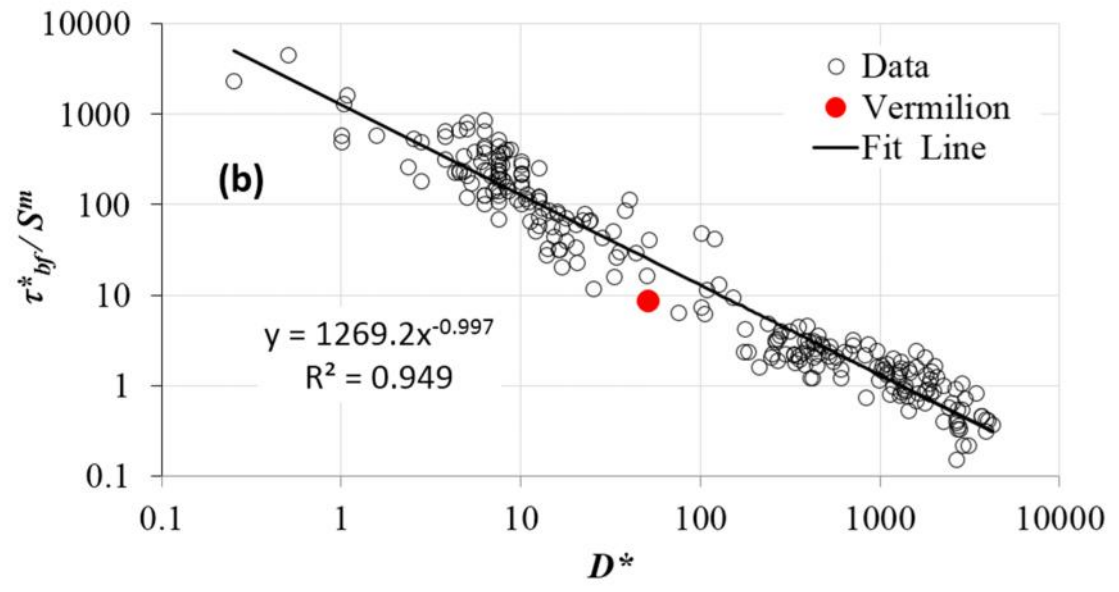
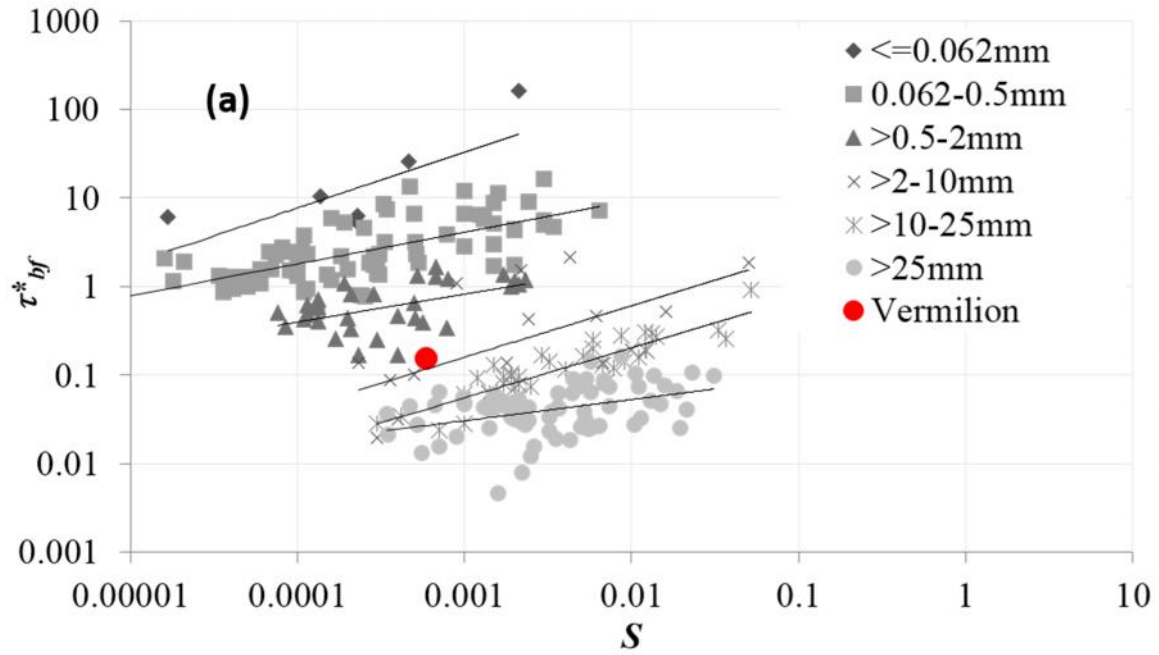


Figure 2.6: (a) Bankfull Shields number versus channel slope (b) Similarity collapse showing normalized bankfull shields number versus grain size D^* . Dataset for bankfull geometry are from Parker et al. (2007) and Wilkerson and Parker (2010). The similarity collapse is due to Li et al. (2013). A point for the reach of the Vermilion River considered here has been added to both figures.

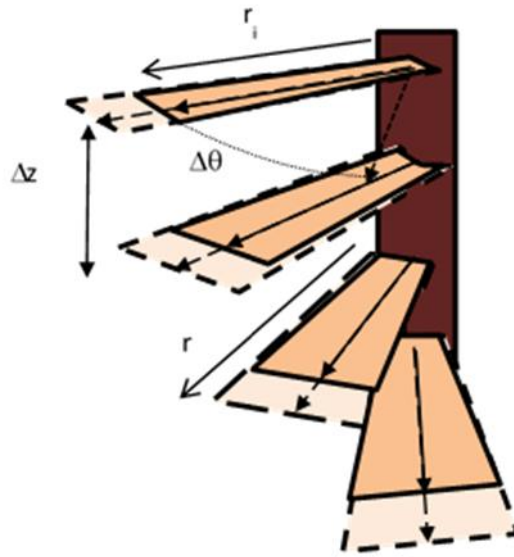
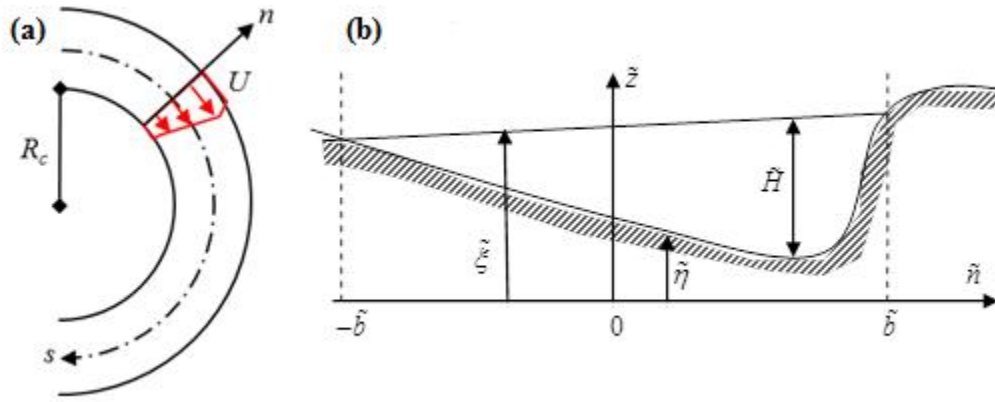


Figure 2.7: Reach of a channel with spatially constant curvature. The channel may undergo temporal change due to migration and width variation. (a) Plan view. (b) Cross-section (c) Spiral staircase illustrating the constraint of constant elevation difference Δz along a reach, the centerline radius of curvature is changing in time.



Figure 2.8: The Vermillion Rive near Empire, MN, USA. Flow is from left to right. Image Courtesy USGS. For scale, average channel width is 15m.

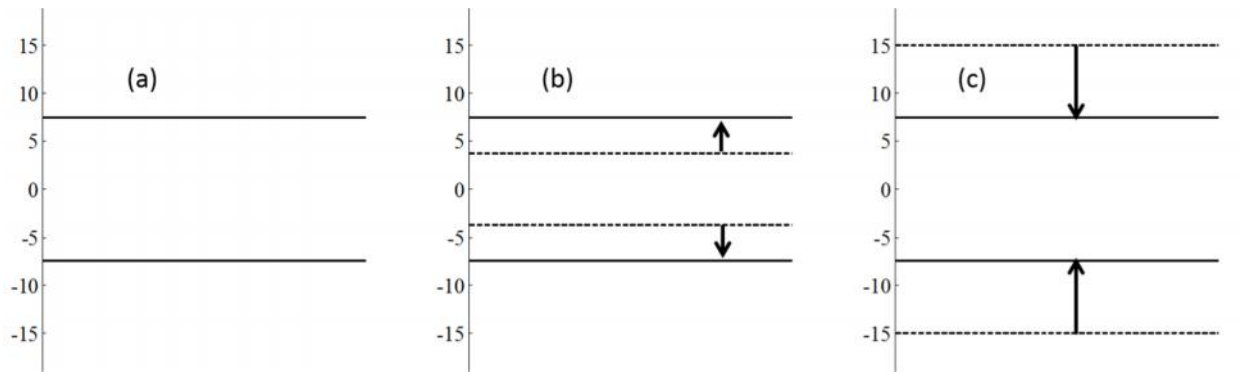


Figure 2.9A: Width adjustment for straight channel with initial width $\tilde{B}_i =$ (a) \tilde{B}_{bf} (b) $0.5 \tilde{B}_{bf}$ and (c) $2 \tilde{B}_{bf}$. Dashed line is initial channel and continuous line is final channel

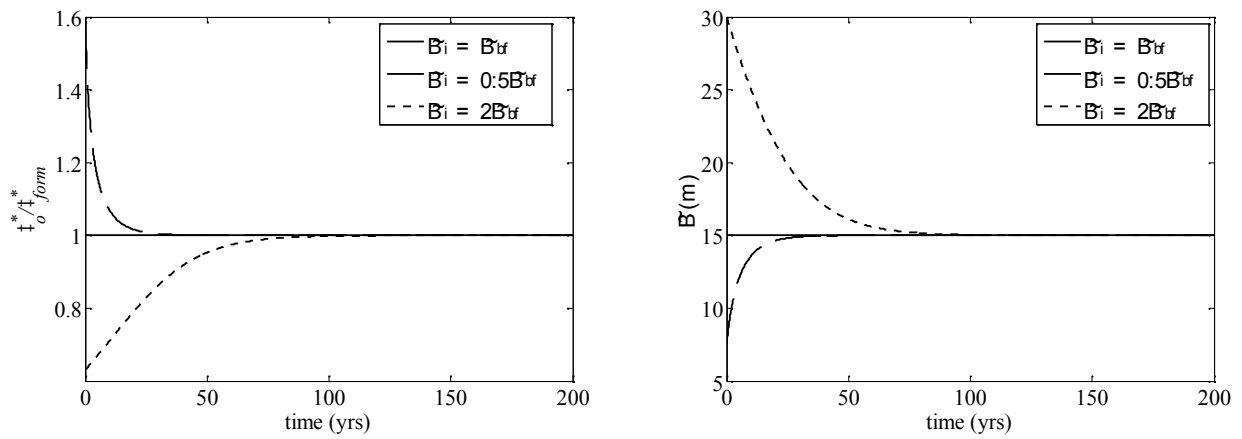


Figure 2.9B: Width adjustment for straight channel with initial with $\tilde{B}_i = \tilde{B}_{bf}$, $0.5 \tilde{B}_{bf}$ and $2 \tilde{B}_{bf}$
 (a) Shields number versus time (b) channel half-width versus time

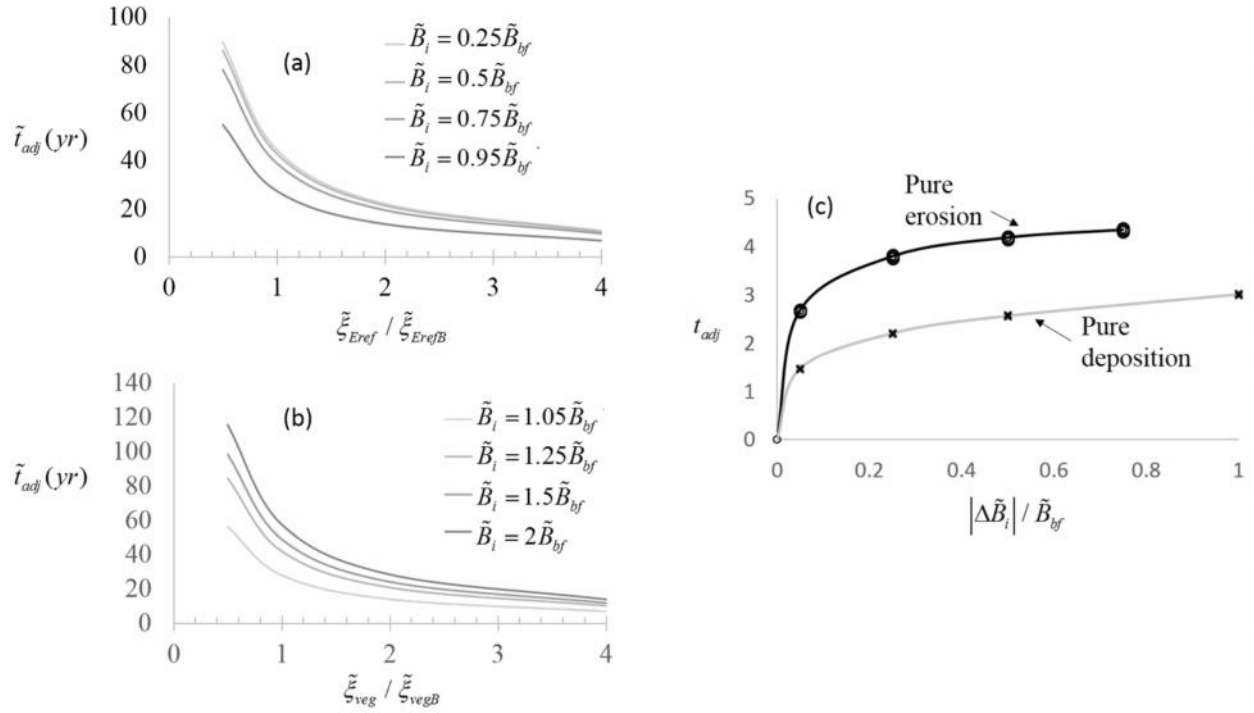


Figure 2.10: Width adjustment for straight channel. (a) Characteristic time of adjustment for an initially over-narrow channel as a function of initial width \tilde{B}_i and reference erosion rate $\tilde{\zeta}_{Eref}$. (b) Characteristic time of adjustment for an initially over-wide channel as a function of initial width \tilde{B}_i and reference vegetation encroachment rate $\tilde{\zeta}_{veg}$ (c) Dimensionless characteristic time of adjustment versus absolute deviation from equilibrium width, for the purely erosional (widening) case and the purely depositional (narrowing) case.

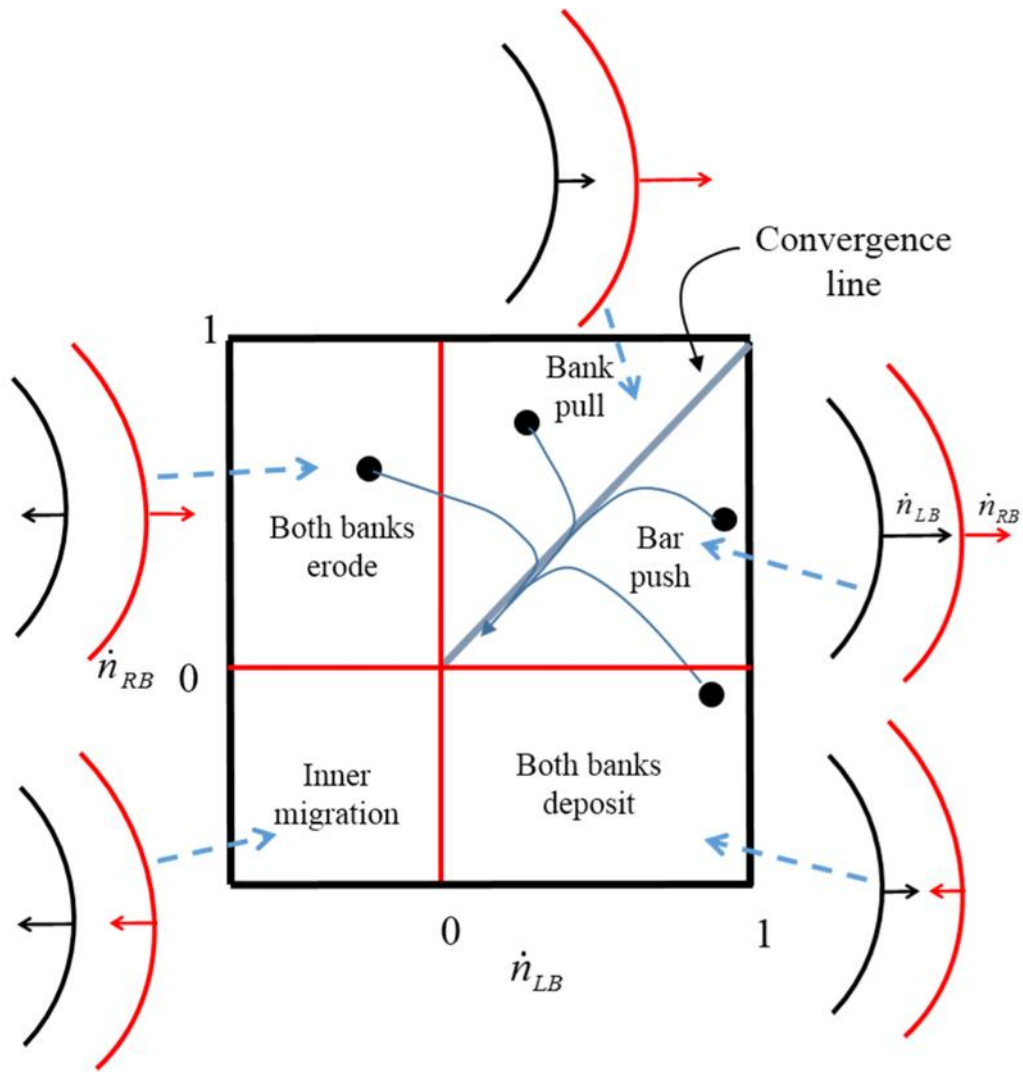


Figure 2.11: Schematic plot in phase space of bank migration showing the different phases of channel bank interaction. Here \dot{n}_{LB} and \dot{n}_{RB} are the migration rates of the left and right banks, respectively.

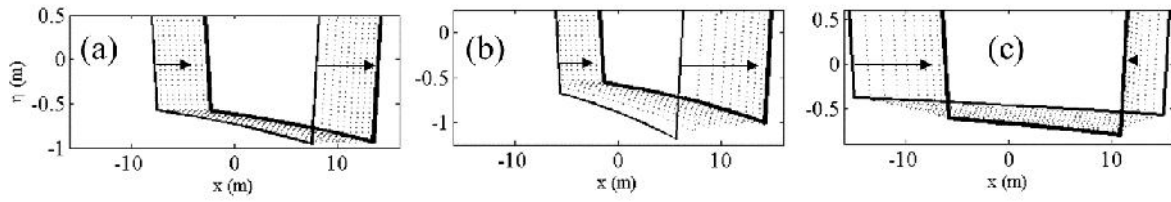


Figure 2.12A: Width adjustment for curved channel ($C = 0.1$) with initial width $\tilde{B}_i =$ (a) \tilde{B}_{bf} (b) $0.75 \tilde{B}_{bf}$ and (c) $2 \tilde{B}_{bf}$. Dashed line is initial channel and continuous line is final channel

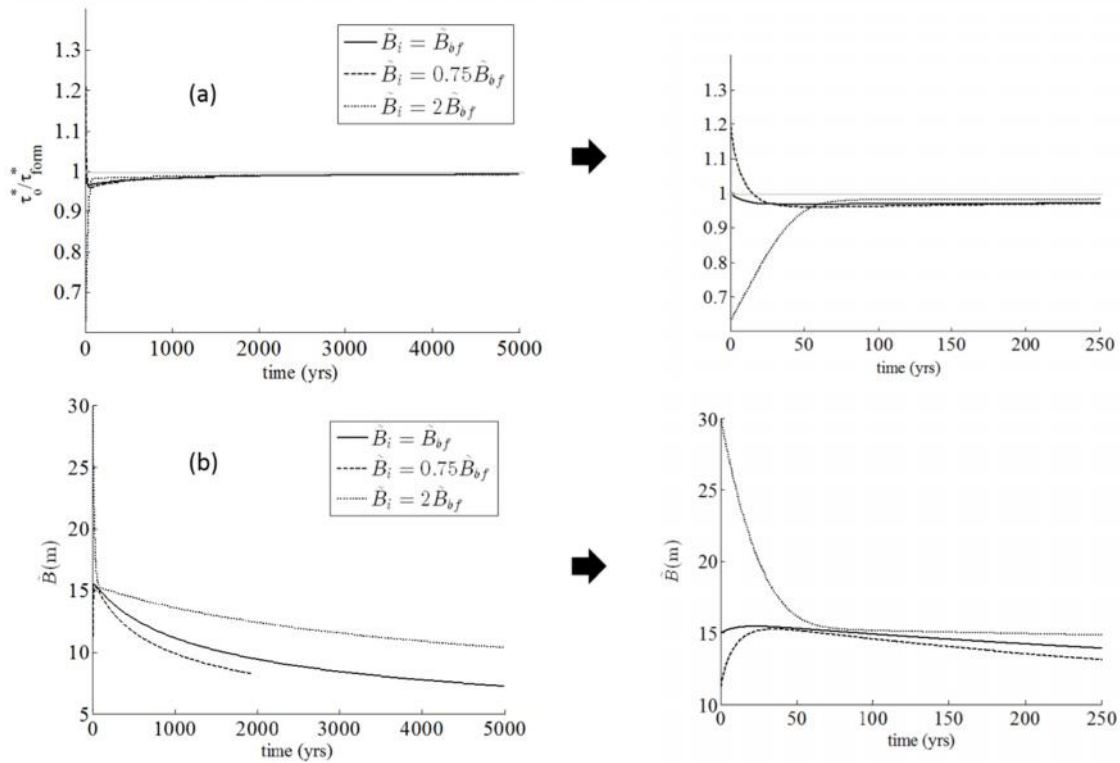


Figure 2.12B: Evolution of bend ($C = 0.05$) with initial width $\tilde{B}_i = \tilde{B}_{bf}$, $0.75 \tilde{B}_{bf}$ and $2 \tilde{B}_{bf}$ (a) Shields number versus time. (b) Channel width versus time. In each case, the diagram on the

right is a magnification of the diagram on the left, so as to illustrate the early stage of channel evolution. Here τ_{Eref}^{\sim} and τ_{veg}^{\sim} are the base values given in table 2.2.

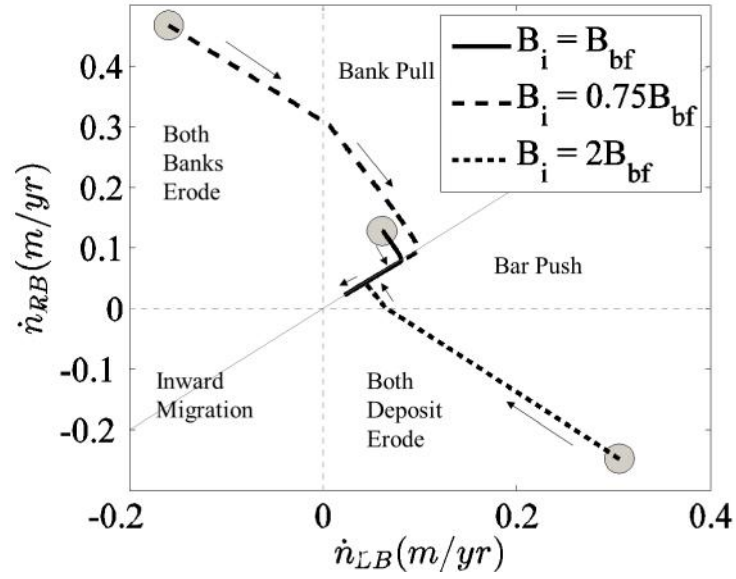


Figure 2.13: Plot in phase space for bank migration of bends of dimensionless curvature $C = 0.05$ with initial widths $\tilde{B}_i = \tilde{B}_{bf}$, $0.75\tilde{B}_{bf}$ and $2\tilde{B}_{bf}$. The parameters \tilde{i}_{Eref} and \tilde{i}_{veg} are the base values given in Table 2. The circles indicate starting point for different initial widths.

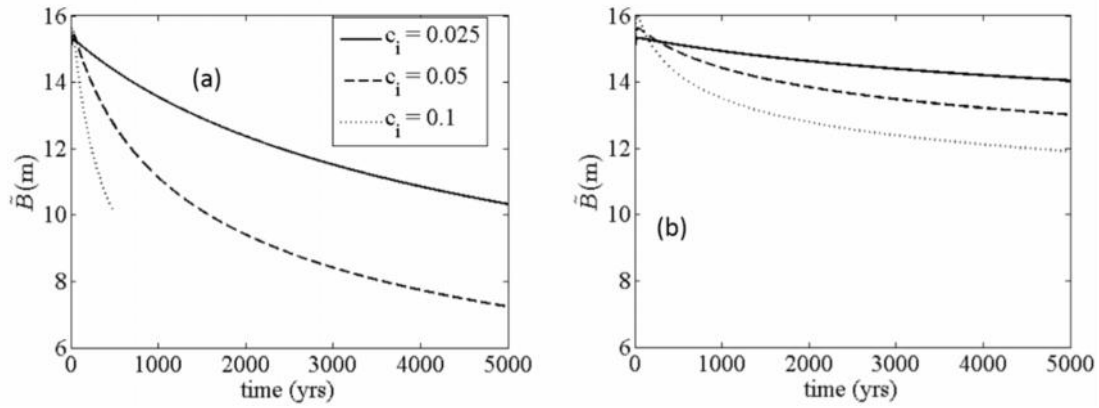


Figure 2.14: Evolution of bend with initial width $B_i = B_{bf}$ and initial dimensionless curvatures $C_i = 0.025, 0.05$ and 0.1 . (a) Case of slope-independent formative Shields number. (b) Case of slope-dependent formative Shields number. The parameters $\tilde{\tau}_{Eref}$ and $\tilde{\tau}_{veg}$ are the base values given in Table 2. The initial Shields number is the same. The circles indicate starting point for different initial widths. Channel narrowing is much more subdued in the case of slope-dependent Shields number.

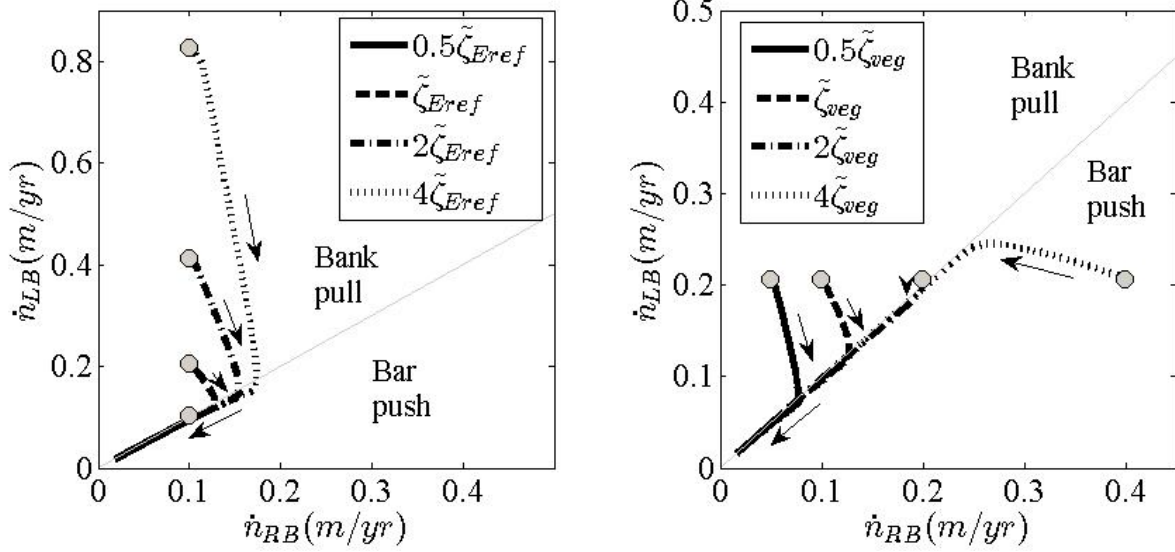


Figure 2.15: Plot in phase space for bank migration of bend with initial width $\tilde{B}_i = \tilde{B}_{bf}$ for dimensionless curvature $C = 0.1$. Left: Illustration of sensitivity to the reference erosion rate $\tilde{\zeta}_{Eref}$. Right: Sensitivity to vegetal encroachment rate $\tilde{\zeta}_{veg}$.

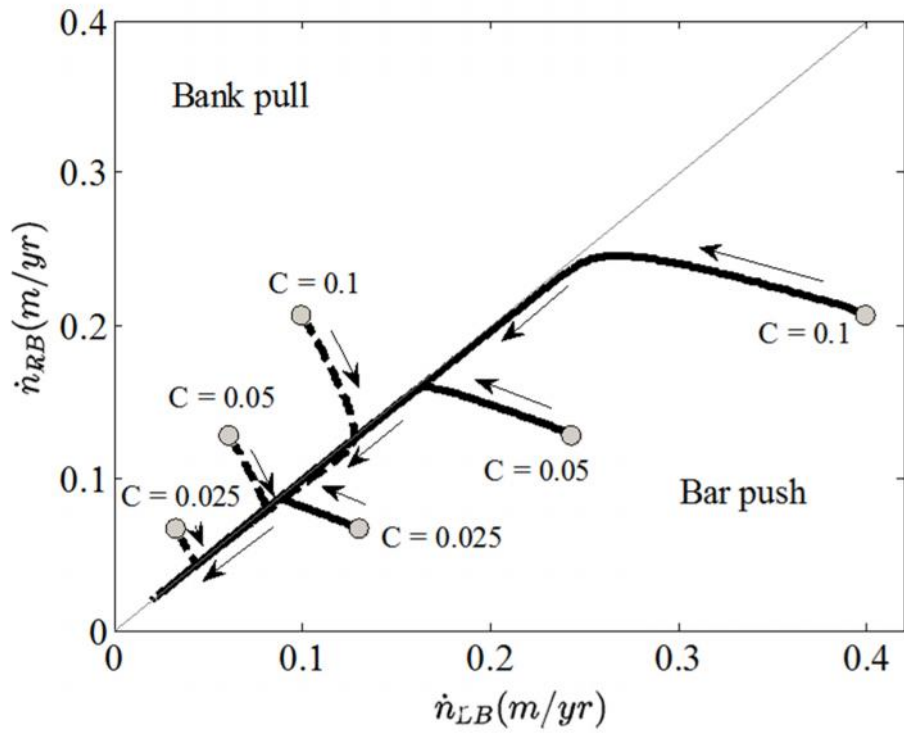


Figure 2.16: Plot in phase space for bank migration of curved channel with initial width $\tilde{B}_i = \tilde{B}_{bf}$ and initial dimensionless curvatures $C = 0.025, 0.05$ and 0.1 . In the three cases illustrating bank pull, \tilde{i}_{Eref} and \tilde{i}_{veg} are the base values in Table 2. In the three cases illustrating bar push, \tilde{i}_{Eref} is set to the base value, \tilde{i}_{veg} set to 4 times the base value.

Chapter 3

COEVOLUTION OF WIDTH AND SINUOSITY IN MEANDERING RIVERS

Abstract

This research explores the coevolution of planform and channel width in a freely meandering river. In the model described here, width evolution is coupled to channel migration through two submodels, one describing bank erosion and the other describing bank deposition. Bank erosion is modeled as erosion of purely non-cohesive bank material damped by natural armoring due to basal slump blocks, and bank deposition is modeled in terms of a flow-dependent rate of vegetal encroachment. While these two submodels are specified independently, the two banks interact through the medium of the intervening channel; the morphodynamics of which is described by a fully nonlinear depth-averaged morphodynamics model. Since both banks are allowed to migrate independently, channel width is free to vary locally as a result of differential bank migration. Through a series of numerical runs, we demonstrate co-evolution of local curvature, width and streamwise slope as the channel migrates over time. The correlation between the local curvature, width and bed elevation is characterized and results show how this relationship is affected by governing parameters. The results also show that, by varying a parameter representing the ratio between a reference bank erosion rate and a reference bank deposition rate, the model is able to reproduce the broad range of river width-curvature correlations observed in the field. This research represents a step towards providing general metrics for predicting width variation patterns in river systems.

3.1 Introduction

Meandering rivers are one of the very common channel forms found in both sedimentary and non-sedimentary environments. They develop in alluvial rivers wandering through floodplains, in incised bedrock rivers, in glacial meltwater systems and even in submarine systems, where turbidity currents form gigantic meandering channels on submarine fans (e.g. Leopold and Wolman, 1960; Hack, 1965; Imran et al. 1999; Seminara, 2006; Karlstrom et al., 2013; Konsoer et al., 2013). Understanding the morphology and evolution of meandering rivers in nature has long attracted the attention of the scientific community, in the fields of fluvial geomorphology (e.g. Hooke, 2007, 2008), fluid mechanics (e.g. Seminara, 2006) and hydraulic engineering (e.g. Duan and Julien, 2010).

The last three decades have seen the development of a mechanistic framework for the quantitative understanding of meander dynamics. The mechanistic bend theory (e.g., Ikeda et al., 1981; Parker et al., 1982) describing meandering rivers as products of bend instability has led to the quantitative determination of many key parameters in meander development, and has also led to the development of models that establish the intrinsic ability of meander trains to evolve from incipient meander formation to and beyond neck cutoff. The basis for the formulation is the groundbreaking work on secondary flow in bends (Rozovskii, 1957) and its contribution to the morphodynamics of alluvial bends and meandering rivers (Engelund, 1974 and Ikeda et al., 1976). Hasegawa (1977), Ikeda et al. (1981), Parker et al. (1982) and Howard and Knutson (1984) showed how the application of a simple relation between the transverse variation of streamwise velocity and the migration rate of channel centerline (HIPS relation below) allows description of channel migration. Further contributions to the mechanics of meander migration, as well as the description

of flow and morphodynamics of meandering rivers needed to understand this mechanics, including (among many), Smith & McLean (1984), Kitanidis & Kennedy (1984), Howard & Knutson (1984); Struiksmas et al. (1985), Blondeaux & Seminara (1985), Parker & Andrews (1985, 1986), Colombini et al. (1987), Nelson & Smith (1989), Johannesson & Parker (1989), Howard (1992, 1996), Sun et al., (1996), Zolezzi & Seminara (2001), Camporeale et al. (2007, 2008), Frascati & Lanzoni (2009) and Luchi et al. (2012), have brought us to the present, relatively advanced state of understanding of the morphodynamics of migrating meandering rivers.

A major gap nevertheless exists in our understanding of the morphodynamics of meander planform evolution. This gap pertains to the problems of how rivers determine their own widths, and how sinuosity and width variation co-evolve. This issue can be best highlighted by considering the most commonly used relation describing channel migration, i.e. the Hasegawa-Ikeda-Parker-Sawai, or HIPS formulation (Hasegawa, 1977; Ikeda et al., 1981).

The HIPS formulation for bank migration has been summarized in Parker et al. (2011). In this formulation, the river is prescribed to have a constant width, here taken to be $2\tilde{b}$, where \tilde{b} is channel half-width, and the tilde denotes a parameter with dimensions. The local normal rate of shift $\dot{\tilde{x}}$ of the channel centerline is taken to be linearly proportional to the difference in the near-bank, depth-averaged streamwise velocity \tilde{U} between the two banks, so that

$$\dot{\tilde{x}} = E\Delta\tilde{U} = E\left(\tilde{U}\Big|_{\tilde{n}=\tilde{b}} - \tilde{U}\Big|_{\tilde{n}=-\tilde{b}}\right) \quad (3.1)$$

where \tilde{n} is normal distance from the channel centerline.

In the above relation, the streamwise velocities are interpreted not to be evaluated at $\pm\tilde{b}$ (where they would be vanishing), but rather just outside the associated near-bank boundary layer. In the above relation, E is a prescribed dimensionless migration coefficient. This same formulation for planform evolution has also been cast in an equivalent intrinsic form by Seminara et al. (2001).

The HIPS formulation for channel migration has been applied to the problem of meander migration using a wide variety of fluid dynamic and in-channel morphodynamic formulations, the sophistication of which has gradually increased in time. In addition, the cases studied have varied from the evolution of single bends to the evolution of entire floodplains characterized by many bend cutoffs. Examples of such applications include Beck et al. (1983), Parker et al. (1983), Howard and Knutson (1984), Blondeaux and Seminara (1985), Parker and Andrews (1986), Beck (1988), Crosato (1990), Howard (1992), Sun et al., (1996), Stolum (1996), Lanzoni and Seminara (2006), Camporeale et al. (2007, 2008) and Frascati and Lanzoni (2009, 2010). In all of these examples, both half-width \tilde{b} and migration coefficient E are *prescribed* constants.

In several recent examples, e.g. Gurneal and Rhoads (2011) and Motta et al. (2012b), the effect of either a *prescribed variation* in migration coefficient E or a *prescribed rule for variation* has been used to study, for, example, the effect of floodplain heterogeneity on patterns of meander migration. These studies, however, retain the assumption of prescribed, constant width. Neither these nor the previously-quoted contributions addresses the issue how a river establishes its own width. In addition, the migration coefficient E has remained an empirically useful parameter with no clear physical basis.

The physics behind the problem of bank erosion has been studied by a number of authors

including Darby and Thorne (1996), Darby et al. (2007) and Langendoen and Simon (2008). Nagata et al. (2000), Ruther and Olsen (2007) and Duan and Julien (2010), for example, present models for meander migration with a physically-based formulation for bank erosion, but channel width monotonically increases over time due to the lack of a description of bank deposition. Motta et al. (2012a) also include a more physically-based formulation for bank erosion, but the channel migrates while maintaining constant width under the constraints of the HIPS formulation.

The assumption of a temporally constant width in a meandering river is partly justified by field observations over geomorphic time, which suggest that many rivers tend to maintain a fairly constant mean channel width as they migrate (e.g. Lagasse et al., 2004). However, many other field observations have clearly shown that natural rivers routinely undergo time periods of width adjustment as the river responds to changes in flow regime and other environmental factors (e.g. Pizzuto, 1994; ASCE, 1998). Spatially constant width is thus, only a first crude approximation. Indeed, systematic spatial width variation patterns have been documented in many meandering rivers by e.g. Brice (1982) and Lagasse et al. (2004).

In recent years, the in-channel morphodynamics of channels with *prescribed variation* in width has been the subject of considerable research. The case of a straight channel with varying width has been studied by Bittner (1994), Repetto et al. (2002), Wu and Yeh (2005) and Wu et al (2011). Meandering rivers with *prescribed variation* of width have been studied by Luchi et al. (2010, 2011), Zolezzi et al. (2012) and Frascati and Lanzoni (2013). None of these analyses include, however, physically-based descriptions of the processes of bank erosion and deposition necessary to establish channel width itself, much less width variation.

The work of Solari and Seminara (2005) and Luchi et al. (2012) offer a physical basis for patterns of width variation. They hypothesized that, were the banks to be free to adjust, a pattern of width variation would prevail, according to which the centerline streamwise free surface slope would become constant. The analysis does not, however, describe the processes of bank erosion and deposition that might lead to such an adjustment of water surface slope.

An understanding of the co-evolution of meander planform and width variation must then be predicated on a deeper understanding of the processes of both bank erosion and deposition. Mosselman (1998) pointed out that it is not possible to accurately capture channel migration in a model that allows bank erosion alone. Mosselman et al. (2000) made the important step of incorporating both erosional and depositional processes into a model of channel shift, albeit in the context of anabranches of the braided Brahmaputra-Jamuna River, Bangladesh.

Here we study the co-evolution of planform and width in the context of the recent framework of Parker et al (2011), which allows channel banks to migrate independently. In this formulation: bank erosion is modeled as erosion of purely non-cohesive bank material damped by natural armoring due to basal slump blocks; and channel deposition is modeled as a function of vegetal encroachment damped by flood flow. Since the banks are allowed to move independently, channel width is allowed to vary locally as a result of differential bank migration. Eke et al. (submitted, Chapter 2) describe closures for a full implementation of this model formulation which link the processes of bank erosion and deposition to a reach-averaged channel-formative Shields number τ_{form}^* . This parameter acts as a threshold below which bank deposition occurs, and above which bank erosion occurs. A brief review of the model closures is presented in the following sections.

Eke et al. (submitted, Chapter 2) has applied this formulation to the case of the evolution of a spatially constant-curvature channel. They showed that for such migrating bend flows, the river converges to an asymptotic state where both erosion and deposition are roughly equal, and where channel width is slowly reducing in time, as streamwise slope reduces and curvature decreases in time. The paper delineates four regimes of bank interaction, i.e. both banks eroding, both banks depositing, bar push (faster migration on the inside of bend) and bank pull (faster migration on the outside of a bend). The analysis shows how a river bend can transition from one regime to another as it evolves towards the asymptotic state.

The work goes beyond Eke et al. (submitted, Chapter 2) by extending the implementation of the model to the case of a freely meandering river rather than a bend of spatially constant curvature. The outline for the rest of this chapter is as follows: In Section 3.2 we document observable trends of width variation from a few river reaches. Section 3.3 is an overview of bankfull geometry as it relates to the formative Shields number. Section 3.4 details the model formulation for flow and bed morphodynamics with varying width, along with the formulation for bank morphodynamics outlined in Eke et al. (submitted, Chapter 2). To show how channel curvature, width and bed topography co-evolve, Section 3.5 details numerical experiments on the growth and development of an idealized sequence of periodic meander bends up till near cut-off conditions. Discussion and conclusions are in Sections 3.6 and 3.7 respectively.

3.2 Observed patterns of width variation in meandering rivers

Brice (1982) and Lagasse et al. (2004) observe that while nearly constant-width channels do exist, the majority of actively migrating channels exhibit spatial width variation. Channels that are

systematically wider at bends apexes (where curvature is highest) tend to exhibit the highest migration rates. They also identify another class of rivers for which width variation is uncorrelated with curvature, and migration rates are low.

Most of the observations of Brice (1982) and Lagasse et al. (2004) were based on channel width defined from vegetation line to vegetation line. Figure 3.1 shows three reaches: the Ob River, Russia, the Trinity River, Texas, USA and the Vermillion River, Minnesota, USA. All three reaches display a pattern of width variation that correlates with centerline curvature. In terms of vegetation line, the first two reaches tend to be wider at bend apexes (maximum curvature) relative to crossings (vanishing curvature). In the third reach, however, this pattern is reversed: the channel tends to be narrower at apexes. Channel width can also be defined, however, in terms of water margin to water margin. In the case of the Trinity River, figure 3.1b shows that the channel defined by vegetation lines is wider at apexes, but that the channel defined by water margins is narrower at apexes. The former may reflect bankfull flow conditions, whereas the latter reflects below-bankfull stage. This stage dependence has been pointed out by Luchi et al. (2011).

In order to analyze width-curvature relations, we used reaches of the Vermillion River near Empire, MN and the Trinity River downstream of Livingston Dam in Eastern Texas, (figure 3.1). We also studied the reach of the Pembina River near Rossington in Alberta, Canada (figure 3.2). Table 3.1 gives the characteristics of each reach. The data sources are as follows: Vermillion River; Lauer and Parker (2008); Trinity River, Smith (2012); Pembina River, Beck et al. (1983). All three reaches are highly sinuous and actively migrating (Lauer and Parker, 2008; Smith, 2012; Beck, 1983).

The channel banklines were digitized from aerial photographs using visible vegetation lines, and the channel centerline was obtained from digitized banklines in a way similar to Lauer and Parker (2008). Local half-widths were obtained during the iterative procedure as the tangential distance from the centerline to the bank line at each node.

Figure 3.3 shows the downstream variation in curvature and width for the Vermillion and the Trinity River reaches. Figure 3.4 shows linear regressions of half-width against curvature for each reach. Here dimensionless curvature c and half-width b are:

$$c = \frac{\tilde{b}_o}{\tilde{R}_c}; \quad b = \frac{\tilde{b}}{\tilde{b}_o} \quad (3.2)$$

where \tilde{b} and \tilde{R}_c denote local half-width and centerline radius of curvature respectively and \tilde{b}_o denotes the reach averaged channel half-width. Again, tildes denote dimensioned parameters.

The cases of the Vermillion and Trinity River reaches of figures 3.3 and 3.4 highlight the range of tendencies in width variation in meandering rivers. In the Vermillion River, sections near the crossings ($c \sim 0$) tend to be wider than sections near the apexes ($c \sim 0.3$), but the variation is weak (fractional width variation of - 0.04 as c varies from 0 to 0.35). In the Trinity River, sections near apexes tend to be wider than those near crossings, and the variation is notably stronger (fractional variation of 0.19 as c varies from 0 to 0.35).

The pattern observed for the Trinity River is in general agreement with the trends reported in Brice (1982) and Lagasse et al (2004). Field data on more than 1500 meander bends reported by Lagasse et al. (2004) indicate that maximum values of channel width tend to be close to bend

apexes and minimum width values tend to be near inflections. Within a subset having significant width variations (type C of the Brice, 1975 classification), width tended to be 14 percent larger at apexes than at inflections.

The reach of the Pembina River in figure 3.2 is of particular interest, because the relevant parameters are used below in implementations of our model of. Here we study the entire reach shown in figure 3.2, along with the Manola subreach which has shown rapid migration in recent geomorphic time (Beck et al., 1983). Figures 3.5a and 3.5b show the correlations between b and c for the entire reach and the Manola subreach. Over the entire reach, the fractional variation in width is 0.03 as c increases from 0 to 0.35; in the Manola subreach it is 0.09.

The observations presented here for the Vermillion, Trinity and Pembina Rivers, combined with the earlier analyses of Lagasse et al. (2004) suggest the following. Meandering rivers may evolve so as to a) have little systematic width variation, b) show apexes that are slightly narrower than crossings, or c) show apexes that are slightly to significantly wider than crossings. Case c) appears to be most common in rivers that show significant rates of migration.

The above picture is supported by results on the Lower Trinity River, TX, reported by Peyret (2011) and Smith (2012). The Trinity River reach shown in figure 3.1 is part of the Lower Trinity River, TX and is sandwiched between two low migration reaches: an upstream incising reach influenced by the presence of the Livingston Dam and a downstream backwater reach that feeds into the Trinity Bay. Peyret (2011) has shown that width is weakly and negatively correlated with centerline curvature in zones of low migration rate, whereas it is more strongly and positively correlated to curvature in zones where the river shows higher migration rates.

Plots of the type of figures 3.4 and 3.5 do not give a complete picture of width variation, because they do not specify the locations of minimum and maximum width relative to bend apexes. We address this with planform data from reaches of two rivers in Florida, USA; the Apalachicola and Suwannee Rivers. These rivers have dense bank vegetation, which makes quantification of width variation straightforward. The segment of the Suwannee River shown in figure 3.6 starts just north of Wannee in Gilchrist County, Florida, and ends at Fowler Bluff in Levee County, Florida. The segment of the Apalachicola River extends from New Hope, south of the Blountstown Gage, to the intersection between the Gulf County border to the north and the Liberty County border to the west¹.

An analysis of 33 bends of the Suwannee River indicates that the point of maximum width is located upstream of the bend apex, i.e. between the apex and the nearest crossing upstream, in 61 percent of cases; in the other cases, maximum width was located between the apex and the next crossing downstream. A corresponding analysis of the Apalachicola River showed that the point of maximum width is reached upstream of the apex in 75 percent of 44 bends. Evidently, these rivers have a strong bias in maximum width occurring between the apex and the nearest crossing upstream.

That this behavior is not universal is illustrated in figure 3.7. The Pembina River is similar to the Apalachicola and Suwannee Rivers, with width maximums preferentially located upstream of bend apexes. In the case of the Vermillion, the position of width maximum is equally split

¹ Analysis of the Suwannee River and the Apalachicola River was done by Sun Tao, a co-author of this manuscript

between upstream and downstream, and in the case of the Trinity River, width maximum is located preferentially downstream of bend apex.

Also shown in figure 3.7 is the percentage of bends for which the width minimum is located upstream of the bend apex. It is seen that in all cases but the Vermillion River, the point of width minimum tends to be located downstream of the bend apex. In the case of the Vermillion River, there is an equal likelihood for the width minimum to be located upstream or downstream of the apex.

Whether or not a migrating, meandering river shows correlation between the spatial variations of width and curvature, where maximum width is attained relative to bend apex, are determined by the internal dynamics of river itself. This dynamical picture cannot be understood without a model for width evolution itself. Such a model is the goal of the analysis below.

3.3 Width of an equivalent straight channel: bankfull geometry

Before exploring how meander planform and width variation co-evolve, it is necessary to specify a closure model for width that is applicable to an equivalent straight channel. More generally, we pursue a model for bankfull channel geometry. We consider a channel with characteristic bed material size \tilde{D}_s , and for which the dominant model of bed material transport is bedload. Let \tilde{Q}_o and \tilde{Q}_{so} be the bankfull water discharge and volume bedload transport rate per unit width at bankfull flow, respectively, and S_o denote the reach-averaged bed slope of a meandering reach. The bankfull half-width and bankfull depth of an equivalent straight reach at this slope are \tilde{b}_o and \tilde{H}_o . Bankfull flow velocity \tilde{U}_o is given according to the continuity relation

$$\tilde{Q}_o = 2\tilde{b}_o\tilde{H}_o\tilde{U}_o \quad (3.3)$$

In addition, \tilde{Q}_{so} is related to the volume bedload transport rate per unit width \tilde{q}_{so} according to the continuity relation

$$\tilde{Q}_{so} = 2\tilde{b}_o\tilde{q}_{so} \quad (3.4)$$

Bankfull streamwise bed shear stress $\tilde{\tau}_{sf}$ is related to bankfull flow velocity \tilde{U}_o as

$$\tilde{\tau}_{sf} = \dots C_f \tilde{U}_o^2 \quad (3.5)$$

where C_f is a dimensionless bed friction coefficient and \dots is (dimensioned) water density. The dimensionless parameter corresponding to channel-forming (i.e. bankfull) Shields number \dagger_{form}^* can be defined as

$$\dagger_{form}^* = \frac{\tilde{\tau}_{sf}}{\dots Rg\tilde{D}_s} \quad (3.6)$$

where R is the (dimensionless) submerged specific gravity of the sediment (1.65 for quartz) and g is (dimensioned) gravitational acceleration.

As outlined in Eke et al. (submitted), the constraints of a) normal flow momentum balance, b) a bedload transport relation, c) a specified channel-formative (bankfull) Shields number \dagger_{form}^* and d) specified grain size \tilde{D}_s result in three constraints on the five parameters \tilde{Q}_o , \tilde{Q}_{so} , \tilde{b}_o , \tilde{H}_o and S_o . Normal flow momentum balance takes the form

$$\ddagger_{sbf} = \dots g \tilde{H}_o S_o \quad (3.7)$$

where g denotes the (dimensioned) acceleration of gravity. Here we use the Parker (1979) approximation of the Einstein (1950) relation for bedload transport applied to bankfull flow:

$$\tilde{q}_{so} = 11.2 \sqrt{Rg\tilde{D}_s} \tilde{D}_s (\ddagger_{form}^*)^{1.5} \left[1 - \frac{\ddagger_c^*}{\ddagger_{form}^*} \right]^{4.5} \quad (3.8)$$

where \ddagger_c^* takes the value 0.03. Reduction of the above relations yields the three constraints:

$$S_o = \frac{R}{11.2 C_f^{1/2} \left[1 - \frac{\ddagger_c^*}{\ddagger_{form}^*} \right]^{4.5}} \left(\frac{\tilde{Q}_{so}}{\tilde{Q}_0} \right) \quad (3.9)$$

$$2\tilde{b}_0 = \frac{\tilde{Q}_{s0}}{11.2 (\ddagger_{form}^*)^{1.5} \left[1 - \frac{\ddagger_c^*}{\ddagger_{form}^*} \right]^{4.5} \sqrt{Rg\tilde{D}_s} \tilde{D}_s} \quad (3.10)$$

$$\tilde{H}_o = 11.2 \ddagger_{form}^* \left[1 - \frac{\ddagger_c^*}{\ddagger_{form}^*} \right]^{4.5} C_f^{1/2} \tilde{D}_s \left(\frac{\tilde{Q}_o}{\tilde{Q}_{so}} \right) \quad (3.11)$$

For example, if bankfull discharge, bedload transport rate at bankfull flow, grain size \tilde{D}_s and channel-forming Shields number are specified, the slope, width and depth of the channel can be computed from equations (3.9)~(3.11).

In the context of the present model, the specified parameters are bankfull discharge \tilde{Q}_o , grain size \tilde{D}_s and reach-averaged bed slope S_o corresponding to a sinuous channel at a given time. In earlier implementations of the above formulation (as summarized in Li et al., submitted and in Appendix B), \dagger_{form}^* was taken to be a specified parameter, taking one value for sand-bed rivers and another value for gravel-bed rivers. This assumption imposes an unrealistic constraint on meandering rivers.

MacDonald et al. (1991) provide a compendium of data for 16 reaches of migrating, meandering rivers in Minnesota, USA. The sinuosity of these reaches varies from 1.21 to 2.61. Now consider a river reach that is initially nearly straight with bed slope S_{oi} , but that evolves toward a tortuous state over time. According to equations (3.9) and (3.10) and the constraints of constant C_f and \dagger_{form}^* , as S_o drops from the straight-channel value S_{oi} to one corresponding to a sinuosity of 2.5, i.e. $0.4 S_{oi}$, width should correspondingly drop to 40 percent of its value at the nearly straight state. No such sharp drop in width with increasing sinuosity is observed in general, and in particular in the data set of MacDonald et al. (1991).

The resolution to this conundrum is contained in Li et al. (submitted). They use empirical data to demonstrate the following relation for channel-forming (bankfull) Shields number, across the range from silt-bed to cobble-bed rivers:

$$\dagger_{form}^* = 1220(D^*)^{-1} S^{0.53} \quad (3.12)$$

where D^* is a dimensionless grain size defined as

$$D^* = \frac{(Rg)^{1/3}}{\epsilon^{2/3}} D_s \quad (3.13)$$

and ϵ denotes (dimensioned) kinematic viscosity of water. According to (3.12), as the sinuosity of a reach increases, and thus the reach-averaged bed slope S_o drops, \dagger_{form}^* drops accordingly. This effect, when embedded in (3.9) and (3.10), results in modest, rather than extreme, channel narrowing as sinuosity increases, as illustrated subsequently in this paper.

The formulation for width-planform co-evolution pursued herein is based on deviation from the channel-forming Shields number. The flow under consideration is bankfull, but bed shear stress now varies spatially because of a meandering planform. The flow field, including bed shear stress, is computed in a submodel for in-channel morphodynamics. Adjacent to a bank, the streamwise bed shear stress may be above or below the value corresponding to channel-forming flow. In the former case, the bank is eroded according to a submodel capturing sediment removal mitigated by armoring due to slump blocks. In the latter case, the bank accretes according to a submodel capturing vegetal encroachment mitigated by increasing strength of near-bank flow.

3.4 Model formulation for a meandering channel

Our model formulation follows the framework of Parker et al. (2011). We define three distinct regions as shown in figure 3.8: a central channel of width $2\tilde{b}(\tilde{s})$ and two bank regions, where $\tilde{b}(\tilde{s})$ is the local channel half-width and \tilde{s} denotes a streamwise centerline coordinate (the tildes denote dimensioned parameters). Within the central region, a steady-state nonlinear flow and bed morphodynamics model is applied to determine in-channel characteristics. The bank region

characteristics (e.g. bank height and bank slope) are specified input parameters, and bank migration is modeled via shock conditions that determine the migration rate of the bank toe.

The model uses an assumption that is akin to the standard quasi-steady assumption of river bed morphodynamics (de Vries, 1965). It is assumed that the planform processes associated with bankline migration are sufficiently slow compared to both hydraulic and in-channel bed morphodynamic processes that at the time scale of planform evolution, the flow and bed can be approximated as steady state. This assumption, which is commonly used in other models of meander planform evolution as well (e.g. Frascati and Lanzoni, 2009) significantly reduces computation time, and allows for the model to be run at larger spatial and temporal scales. The drawback of this assumption is that the model cannot incorporate the formation of free bars migrating through a train of bends.

3.4.1. In-channel morphodynamic submodel for channel of varying width

As shown in figure 3.8, the model uses an intrinsic curvilinear coordinate system to describe the channel planform. In this coordinate system, the streamwise coordinate \tilde{s} corresponds to the channel centerline and the local transverse coordinate \tilde{n} is defined to be orthogonal to the channel centerline, and is always taken as increasing toward the left bank of the river looking downstream. This transverse coordinate varies from $-\tilde{b}(\tilde{s})$ to $\tilde{b}(\tilde{s})$ as shown in figure 3.8b.

The equations governing channel hydrodynamics/morphodynamics are presented below. Unless otherwise specified, dimensioned parameters introduced below are denoted so with a tilde superscript; the corresponding parameters without a tilde are dimensionless. Relevant scales for the non-dimensionalization are the previously-introduced dimensioned depth-averaged

streamwise flow velocity \tilde{U}_o , flow depth \tilde{H}_o and mean channel half-width \tilde{b}_o , all in a reference straight channel as defined in figure 3.8(c). The Froude number F_o and ratio of half-width to depth χ_o of the base flow are given as

$$F_o = \frac{\tilde{U}_o}{\sqrt{g\tilde{H}_o}}; \quad \chi_o = \frac{\tilde{b}_o}{\tilde{H}_o} \quad (3.14)$$

We introduce the following dimensionless parameters: s and n denote dimensionless streamwise and transverse coordinates, respectively, U and V denote dimensionless, depth-averaged streamwise and transverse flow velocities, respectively, H denotes dimensionless depth, c denotes dimensionless channel centerline curvature and \langle denotes dimensionless water surface elevation, defined as

$$s = \frac{\tilde{s}}{\tilde{b}_o}; \quad n = \frac{\tilde{n}}{\tilde{b}}; \quad b = \frac{\tilde{b}}{\tilde{b}_o}; \quad (U, V) = \frac{(\tilde{U}, \tilde{V})}{\tilde{U}_o}; \quad (H, \langle) = \frac{(\tilde{H}, \tilde{\langle})}{\tilde{H}_o}; \quad c = \frac{\tilde{b}_o}{\tilde{R}_c} \quad (3.15)$$

where \tilde{R}_c is the local centerline radius of curvature. Note here that the transverse coordinate n defined above has been rescaled with the local channel width $\tilde{b}(s)$ for geometric simplicity so that the dimensionless coordinate n always ranges from -1 to 1. The parameters (\ddagger_s, \ddagger_n) denote dimensionless streamwise and transverse bed shear stresses, respectively, and (q_s, q_n) denote dimensionless streamwise and transverse volume sediment transport rates per unit width, respectively: they are defined in terms of their corresponding dimensioned variables as

$$(\ddagger_s, \ddagger_n) = \frac{(\ddagger_s, \ddagger_n)}{\dots \tilde{U}_o^2}; \quad (q_s, q_n) = \frac{(\tilde{q}_s, \tilde{q}_n)}{\sqrt{Rg\tilde{D}_s\tilde{D}_s}} \quad (3.16)$$

The dimensionless steady-state depth-averaged equations of motion for a general fluid flow with variable width can thus be written in intrinsic curvilinear coordinates as follows:

$$\frac{\partial HV}{\partial n} + NbcVH + bL_{sn}(UH) = 0 \quad (3.17)$$

$$V \frac{\partial U}{\partial n} + UbL_{sn}(U) + bNcU(V + 2\zeta) + \frac{1}{H} \frac{\partial HU\zeta}{\partial n} = -\frac{1}{F_o^2} bL_{sn}(\zeta) - b \frac{\kappa_o \ddagger_s}{H} \quad (3.18)$$

$$\begin{aligned} V \frac{\partial V}{\partial n} + UbL_{sn}(V) + Nbc(2V\zeta + \mathfrak{E} - U^2) + 2 \frac{1}{H} \frac{\partial HV\zeta}{\partial n} + \frac{1}{H} \frac{\partial H\mathfrak{E}}{\partial n} \\ + \frac{1}{H} bL_{sn}(UH\zeta) = -F_o^{-2} \frac{\partial \zeta}{\partial n} - b \frac{\kappa_o \ddagger_n}{H} \end{aligned} \quad (3.19)$$

where L_{sn} is a differential operator given as

$$L_{sn} = N \left(\frac{\partial}{\partial s} - \frac{n}{b} \frac{db}{ds} \frac{\partial}{\partial n} \right) \quad (3.20)$$

N is the longitudinal metric coefficient of the coordinate system, i.e.

$$N = (1 + nbc)^{-1} \quad (3.21)$$

and the parameters ζ and \mathfrak{E} in (3.18) and (3.19) are secondary flow redistribution terms defined in Eke et al. (submitted, Chapter 2).

The Exner equation of bed sediment conservation is given as:

$$bL_{sn}(q_s) + \frac{\partial q_n}{\partial n} + q_n Nbc = 0 \quad (3.22)$$

Closures for the components of bed shear stress and bedload transport are as given in Eke et al. (submitted, Chapter 2), i.e.

$$(\dagger_s, \dagger_n) = C_f \sqrt{U^2 + V^2} \left(U, V + \frac{\epsilon_s(0)}{T(0)} \right) \quad (3.23)$$

$$(q_s, q_n) = \Phi (\cos [\alpha], \sin [\alpha]) \cong \Phi \left(1, \frac{\dagger_n^*}{\dagger_s^*} - \frac{r}{\chi_o \sqrt{\dagger_o^*}} \frac{\partial y}{\partial n} \right) \quad (3.24)$$

where v_s denotes dimensionless secondary flow (made dimensionless by the streamwise velocity \tilde{U}_o), C_f is the bed friction coefficient (here assumed to be a constant), T is a primary flow structure function (Johannesson and Parker, 1989), $[\alpha]$ indicates the angle of direction of sediment transport relative to the channel centerline, r is a coefficient ranging from 0.3 to 1 (see also Johannesson and Parker, 1989). \dagger_s^* and \dagger_n^* are the dimensionless Shields stresses given as:

$$(\dagger_s^*, \dagger_n^*) = \frac{\tilde{U}_o^2}{gR\tilde{D}_s} (\dagger_s, \dagger_n) \quad (3.25)$$

and Φ is the bedload transport intensity, here estimated using the relation of Parker (1979):

$$\Phi = 11.2 (\dagger_s^*)^{1.5} \left[1 - \frac{0.03}{\dagger_s^*} \right]^{4.5} \quad (3.26)$$

The approximation for secondary flow adopted here is derived from the case of steady, uniform bend flow; and has been generalized to a channel of arbitrary curvature:

$$\epsilon_s = \frac{UH}{\tau_1 \kappa_o C_f} cG \quad (3.27)$$

where G is the normalized secondary flow structure function defined in Johannesson and Parker (1989) and $\tau_1 = C_f^{-1/2} / 13$

The lateral boundary conditions associated with equations (3.17)-(3.19) and (3.22) are no-penetration conditions for the flow and sediment transport respectively. Thus, $\mathbf{U} \cdot \hat{\mathbf{n}}_b = \mathbf{q} \cdot \hat{\mathbf{n}}_b = 0$, where \mathbf{U} and \mathbf{q} are the velocity and bedload transport vectors respectively and $\hat{\mathbf{n}}_b$ is the unit vector normal to the banks. This translates to:

$$-\frac{U}{(1 \pm bC)} \frac{db}{ds} \pm V = 0 \quad \text{at } n = \pm 1 \quad (3.28)$$

$$-\frac{q_s}{(1 \pm bC)} \frac{db}{ds} \pm q_n = 0 \quad \text{at } n = \pm 1 \quad (3.29)$$

In the streamwise direction, for simplification, periodic boundary conditions are applied.

Finally, the imposed integral conditions for the conservation of water and sediment discharge within the channel are as follows:

$$b \int_{-1}^1 UH dn = 2 \quad (3.30)$$

$$b \int_{-1}^1 q_s dn = 2q_{so} \quad (3.31)$$

where q_{so} is the streamwise bedload transport rate for the reference straight channel. The integral conditions (3.30) and (3.31) specify that the water discharge and sediment discharge in the channel respectively remain the same as for a reference straight channel, regardless of sinuosity. As a result, the average channel slope S becomes a free variable represented by the deviation s_{do} from the reference channel slope S_o , such that

$$S = S_o (1 + s_{do}) \quad (3.32)$$

Nonlinear effects assure that in the case of a bend with the same average width, the same sediment transport rate is realized at a *lower* average bed slope than the case of a straight channel (e.g. Luchi et al., 2012). In keeping with (3.32), *constant* deviatoric velocity and depth parameters, u_{do} and h_{do} respectively, arise which in the presence of sinuosity allow total reach-averaged velocity and flow depth to differ from the values corresponding to the reference straight channel. Thus

$$\tilde{H}_{mean} = \tilde{H}_o (1 + h_{do}); \quad \tilde{U}_{mean} = \tilde{U}_o (1 + u_{do}) \quad (3.33)$$

At the linear level however, the reach-averaged values of velocity, bed slope and depth are found to be identical to the reference values (e.g. Imran et al., 1999).

The method to arrive at an iterative solution of the nonlinear system of equations is as outlined in Imran et al. (1999) and Camporeale et al. (2007). Herein we go a step further to include the added complexity of width variation to the solution outlined in Camporeale et al. (2007). Our method involves expressing each morphodynamic variable as the sum of a uniform flow (reach averaged) solution and a deviation due to the combined effect of channel curvature and width variation. Thus, local variables are expressed as follows:

$$(U, V, H, \zeta, y, c, b) = \left[1 + u_{do}, 0, 1 + h_{do}, \zeta_r + (1 + h_{do}) - S_o (1 + s_{do}) s, y_r - S_o (1 + s_{do}) s, 0, 1 \right] + (u_d, v_d, h_d, \zeta_d, y_d, c, b_d) \quad (3.34)$$

where $h_d = \zeta_d - y_d$, the subscript “d” denotes the deviation and ζ_r, y_r are the reference water and bed elevation as shown in figure 3.8(c). In the above equations, u_{do}, s_{do} and h_{do} denote the constant deviatoric streamwise velocity, slope and water depth respectively, which correspond to reach-averaged conditions and are independent of s and n .

Meanwhile, q_s is taken to be a nonlinear function of U such that $q_s = 1$ where $U = 1$. As defined in equations (3.24) and (3.26), q_s is evaluated from the relation of Parker (1979) and can be expressed in the form of a Taylor’s expansion, i.e.

$$q_s = 11.2 (\dagger_s^*)^{1.5} \left[1 - \frac{0.03}{\dagger_s^*} \right]^{4.5} = q_{so} (1 + M(U - 1) + R_q(U)) \quad (3.35)$$

where $M = 2 \frac{\dagger_o^*}{q_{so}} \frac{\partial q_s}{\partial \dagger_s^*} \Big|_{\dagger_s = \dagger_o}$. The above equation illustrates the approach to the nonlinear problem presented here; R_q represents the difference between the full sediment transport relation and its linear form, or thus the nonlinear residual.

The deviations u_d, ζ_d and y_d can be further decomposed as follows:

$$\begin{aligned} u_d &= u_{dd}(s, n) + u_{dc}(s) \\ y_d &= y_{dd}(s, n) + y_{dc}(s) \\ \zeta_d &= \zeta_{dd}(s, n) + \zeta_{dc}(s) \end{aligned} \quad (3.36)$$

Here u_{dc} , ζ_{dc} and y_{dc} denote the cross-sectionally averaged deviations of streamwise velocity u_d , water surface elevation ζ_d , and bed elevation y_d , respectively. As such, they are functions of streamwise coordinate s only. In addition, the parameters u_{dd} , ζ_{dd} and y_{dd} represent the corresponding differences $u_d - u_{dc}$, $\zeta_d - \zeta_{dc}$ and $y_d - y_{dc}$; they depend on s and n , and characterize the transverse variations of streamwise velocity, water surface elevation and bed elevation. By definition, the parameters u_{dd} , ζ_{dd} and y_{dd} must satisfy the conditions

$$\int_{-1}^1 u_{dd} dn = 0 \quad \int_{-1}^1 \zeta_{dd} dn = 0 \quad \int_{-1}^1 y_{dd} dn = 0 \quad (3.37)$$

In addition, u_{dc} , ζ_{dc} , and y_{dc} are assumed to be periodic with wavelength λ and must satisfy the following condition:

$$\int_0^\lambda u_{dc} ds = 0 \quad \int_0^\lambda y_{dc} ds = 0 \quad \int_0^\lambda \zeta_{dc} ds = 0 \quad (3.38)$$

At this point, it is seen that ten unknowns, u_{do} , S_{do} , h_{do} , u_{dc} , ζ_{dc} , y_{dc} , u_{dd} , ζ_{dd} , y_{dd} and v_d appear in the above equations. According to these variables, three types of problems are defined: the ‘‘O’’ problem with unknowns u_{do} , S_{do} , and h_{do} independent of s and n ; the ‘‘C’’ problem with unknowns u_{dc} , ζ_{dc} , and y_{dc} which are function of s only; and the ‘‘D’’ problem with unknowns u_{dd} , ζ_{dd} , y_{dd} and v_d which are functions of s and n .

Substituting the above decomposition into the governing equations and applying the relevant closures, boundary and integral conditions, the solution of the governing equations are as expressed below and in order of iteration

O-SOLUTIONS

$$u_{do}^{\epsilon+1} = -\frac{1}{M} \frac{1}{\int_0^L b_d ds} + R_{61}^v \quad (3.39)$$

$$h_{do}^{\epsilon+1} = -\frac{(M-1)}{M} \frac{1}{\int_0^L b_d ds} + R_{51}^v - R_{61}^v \quad (3.40)$$

$$s_{do}^{\epsilon+1} = -\left(\frac{3-M}{M}\right) \frac{1}{L} \int_0^L b_d ds - R_{51}^v + 3R_{61}^v - R_{22}^v \quad (3.41)$$

C-SOLUTIONS

$$y_{dc}^{v+1} = \langle_{dc}^{v+1} + \left(\frac{M-1}{M}\right) \left(b_d - \frac{1}{\int_0^L b_d ds}\right) + R_{62}^v - R_{52}^v \quad (3.42)$$

$$u_{dc}^{\epsilon+1} = -\frac{1}{M} \left(b_d - \frac{1}{\int_0^L b_d ds}\right) + R_{62}^v \quad (3.43)$$

$$\langle_{dc}^{\epsilon+1} = \langle_{dc}^{\epsilon+1}(0) + F_o^2 \int_0^s \left[\begin{array}{l} \frac{1}{M} \frac{\partial b_d}{\partial s} - v \left(\frac{1+M}{M}\right) \left(b_d - \frac{1}{\int_0^L b_d ds}\right) \\ -v(3R_{62}^v + R_{52}^v) + R_{24}^v - \frac{\partial R_{62}^v}{\partial s} \end{array} \right] ds' \quad (3.44)$$

D-SOLUTIONS

$$u_{dd}^{\epsilon+1} = u_{dd}^{\epsilon+1}(0, n) e^{-2vs} + e^{-2vs} \int_0^s e^{2vs} \left[v \langle_{dd}^{\epsilon} - v y_{dd}^v - F_o^{-2} \frac{\partial \langle_{dd}^{\epsilon}}{\partial s} - v n c + R_{23}^v \right] ds' \quad (3.45)$$

$$\langle_{dd}^{v+1} = F_o^2 cn + F_o^2 \int_{-1}^n R_3^\epsilon dn' - F_o^2 \frac{1}{2} \int_{-1}^1 \int_{-1}^n R_3^\epsilon dn' dn'' \quad (3.46)$$

$$v_d^{\epsilon+1} = -\frac{\partial b_d}{\partial s} - (n+1) \left(\frac{\partial u_{dc}^{\epsilon+1}}{\partial s} + \frac{\partial \langle_{dc}^{\epsilon+1}}{\partial s} - \frac{\partial y_{dc}^{\epsilon+1}}{\partial s} \right) \quad (3.47)$$

$$- \frac{\partial}{\partial s} \int_{-1}^n (u_{dd}^{\epsilon+1} + \langle_{dd}^{\epsilon+1} - y_{dd}^{v+1}) dn + R_1^\epsilon$$

$$y_{dd}^{\epsilon+1} = \frac{\chi_o \sqrt{\dagger_{so}^*}}{r} \left[\left(\frac{\partial b_d}{\partial s} + \frac{G(0)}{tv} c \right) n + \int_{-1}^n \Lambda^{\epsilon+1} dn' - \right. \quad (3.48)$$

$$\left. \frac{1}{2} \int_{-1}^1 \int_{-1}^n \Lambda^{\epsilon+1} dn' dn'' + \int_{-1}^n R_4^\epsilon dn' - \frac{1}{2} \int_{-1}^1 \int_{-1}^n R_4^\epsilon dn' dn'' \right]$$

where the terms R_1 to R_{62} in the above equations are nonlinear residuals. These, along with the solution procedure, are presented in Appendix A. The solution is obtained iteratively starting with a linear solution obtained by setting all nonlinear residuals to zero.

3.4.2. Bank Submodels

As previously stated, in order to generate width oscillations by channel migration, the standard channel centerline migration model proposed by Hasegawa (1977) and Ikeda et al. (1981) must be abandoned in favor of a model that allows each bank to migrate independently. The bank migration model formation proposed in Parker et al. (2011) and modified in Eke et al. (submitted) quantifies this migration rate through a shock condition, which can be applied to either an eroding or depositing bank. Only a summary is given here; details can be found in the preceding references.

The shock condition is based on the assumption of a specific bank structure. Here the index j denotes either the left bank (LB) or right bank (RB). Let $\dot{\tilde{n}}_j$ denote the (dimensioned) normal migration rate of the j bank. The bank is assumed to consist of a non-cohesive layer of sediment of thickness $\tilde{H}_{b,j}$, topped by a cohesive layer which, when eroded, generates slump blocks. The magnitude of the slope of the bank region is denoted as $S_{s,j}$, the transverse position of the toe of the bank is $\tilde{n}_{t,j}$, the transverse position of the center of the bank region is $\bar{\tilde{n}}_j$ and the porosity of the non-cohesive bank material is $p_{b,j}$. Finally, $\tilde{q}_{nb,j} = \tilde{q}_n|_{\tilde{n}=\tilde{n}_{t,j}}$ denotes the transverse bedload transport rate at the toe of the bank. The shock condition is then given as

$$\begin{aligned}\dot{\tilde{n}}_j &= \frac{-\tilde{q}_{fb,j} (1 + \tilde{n}_{t,j} \tilde{C})}{\tilde{H}_{b,j} (1 + \bar{\tilde{n}}_j \tilde{C}) (1 - p_{b,j})} + \frac{1}{S_{s,j}} \frac{\partial \tilde{y}_j}{\partial \tilde{t}} \Big|_{\tilde{n}=\tilde{n}_{t,j}} \\ &= \tau_{E/D}^{\sim} + \frac{1}{S_{s,j}} \frac{\partial \tilde{y}_j}{\partial \tilde{t}} \Big|_{\tilde{n}=\tilde{n}_{t,j}}\end{aligned}\quad (3.49)$$

where \tilde{y} is bed elevation and $\tilde{y}_j = \tilde{y}|_{\tilde{n}=\tilde{n}_{t,j}}$. As in the flow model, the transverse coordinate \tilde{n} is defined as increasing towards the left bank looking downstream, so that at the toe of the left bank $\tilde{n} = \tilde{n}_{t,LB} = \tilde{b}(\tilde{t})$, and at the toe of the right bank $\tilde{n} = \tilde{n}_{t,RB} = -\tilde{b}(\tilde{t})$, where \tilde{b} is the half channel width.

As shown in Eke et al. (submitted, Chapter 2), quantification of the first term on the right-hand side of (3.49), i.e. the term $\tau_{E/D}^{\sim}$, must be done differently depending on whether the bank is eroding or depositing. The discrimination between the two is made in terms of an empirical relation

for channel-forming (bankfull) Shields number \dagger_{form}^* , i.e. equation (3.12). Here we assume that if the Shields number based on the streamwise bed shear stress immediately adjacent to a bank \dagger_j^* is greater than a reach-averaged channel-formative value \dagger_{form}^* , the bank erodes; otherwise it deposits.

For an eroding bank, i.e. one for which $\dagger_j^* \equiv \dagger_E^* > \dagger_{form}^*$ the model specifies the bank migration rate i'_E (away from the channel centerline) in terms of a default transverse removal rate by bedload transport based on the assumption of purely non-cohesive, loose bank sediment, but with this default removal rate damped by natural armoring due to slump blocks. Thus,

$$i'_E = K_{armor} I_f i'_{non,E} \quad (3.50)$$

where $i'_{non,E}$ is the erosional bank migration rate for a purely non-cohesive bank and I_f is a flood intermittency factor corresponding to an estimate of the fraction of time that the river is morphodynamically active. The parameter $i'_{non,E}$ is specified in Eke et al. (submitted) as

$$i'_{non,E} = - \frac{1}{(1 - p_{b,E})} \frac{\tilde{q}_{non,E}}{\tilde{H}_{b,E}} \frac{(1 + \tilde{n}_{t,E} \tilde{C})}{(1 + \bar{n}_E \tilde{C})} \quad (3.51)$$

where $\tilde{q}_{non,E}$ is the transverse bedload transport rate along a sloping bank estimated for a purely non-cohesive bank, $p_{b,E}$ is the porosity of the non-cohesive portion of the eroding bank and $\tilde{H}_{b,E}$ denotes the non-cohesive layer thickness $H_{b,j}$ where the bank j is eroding.

$K_{armor} \leq 1$ is a multiplicative armoring coefficient modeled as a function of slump block characteristics, given as:

$$K_{armor} = \frac{1}{\left(1 + \left(\frac{\dagger_E^*}{\dagger_{form}^*} - 1\right)^{-1} I_{f,ref} \frac{\left| \tilde{i}_{non,E} \right|}{\tilde{i}_{Eref}} \right)} \quad (3.52)$$

In (3.52), the parameter $I_{f,ref}$ is a reference intermittency, and \tilde{i}_{Eref} is a lumped reference erosion rate corresponding to that intermittency, which is in turn a function of slump block properties. According to Eke et al. (submitted), this relation takes the form.

$$\tilde{i}_{Eref} = \frac{\tilde{D}_c \tilde{B}_{bw}}{\tilde{H}_c (1 - p_c) \tilde{T}_{cref}} \quad (3.53)$$

where \tilde{D}_c is a characteristic size of the slump blocks, \tilde{H}_c is the thickness of the cut-bank cohesive layer, p_c denotes the porosity of the cohesive material, \tilde{T}_{cref} denotes a characteristic reference slump block residence time and

$$\tilde{B}_{bw} = \tilde{H}_{b,E} \sqrt{1 + (S_{s,E})^2} \quad (3.54)$$

is the arc width of the zone available to be covered by slump blocks and $S_{s,E}$ denotes the parameter $S_{s,j}$ for an eroding bank.

Note that the intermittency I_f in (3.50) need not be identical to the reference value $I_{f,ref}$ in (3.52) (which corresponds to the intermittency at which \tilde{T}_{cref} was determined). This generalization

makes it possible to freely vary I_f , so allowing the treatment of arbitrary flood regime (as quantified in terms of flood intermittency).

For a depositing bank, i.e. one for which $\dagger_j^* \equiv \dagger_D^* M \dagger_{form}^*$, the model specifies a default rate of transverse migration i_{veg}^{\sim} of the inner accretional bank toward the channel center associated with flows that are insufficient to suppress vegetation growth, i.e. during the fraction of time $1 - I_f$. The model then assumes a linear suppression of this encroachment rate as the near-bank bed shear stress increases according to the relation, so that where i_D^{\sim} denotes the depositional migration rate,

$$i_D^{\sim} = i_{veg}^{\sim} (1 - I_f) \left(1 - \frac{\dagger_D^*}{\dagger_{form}^*} \right) \quad (3.55)$$

where i_D^{\sim} is a rate of transverse migration of the inner accretionary bank toward the channel center and \dagger_D^* is the Shields number based on the streamwise shear stress acting on the bed immediately adjacent to the depositing bank.

To summarize, then, for any bank j , the lateral migration rate is computed as:

$$\dot{\tilde{n}}_j = \begin{cases} i_E^{\sim} + \frac{1}{S_{s,j}} \frac{\partial \tilde{y}_j}{\partial \tilde{t}} \Big|_{\tilde{n}=\tilde{n}_{i,j}} & \dagger_j^* > \dagger_{form}^* \\ i_D^{\sim} + \frac{1}{S_{s,j}} \frac{\partial \tilde{y}_j}{\partial \tilde{t}} \Big|_{\tilde{n}=\tilde{n}_{i,j}} & \dagger_j^* \leq \dagger_{form}^* \end{cases} \quad (3.56)$$

where relations for \tilde{r}_E and \tilde{r}_D are specified by (3.50) and (3.55) respectively. Model bank input parameters thus include a specification of a relation for the formative Shields number \dagger_{form}^* , an estimation of the lumped reference migration rate due to erosion \tilde{r}_{Eref} and an estimation of the default vegetal encroachment rate \tilde{r}_{veg} .

3.4.3. Kinematic model for channel shift

The channel axis is discretized through a sequence of equally spaced nodes (x_c, y_c) , each of representing a cross-section of the river identified by the streamwise coordinate \tilde{s} . The spatial distribution of the angle $\theta(\tilde{s})$, formed by the local tangent to the channel axis and the direction of a generic Cartesian axis of reference, is obtained by the following relationship:

$$\theta^{(i)} = \arctan\left(\frac{y_c^{(i+1)} - y_c^{(i-1)}}{x_c^{(i+1)} - x_c^{(i-1)}}\right) \quad (3.57)$$

where the subscript i denotes the location along the streamwise co-ordinate. The curvature distribution can thus be computed easily as:

$$\tilde{c}(\tilde{s}) = -\frac{d\theta}{d\tilde{s}} \quad (3.58)$$

Central differences are used to calculate the derivative of θ and periodic boundary conditions are applied at the reach boundaries.

Planimetric evolution of the channel centerline is calculated by displacing each centerline node orthogonally by an amount

$$\Delta_c^{(i)} = \frac{1}{2} \left[\dot{\tilde{n}}_{LB}^{(i)} + \dot{\tilde{n}}_{RB}^{(i)} \right] \Delta \tilde{t} \quad (3.59)$$

such that the new centerline co-ordinates are

$$\begin{aligned} xc^{(i)}(t + \Delta t) &= xc^{(i)}(t) - \Delta_c^{(i)} \sin \theta^{(i)} \\ yc^{(i)}(t + \Delta t) &= yc^{(i)}(t) + \Delta_c^{(i)} \cos \theta^{(i)} \end{aligned} \quad (3.60)$$

The corresponding channel half-width evolution is computed accordingly:

$$\tilde{b}^{(i)}(t + \Delta t) = \tilde{b}^{(i)}(t) + \frac{1}{2} \left(\dot{\tilde{n}}_{LB}^{(i)} - \dot{\tilde{n}}_{RB}^{(i)} \right) \Delta \tilde{t} \quad (3.61)$$

At each time step, once the centerline has been displaced according to (59), the new centerline is re-gridded such that each node is equally spaced at an interval $\Delta \tilde{s}$ set on the order of the mean channel half-width $\tilde{b}_o(\tilde{t})$. Thus, as the channel migrates, to maintain the specified grid spacing, the number of nodes in the channel grid may increase or decrease. The channel half width distribution corresponding to the re-gridded centerline is obtained by cubic spline interpolation.

In so far as the mean width, length and reach-averaged slope of the channel is changing in time, the parameters \tilde{U}_o and \tilde{H}_o corresponding to the reference straight channel solution also evolve, according to the following relations obtained from equations (3.3), (3.5) and (3.7):

$$\tilde{H}_o = \left(\frac{C_f \tilde{Q}_o^2}{4 \tilde{b}_o^2 \tilde{g} S_o} \right)^{1/3} ; \quad \tilde{U}_o = \left(\frac{\tilde{g} \tilde{Q}_o S_o}{C_f 2 \tilde{b}_o} \right)^{1/3} \quad (3.62)$$

These parameters, which are embedded into the non-dimensionalization of equation (3.15), must be recomputed at every time step. The reference channel slope is varied under the constraint of a constant elevation drop $\Delta\tilde{z}$ as:

$$\mathfrak{S}(\tilde{t}) = \frac{\Delta\tilde{z}}{\tilde{L}} \quad (3.63)$$

where \tilde{L} is the channel centerline reach length.

The step size $\Delta\tilde{t}$ is controlled as suggested by Frascati and Lanzoni (2009) by requiring that

$$\Delta\tilde{t} \leq 0.01 \frac{\Delta\tilde{s}}{\left(\dot{\tilde{n}}_j\right)_{\max}} \quad (3.64)$$

The form of (3.64) is similar to the relation used by Courant et al. (1952) for the stability of explicit numerical schemes for computation of riverbed deformation. In this particular case, the celerity of propagation of an infinitesimal bed perturbation is replaced by the celerity of river migration.

3.5 Numerical Experiments

3.5.1. Set-up

Starting from a constant width, low-amplitude meander, we apply the above formulation to an initial sine-generated meander waveform, and run until incipient cut-off conditions. The sine-generated meander waveform is defined according to:

$$\theta = \theta_0 \sin(|s|) \quad (3.65)$$

where θ specifies the angle orientation of the s coordinate, θ_0 is the angular amplitude and k is the downstream channel wavenumber. Channel curvature distribution is thus evaluated as:

$$c = -\frac{d\theta(s)}{ds} = \theta_0 \cos(|s|) \quad (3.66)$$

The test-case river channel for the calculations is based on a reach of the Pembina River (section 3.2, figure 3.2) which represents a fairly typical actively meandering sand bed stream (Beck, 1983, Beck et al., 1988, Imran et al., 1999). According to Beck (1983), this reach has shown peak bank erosion rates ranging between 2 – 5 m/yr, an estimated bankfull discharge that range 250 – 440 m³/s, a mean bankfull width of 91 m, a mean bankfull depth of 3.75 m, a water surface slope of 0.00026 corresponding to a sinuosity of 1.9 and an estimated friction coefficient $C_f = 0.0068$.

A representative bankfull discharge of 405m³/s is chosen which has a flood intermittency of approximately 0.2 (Beck, 1983). Characteristic grain size \tilde{D}_s is known to be in the sand range for the reach in question; here it is set equal to 2.0 mm, i.e. the upper end of sand. This modification is made so that sediment transport can be computed solely from a bedload transport relation, here chosen to be Parker (1979). In the case of medium sand, the sediment transport rate would have to be decomposed into bedload and suspended load parts, and the gravitational term in equation (25) would have to be applied only to bedload transport.

In order to specify an appropriate initial state, the river bankfull parameters have been adjusted to correspond to a nearly straight channel with a water surface slope equal to the channel

downvalley slope S_v ($= 0.00026 \times 1.9 = 0.00049$). The formative Shields number is estimated using the linear regression fit of Li et al (submitted, Appendix B) which is as expressed in equation (3.12), and the corresponding bankfull channel characteristics are obtained from equations (3.9)-(3.11). Table 3.2 shows the adopted model input parameters corresponding to a nearly straight reach of the Pembina River. Comparing with the dataset of Parker et al (2007) and Wilkerson and Parker (2010) for river reaches covering a broad range of grain size classes, we see, as shown in figure 3.9, that the channel-forming Shields number \dagger_{form}^* corresponding to the model input parameters fits within the range for rivers of similar grain sizes. This value is used here as an initial value $\dagger_{form,i}^*$ corresponding to a nearly straight or low-sinuosity channel.

The estimated reference erosional migration rate $\tilde{i}_{Eref} = 5\text{m/yr}$ is based on the following assumptions: an average cut bank 3.75m high with a third of the bank height consisting of cohesive/rooted soil, a characteristic slump block size equal to the cohesive layer thickness, a reference slump block decay time \tilde{T}_{cref} of 1.5 years, and a cohesive layer porosity $p_c = 0.6$. A default vegetal encroachment rate \tilde{i}_{veg} corresponding to approx. 10% of initial bankfull width per year, or thus 10 m/yr has been adopted. Here these numbers have been chosen in part by means of numerical experiments, so as to produce results that correspond to observations. In principle, all these parameters are physically measurable; but measurement of \tilde{T}_{cref} and \tilde{i}_{veg} in particular would require an extensive field campaign that is beyond the scope of this work.

For the initial low-amplitude channel, we assume an along-channel centerline wavelength $\tilde{\lambda}$ of 2 km and an initial maximum curvature value $c_{apex} = \hat{c} = 0.025$.

The input parameters shown in table 3.2 are for the base run. In addition to the base case, numerical experiments were carried out to determine model sensitivity to selected non-dimensional parameters. The input parameters for the various runs expressed in terms of dimensionless numbers are shown in table 3.3.

Going from right to left, the dimensionless parameters shown in each column are: the half-width to depth ratio or aspect ratio χ_o , the dimensionless grain size D_s , the channel forming Shields number \dagger_{form}^* , the dimensionless channel wavenumber $|$ and the ratio of reference erosion rate to reference deposition rate, Υ . The first four parameters are considered to be key governing parameters in river morphodynamics. The last parameter, Υ , specifically defined as,

$$\Upsilon = \frac{\tilde{i}_{Eref}}{\tilde{i}_{veg}} \quad (3.67)$$

is here shown to be critical in determining the correlation between channel width and curvature. By varying discharge within the range of estimated bankfull discharge i.e. from 200 - 405 m³/s, we vary the initial value of the aspect ratio from 8.6 – 17.5 in the G runs. We vary both the grain size and formative Shields number in the D runs by increasing the grain size from coarse sand to medium gravel i.e. from 2 - 10mm. Finally, we vary the reference migration parameter in runs Y by fixing the reference erosion parameter $\tilde{i}_{Eref} = 5$ m/yr and varying the deposition parameter accordingly so that Υ varies from 0.25 to 1.5. As a check, the Y runs were repeated for different values of \tilde{i}_{Eref} .

3.5.2. Constant versus slope-dependent channel-forming Shields number

We indicated in Section 3 that the adoption of a constant value of channel-forming Shields number \dagger_{form}^* equal to the initial value $\dagger_{form,i}^*$ leads to a channel that becomes unacceptably narrow as sinuosity increases. Here we illustrate this process, and also illustrate how the slope-dependent form (3.12) for channel-forming Shields number resolves this problem.

The calculation is first performed for the base case values under the assumption of constant $\dagger_{form}^* = 0.426$ (Table 3.2). Figure 3.10(a) shows the planimetric evolution of the channel centerline over time in terms of five snapshots from time $t = 0$, each at 1000-year intervals, and figure 3.10(b) plots the two banklines over the same time interval. In figure 3.10(a) we see that the channel undergoes an initial rapid downstream and lateral channel migration rate which reduces as the sinuosity increases. The figure also shows the development of an upstream skewing bias as the channel elongates (e.g. Parker et al., 1983). The simulation does not reach incipient cut-off, as the numerical model fails not long after the last snapshot at $t = 3400$ years. Figure 3.10(b) and figure 3.12 illustrates the cause of failure.

The continuous variation of the downchannel slope triggered by planimetric evolution results in a variation of reach-averaged/reference channel characteristics. As shown in figure 3.10(b) and 3.11, with the increasing sinuosity, channel width and depth adjusts as expected. Mean bankfull width reduces and mean bankfull depth increases with the progressive decline in channel slope. The result is a channel that becomes progressively deeper and narrower as it approaches cut-off. This narrowing yields a width-depth ratio that is not only unrealistically small from a physical point of view, but also causes failure of the numerical model, as shown in figure 3.11.

Figures 3.12 and 3.13 show the corresponding calculations for the case of a slope-dependent channel-forming Shields number varying according to (3.12). Although channel narrowing is observed, the channel continues to develop sinuosity until incipient neck cutoff. This result highlights the significance of the work of Li et al. (submitted), who demonstrate that bankfull Shields number increase to about the half power of channel slope. The model results show that the inclusion of this effect is important in the analysis of meandering channels with self-formed width.

In all cases below, the channel-forming Shields number is assumed to be slope-dependent according to(3.12)

3.5.3. Base Case

The planimetric evolution of the base simulation is as shown in figure 3.12 and 3.13. In addition to a migration rate and a channel width that declines, it can be discerned that the channel develops and maintains a spatial width variation pattern which becomes less prominent over time as the channel elongates. The nature of this variation is illustrated more clearly below.

Let c_{apex} denote the dimensionless curvature at the bend apex, $\dot{\tilde{n}}_{max}$ denote the (dimensioned) magnitude of the maximum centerline lateral migration rate of the channel bend, and u denote the (dimensionless) strength of the width variation deviation, here defined as:

$$u = \frac{\tilde{B}_{max} - \tilde{B}_{min}}{4\tilde{b}_o} \quad (3.68)$$

where \tilde{B}_{\max} and \tilde{B}_{\min} are the maximum and minimum widths for the reach at a given time. Over the course of channel evolution, we observe, as shown in figure 3.14(a), that c_{apex} , u and $\dot{\tilde{n}}_{\max}$ rapidly increase, reach a peak value at 498, 450 and 425 years respectively and then decline more slowly. The peak values obtained for the migration rates and width variation are within the range of observed values for the reach of the Pembina River in question.

In figure 3.14(b), the loop curve mapping the computed relationship between maximum migration rate $\dot{\tilde{n}}_{\max}$ and dimensionless radius of curvature $1/c_{apex}$ up to incipient cutoff for the base case is shown. The peak migration rate shown on the loop falls toward the lower end of the observed range of peak values, i.e. 2 ~ 5 m/yr. reported by Beck (1983). Beck's values are for the relatively rapidly migrating Manola subreach rather than the entire reach of figure 3.2.

Also shown in figure 3.14(b) are data of Hickin and Nanson (1984) for the Beatton River, Canada. These are included only to illustrate a similar trend for sufficiently large radius of curvature; evidently the Beatton River has a peak migration rate that is substantially lower than the reach of the Pembina River studied here.

In figure 3.14(c), the computed loop curve in the form of $\dot{\tilde{n}}_{\max} / \tilde{b}_o$ versus $1/c_{apex}$ is plotted against data for the Beatton River, as well as 21 other river reaches in Canada, including the Pembina River. Also shown in figure 3.14(c) is an envelope curve bounding the data from above. Figures 3.14(b) and 3.14(c) suggest model performance that is in the expected range for meandering rivers. The model does not capture a zone within which migration rate decreases with increasing curvature (decreasing radius of curvature $1/c_{max}$). This may be due to a) limitations of

the model at high curvature, or b) behavior observed in the field associated with the development of bend complexity and cut-off (Hickin and Nanson, 1984; Hooke, 2003). The observed behavior at very high curvature is not captured in the simple implementation shown in figure 3.12, corresponding to a periodic bend developing only as far as cutoff, but can be partially captured in an implementation that includes non-periodicity and goes beyond cutoff. (Eke and Parker, Chapter 4).

Figure 3.15 shows the downstream variation in dimensionless curvature c , half width b and relative bed elevation y_d at channel right, left and center (i.e. $n = -1, 1$ and 0 respectively) for the time $t=500$ years. This time is when the bends reach peak curvature, i.e. point O in figure 3.14(a). The downstream co-ordinate \tilde{s} has been scaled by the bend length $\tilde{s}_{bend} = \tilde{s}/2$.

The width is shown to spatially oscillate at twice the wavelength of curvature. The bed elevation at the left and right banks shows a primary oscillation at the wavelength of curvature, but hidden in the variation is a second harmonic. This second harmonic, which appears only when nonlinear effects are included in the numerical model (section 3.4.1), is readily seen in terms of centerline bed elevation, which, like width, oscillates at twice the wavelength of curvature. This prominent second harmonic at the channel centerline is present even for the case of a constant-width channel. It has been considered to be an indication of a tendency for central bars to emerge (Luchi et al, 2010) and has been used as a basis for the “curvature-forced” mechanism for mid-channel bar development proposed by Luchi et al. (2010).

Figure 3.15 shows that for the base run, the width maximum falls just upstream of the bend apex, and the minimum somewhat farther downstream of it. The bends of the Pembina do indeed

show this behavior, as can be seen in figure 3.7. The centerline bed elevation responds in kind with its peak located just upstream of the bend apex.

At this point it is useful to recall the analysis of field data in Section 3.2, in which local dimensionless width b is plotted against the absolute value of local dimensionless curvature $|c|$ (figures 3.4 and 3.5). In the field data, the width-curvature correlation over multiple bends appears as a series of scatter points to which we have fit a regression line. Along one wavelength of single bend, however, the correlation appears as a loop, with width varying with curvature along the bend. For the simplified case of a periodic channel, the result is a closed loop. Figure 3.17 shows this loop for the base case, at time $t = 498$ years. Also shown is the corresponding loop for deviatoric bed elevation along the centerline denoted as c_c , to distinguish from the cross-sectionally averaged deviatoric bed elevation c_{dc} . The arrows denote the path from the inflection point (where $c = 0$) downstream to the point of maximum curvature magnitude $|c|$, and then farther downstream to the next inflection point.

It is seen in the figure that width increases with increasing curvature downstream of the inflection point A, and reaches a maximum at point B, somewhat upstream of point C corresponding to the bend apex (maximum $|c|$). Downstream of point B, width then decreases. At the bend apex, width differs little from the value at the inflection point. Farther downstream, width reaches a minimum at point D, located well downstream of the apex C. Width then increases from point D to point A, which now corresponds to the next inflection point downstream. Over time, this loop expands outwards during the growth phase of the planimetric evolution envelope and subsequently shrinks inward as incipient cutoff is reach.

The corresponding loop for deviatoric centerline bed elevation w_c in figure 3.16 also shows an increase in bed elevation downstream of the inflection point A' to a maximum at B', which is just downstream of the maximum in curvature B. Deviatoric centerline bed elevation then declines farther downstream, but is still well above zero at the bend apex C'. Minimum deviatoric centerline bed elevation continues to decline to point D', located somewhat downstream of the point of minimum width D, and then increases back to point A' corresponding to the next inflection point downstream. The width at the apex is shown to be nearly the same as that at the crossing. Having said this, the point of width maximum is upstream of the apex, and closer to the apex than the nearest crossing, which is in line with the general trends observed in figures 3.7.

To show how correlation trends change over time as the bend develops toward incipient cut-off, let w_{apex} , w_{Bmax} , w_{Bmin} , w_{cmax} denote the respective dimensionless phase distances, from an upstream inflection point to the location of the curvature maximum, width maximum, width minimum and centerline bed elevation maximum respectively. The phase distance represents an arc length that has been rescaled by the channel bend length \tilde{l}_{bend} such that it ranges from 0 at the upstream inflection point to 1 at the downstream inflection point. The time variation of w_{apex} , w_{Bmax} , w_{Bmin} , w_{cmax} is shown in figure 3.17(a). The figure also shows the phase distance to the location of maximum centerline migration rate w_M .

In figure 3.17(a), the point $w = 0.5$ corresponds to half the distance from inflection point to the next inflection point downstream. Thus $0 < w < 0.5$ corresponds to the upstream half of the bend, and $0.5 < w < 1$ corresponds to the downstream half. It is seen from the curve of w_{apex} in the

figure that the bend apex quickly moves into the upstream half of the bend, and stays there until incipient cut-off. This corresponds to bends that are skewed upstream, (e.g. Parker et al., 1983).

The curves of W_{Bmax} and W_{Bmin} in figure 3.18(a) indicate that maximum width is always attained upstream of the apex, and minimum width is always attained downstream of the apex. The bend apex always falls downstream of the point of maximum width and upstream of the point of minimum width, but is closer to the point of maximum width. The point of maximum width is always in the upstream half of the bend; this trajectory is also tracked by the phase location $W_{y_{cmax}}$ corresponding to maximum deviatoric centerline bed elevation. The location of minimum width W_{Bmin} shifts from the upstream half to the downstream half of the bend as the meander train evolves. The location of maximum migration rate W_M tracks the location of minimum width.

Another way to measure width-curvature-bed elevation phasing is to define the phase distance relative to the bend apex, S , as:

$$\check{S}_q = \begin{cases} \frac{W_q - W_{apex}}{W_u} & W_q - W_{apex} < 0 \\ \frac{W_q - W_{apex}}{W_d} & W_q - W_{apex} > 0 \end{cases} \quad (3.69)$$

where q is a given variable (e.g. $q = y_{dc}$ for deviatoric centerline bed elevation) and W_u and W_d denote the upstream and downstream phase distance relative to the bend apex as defined in figure 3.17(a), so that the two sum to unity. The parameter \check{S}_q is thus defined such that it varies from -1 to 1 with 0 corresponding to the bend apex and -1 and 1 corresponding to the upstream and downstream inflection points respectively. The variations over time of location of the width

maximum \tilde{S}_{Bmax} , width minimum \tilde{S}_{Bmin} , maximum deviatoric centerline bed elevation \tilde{S}_{ycmax} and maximum migration rate \tilde{S}_M are shown in figure 3.17(b). In the figure we see that over time, the normalized locations of the width maximum and deviatoric central bed elevation maximum remain fairly constant at approximately $\tilde{S} = -0.3$. The locations of the width minimum and maximum migration rate, on the other hand, shows significant change during bend development, but eventually approach an asymptote of $\tilde{S} = 0.25$ up to incipient cutoff.

3.5.4. Model sensitivity to channel parameters

Changes to the aspect ratio, grain size and initial wavelength were found to alter the lateral migration rates predicted by the model. For example, a reduction in the initial aspect ratio χ_{oi} from the base value was found to result in lower curvature peaks as well as reduced channel migration rates. Increased sediment size also resulted in a decrease in migration rates. Increasing the initial channel wavenumber $|$ (i.e. decreasing the wavelength) from the base value, however, was found to increase the migration rate and yield a higher curvature peak. These tendencies, were computed by performing the G runs (variation in χ_{oi}), D runs (variation in D_s) and L runs (variation in $|$) of table 3.3. The results are summarized in figure 3.18.

Figures 3.18(a), 3.18(b) and 3.18(c) all show time trajectories of width variation intensity u versus down-channel meander wavenumber $|$. In all cases temporal variation is from right to left, as indicated by the curved arrow in figure 3.18(a). The sensitivity of this trajectory to variation in initial aspect ratio χ_{oi} is shown in figure 3.18(a); the sensitivity to varied dimensionless grain size D_s is shown in figure 3.18(b), and the sensitivity for varied initial wavenumber $|_i$ is shown in

figure 3.18(c). The base case is shown as the thick black line for each figure. The straight arrow denotes the direction of increase of the parameter in question.

For each case, as the channel evolves over time, the channel wavenumber steadily drops, corresponding to increasing sinuosity. As time passes and wavenumber drops, the intensity of width variation increases, reaches a peak, and then declines. The magnitude of this peak evidently increases with increasing initial aspect ratio χ_{oi} and initial wavenumber $|i$. Although the behavior is less consistent in terms of grain size, a grain size that is five times the base value results in a near-doubling of width variation intensity.

The phasing of width oscillation with respect to curvature is also impacted by changes to the parameters χ_{oi} , D_s and $|i$. This sensitivity is illustrated in terms of the time trajectories of \check{S}_{Bmax} and \check{S}_{Bmin} versus $|$ given in figures 3.19(a), 3.19(b) and 3.19(c). In all cases temporal evolution is from right to left, i.e. the direction of increasing wavenumber $|$. The general trend is for the location of the width minimum to be shifted upstream toward the bend apex as sinuosity increases over time. This is seen in all cases shown in figure 3.19. The width minimum shifts upstream for increasing χ_{oi} and downstream for increasing grain size. The location of the width maximum is largely unaffected by χ_{oi} , but shows a significant downstream shift toward the bend apex for larger grain sizes.

In all the above simulations shown, while width-curvature trajectory is seen to change with changing input parameters, the general tendency is for the width maximum to be located just upstream of the bend apex and for the minimum to be located slightly to significantly downstream.

In the next section, however, we show that this pattern is a strong function of the reference erosion and deposition rates. We study this by varying their ratio (Υ runs of table 3.3)

3.5.5. Model sensitivity to bank parameters

Figure 3.20 shows results for bed topography and bank lines obtained from model simulations from the Υ runs of table 3.3, where the ratio of the reference erosion rate to reference deposition rate $\Upsilon = \tilde{i}_{Eref} / \tilde{i}_{veg}$ is varied by holding the erosion rate \tilde{i}_{Eref} constant and varying the deposition rate \tilde{i}_{veg} accordingly. More specifically in addition to the base value $\Upsilon = 0.5$, the values 0.25, 0.75, 1.0, 1.25 and 1.5 are also considered. Again each snapshot shown here represents the time at which curvature reaches the peak of its envelope curve (e.g. figure 3.15a). The values of the peak curvature and migration rates for each of the snapshots are indicated in the figure.

In the figures, the bank lines correspond to the bounds of the central region of figure 3.8. The contour lines shown indicate dimensionless relative bed elevation. The near zero contour of 0.05 has been highlighted to better visualize the point bar configuration in each plot. Here we define the point bar in terms of the portion of the channel between the 0.05 contour and the lower bank in the plot.

Figures 3.20(a) ~ 3.20(f) show a steady progression in pattern as Υ increases. This is most readily seen in terms of the two points, A and B, in figure 3.20(a). Point A, marked with a solid arrow, shows the position of maximum width for $\Upsilon = 0.25$, and point B, marked with an open arrow, shows the position of minimum width for the same value of Υ . These same positions are marked with corresponding solid and open arrows for the cases $\Upsilon = 0.50, 0.75, 1.0, 1.25$ and 1.5

in figures 3.20b ~ 3.20f, respectively. The width at the point of the solid arrow monotonically decreases with increasing Υ , so that the point becomes very nearly the narrowest point on the bend for $\Upsilon = 1.50$. The width at the point of the open arrow monotonically increases with increasing Υ , so that this point is not too far of the width maximum at $\Upsilon = 1.5$. The systematic variation of width at the points of the solid and open arrows is illustrated in figure 3.20.

It can also be seen that as Υ increases from 0.25 to 1.50, the intensity of width variation first decreases, and then increases. A corresponding pattern can be seen somewhat downstream of the bend apex at point “B”, with monotonically increasing width as Υ increases from 0.25 to 1.50. The value of the dimensionless width at point A and B for each of the cases shown in figure 3.20 are plotted as a function of Υ in figure 3.21.

The case $\Upsilon = 0.5$ shown in figure 3.20(b) is of particular interest because it corresponds to the base case. It is seen from the figure that the model predicts a point of maximum width that lies upstream of the bend apex just as seen in the field.

The teardrop shape of the point bar delineated by the 0.05 bed elevation contour line also undergoes a systematic transition as Υ increases, with the locus of maximum bar width moving from upstream of the bend apex to downstream of it.

This systematic change in the pattern of width variation with increasing Υ may be one reason why each of the four field cases shown in figures 3.4 and 3.5 shows a different relation for b versus $|c|$.

Bend migration patterns can be characterized in terms of “bank pull” and “bar push”. Based on Stillwater Science (2007), Eke et al. (submitted) defined these as follows: a cross-section is undergoing bank pull when the eroding bank is migrating faster than the depositing bank, and it undergoes bar push when the depositing bank is migrating faster than the eroding bank. Stillwater Science (2007) relates these modes of migration to the effect of topographic steering of the flow by the point bar.

It might be thought that an increase in $\Upsilon = \tilde{i}_{Eref} / \tilde{i}_{veg}$ would engender an across-the-board increase in erosion-dominated migration (bank pull) over deposition-dominated migration (bar push). The behavior predicted by the model is at variance with this. In the present model, the overall, the net migration pattern tends to be predominantly deposition-dominated, due to the net reduction in channel width over time documented in figure 3.13. However, within the channel itself, it has been observed that there is a spatial distribution of patterns of bank-pull and bar-push. These have been documented through field and experimental observation to correlate with the location of the point bar (Stillwater Science, 2007).

Figure 3.22 shows the centerline curvature distribution for cases corresponding to $\Upsilon = 0.25, 0.5, 1.25$ and 1.5 in figure 3.20. The shaded regions indicates zones where bank pull is the dominant channel migration mechanism. Regions without shading are dominated by bar push.

As shown in figure 3.22, for lower values of Υ , bank pull zones are found close to the bend apex, but downstream of it. As Υ increases, these zones migrate upstream, even as the location of the width maximum, as documented in figure 3.20, migrates downstream. Figures 3.20 and 3.22 present a consistent picture of the effect of topographic steering in meander bends. The

presence of significant width variation and the accompanying enlarged pointbar upstream of the bend apex steers flow toward the outer bank upstream, causing an elevated erosion rate at or downstream of the bend apex. Thus as the width maximum shifts downstream towards the inflection point, the zone of elevated erosion rates shifts accordingly.

In Figure 3.23, width b , centerline bed elevation, y_C and centerline water surface elevation ζ_C are plotted against curvature magnitude $|c|$ for the cases $\Upsilon = 0.25, 0.75$ and 1.5 of the Υ runs of Table 3. This figure documents a transition from a generally positive correlation between width and curvature for $\Upsilon = 0.25$ to a generally negative one for $\Upsilon = 1.25$, similar to the transition observed in the field data comparison between the Vermillion River and Trinity River Reaches in Section 3.2. This suggests that the present model can encompass the full range of trends documented in figures 3.4 and 3.5, including the positively-correlated case of the Trinity River and the negatively correlated case of the Vermillion River.

The case of figure 3.23b is of particular interest, because it corresponds to the base case $\Upsilon = 0.5$ for the Pembina River. The predicted trend is for width to be positively correlated with the magnitude of curvature, as is indeed the case for in the field (figure 3.4).

Figure 3.23 also shows that the magnitude of the deviatoric centerline bed oscillation y_C varies with the intensity of width variation. For the cases $\Upsilon = 0.25$ and $\Upsilon = 1.5$, corresponding to significant width variation, the values of y_C are significantly greater than for the $\Upsilon = 0.75$, corresponding to very little width variation.

The above result is significant in the light of the recent work of Luchi et al. (2012) where an analytical model was developed to predict channel width variation for the equilibrium river. They hypothesized that the width variation observed in an equilibrium channel should correspond to the one that yields the least streamwise variation in centerline water surface elevation ζ_C , and thus the most nearly streamwise-constant water surface slope. They furthermore showed that this constraint results in a pattern of width variation such that width is maximum close to the crossings. Here, however, we find that the predicted pattern of width oscillation is not necessarily associated with, nor does it require, any tendency toward constant centerline water surface slope. Rather, the patterns of spatial variation of width, centerline bed elevation and centerline water surface elevation are functions of (among other things) the dimensionless parameter Υ corresponding to the reference erosion rate divided by the reference deposition rate.

3.6 Discussion

The model presented above has at least three limitations. Firstly, it is applicable only to bedload-dominated rivers. In order to extend it to suspension-dominated rivers, the sediment transport needs to be reformulated so as to a) divide bed material load into bedload and suspended load, b) apply separate transport equations, and c) calculate transverse load under the influence of gravity solely from bedload.

Secondly, the model cannot capture the formation and migration of free bars (e.g. Seminara, 2006). This is because it uses a specific variant of quasi-steady assumption; the characteristic time for planform adjustment is assumed to be sufficiently long compared to bed

adjustment so as to allow a steady-state solution for bed morphology. The model of Asahi et al. (2013) discussed below is not subject to this constraint.

Thirdly, the model captures only one type of natural armoring, i.e. slump blocks. In some cases, induration of otherwise non-cohesive floodplain sediment may act to throttle bank erosion below its default non-cohesive value. In relatively large streams, fallen trees and tree stumps may be more effective units of natural armoring than slump blocks (Konsoer et al., 2012).

Having said this, the parameters entering into the submodels for bank erosion and deposition are all physically measurable quantities. More specifically, the parameters $\tilde{\tau}_{veg}$ = default rate of vegetal encroachment in the absence of near-bank shear stress long enough to limit it, \tilde{H}_c = characteristic thickness of the cut bank cohesive layer, \tilde{D}_c = characteristic size of the slump blocks and \tilde{T}_c = characteristic residence time of slump blocks are all measurable in the field. The model assumes fairly simple relations for the way in which deposition rate $\tilde{\tau}_D$ decreases, and erosion rate $\tilde{\tau}_E$ increases, with increasing near-bank Shields number. These relations can be refined as more field data become available.

The model presented here merits comparison with that of Asahi et al. (2013). An advantage of the model of Asahi et al. (2013) compared to the present one is that it encompasses free bars, and thus leads to a rather more complex pattern than that observed here. A disadvantage is that their model cannot yet be applied at field scale, whereas the present model has been applied using input values from the meandering Pembina River, Alberta, Canada. In addition, the model of Asahi

et al. is not yet able to fully describe how average width is maintained in meandering rivers. All these limitations could be overcome by means of a future amalgamation of the two models.

The treatment of Asahi et al. (2013) for bank erosion is similar to the one used here. The treatment of bank deposition, however, is different. The present analysis assumes a default rate of deposition associated with unrestricted vegetal encroachment, which is then reduced as near-bank bed shear stress during floods is increased. Asahi et al. (2013) a) assume a two-step hydrograph, and b) assigns a characteristic time T_{land} for exposed point bar to become stabilized by vegetation. Once a zone of the bed has been exposed for this time, it is stabilized, and is no longer a part of the riverbed. The only way the material can be removed is the river later erodes into it. For the same flood return period, larger values of T_{land} result in wider channels, due the decreasing effectiveness of vegetal stabilization.

In the present analysis, flow hydrograph is not explicitly modeled. Instead, it is implicitly modeled via the forms (3.50) and (3.55) for the bank erosion rate and deposition rate, respectively. The former is proportional to flood intermittency I_f , so that longer flood flows yield higher erosion rates. The latter is proportional to the fraction of time $(1 - I_f)$ corresponding to low flow, but decreases with increasing near-bank bed shear stress during floods, when vegetation can be partially or completely uprooted.

One way to bring the models into closer accord is the addition of a time lag effect in (3.55), so that

$$\tilde{\tau}_D = \tilde{\tau}_{veg} [(1 - I_f) - I_{lag}] \left(1 - \frac{\dagger_D^*}{\dagger_{form}^*} \right) \quad (3.70)$$

Here I_{lag} corresponds to a fraction of the low-flow period necessary for the vegetation to take root. Larger values of I_{lag} might correspond to vegetation types that take longer to become established, or coarser point bar sediment which inhibits establishment.

A final limitation of both this model and that of Asahi et al. (2013) is that while they can erode floodplain, they cannot build floodplain above the top of the point bar. The formulation of morphodynamic models of meandering rivers will not be complete until the floodplain, as well as the channel is self-formed. A basis for the formulation of a model that accounts for both the channel sediment material gained from channel erosion and that lost as the channel deposits and builds its floodplain can be found in Lauer and Parker (2008).

3.7. Conclusions

A large body of research on the theoretical and numerical simulation of the migration of meandering rivers is based on the HIPS model (Hasegawa, 1977; Ikeda et al., 1981). This formulation assumes that the river maintains a constant, prescribed width as it migrates. Since the time of that research, however, it has been shown that meandering rivers show systematic spatial patterns of width variation (Brice, 1982; Lagasse et al., 2004).

We use field data from five river reaches to demonstrate the existence of a range of patterns of spatial variation of width in meandering rivers. One end member is the case of the Trinity River, Texas, USA, where width shows strong positive correlation with the absolute value of centerline curvature. In this case, points near apexes tend to be wider than points near crossings. The other

end member is the case of the Vermillion River, Minnesota, USA, where width shows weak negative correlation with curvature. In the case of the Suwannee and Apalachicola Rivers, Florida, USA and the Pembina River, Alberta, Canada, maximum width tends to occur upstream of the bend apex, whereas in Trinity River, maximum width tends to occur downstream of the bend apex, and in the case of the Vermillion River, both cases are equally likely.

We invoke a physically-based numerical model for self-formed, co-evolving channel planform and width variation to study the underlying causes for these patterns. Our model uses the framework of Parker et al. (2011), applied to a stream for which bedload is the dominant mode of sediment transport. More specifically, it uses the submodels given in Eke et al. (submitted, Chapter 2) for bank erosion and deposition. In the case of an eroding bank, slump block armoring acts to hold the bank erosion rate well below the value that would prevail in the case of purely non-cohesive material. In the case of a depositing bank, vegetal encroachment stabilizes otherwise loose point bar sediment, causing the bankline to advance. As opposed to the earlier HIPS model of meander migration (Hasegawa, 1977; Ikeda et al., 1981), all of the input parameters pertaining to physical quantities in the two submodels are at least potentially measurable in the field.

A model that predicts width variation must also be capable of predicting overall mean width as well. This is accomplished in terms of three relations: a relation for momentum balance, a relation for bedload transport and a relation for channel-forming (bankfull) Shields number. In previous implementations of this formulation (e.g. Parker et al., 1998), channel-forming Shields number has been taken to be a prescribed constant. The resulting relations predict a bankfull width that varies inversely with bed slope. Here we show that as sinuosity increases, and thus mean down-channel bed slope decreases, such a relation applied to meandering streams predicts a drastic

decrease in bankfull width. Li et al. (submitted, Appendix B) have shown, however, that bankfull Shields number is an increasing function of slope. We show here that this formulation overcomes the problem of over-narrowing; bankfull width decreases only mildly as sinuosity increases.

The following two parameters play key roles; the default rate of migration of a depositing bank, $\tilde{\tau}_{veg}$ due to vegetal encroachment in the absence of flood flow, and a reference rate of migration of an eroding bank $\tilde{\tau}_{Eref}$ that corresponds to a near-bank bed shear stress that is twice the bankfull value. In applying our model to a reach of the Pembina River we find that the dimensionless parameter $\Upsilon = \tilde{\tau}_{Eref} / \tilde{\tau}_{veg}$ controls the mode of spatial width variation. As Υ increases from 0.25 to 1.5, a) the point of maximum width shifts from a position upstream of the apex to a position downstream of it, and b) the correlation between width and the magnitude of curvature shifts from positive to negative, and c) the locus of bank pull migrates from downstream of the apex to upstream of it. The case of least width variation is seen when Υ is near the intermediate value 0.75.

The predictions thus span the patterns of variation observed across the five field examples. It is not possible to compare the results directly with each of the five field examples, because the applicable input parameters are likely to be different from reach to reach. The predictions for the base case $\Upsilon = 0.5$ of the Pembina River are, however, in agreement with the trends in the observations: width correlates positively with the absolute value of curvature, and the position of the width maximum is located upstream of the bend apex.

The model for meander evolution presented here does not necessarily render the HIPS formulation obsolete. In the case $\Upsilon = 0.75$, for example, width variation is predicted to be modest. There may be a range of conditions for which the results of the present model for planform evolution do not differ too much from a parallel HIPS implementation with appropriately chosen input parameters. Such a parallel implementation and comparison should be a goal of future research. Another goal should be the melding of the present formulation and that of Asahi et al. (2013) into a single, unified formulation.

This research represents a contribution of the National Center for Earth-surface Dynamics, a Science and Technology Center funded by the US National Science Foundation (agreement EAR-0120914). We thank R. Luchi for valuable advice on the research and the text.

Tables

	<i>Bankfull Depth (m)</i>	<i>Slope (m/m)</i>	<i>Bankfull width (m)</i>	<i>Sinuosity</i>	<i>Mean grain size (mm)</i>	<i>Migration rate (m/yr)</i>
<i>Vermillion</i>	0.75	5.18×10^{-4}	15	2.62	2	0.75
<i>Trinity</i>	3.85	1.24×10^{-4}	190.4	1.78	0.35	2.3
<i>Pembina</i>	3.75	2.60×10^{-4}	91	1.9	0.4	2-5 (peak)

Table 3.1. Characteristics of study reaches

<i>Parameter</i>	<i>Value</i>	<i>Description</i>
\tilde{Q}_o (m ³ /s)	405	Bankfull discharge
$2\tilde{b}_{oi}$ (m)	99.7	Initial bankfull width
\tilde{H}_{oi} (m)	2.85	Initial bankfull depth
S_{oi}	0.00049	Initial mean channel centerline slope
\tilde{D}_s (mm)	2	Characteristic grain size
$\ddagger_{form,i}^*$	0.426	Initial channel-forming Shields number
I_f, I_{fref}	0.2	Flood intermittencies
$S_{s,LB}; S_{s,RB}$	-1.5; 1.5	Bank side slope
$H_{b,LB}; H_{b,RB}$ (m)	2.5	Thickness of non-cohesive layer
H_c (m)	1.25	Cohesive layer thickness
p_c	0.6	Cohesive layer porosity
i_{Eref}^{\sim} (m/yr)	5	Reference slump block-modulated bank erosion rate
i_{veg}^{\sim} (m/yr)	10	Default vegetal encroachment rate

Table 3.2. Summary of input parameters for base run based on the Pembina River in Alberta, Canada. The subscript *i* indicates initial values of parameters that change over time

<i>Run</i>	$\chi_{oi} = \tilde{b}_{oi} / \tilde{H}_{oi}$	$D_s = \tilde{D}_s / \tilde{H}_o$	$\dagger_{form,i}^*$	$ _i = 2f \tilde{b}_{oi} / \tilde{y}_i$	$\Upsilon = \tilde{I}_{Eref} / \tilde{I}_{veg}$
<i>Base</i>	17.5	0.0007	0.43	0.16	0.5
<i>G</i>	8.6-17.5	0.0007	0.43	0.16	0.5
<i>D</i>	17.5	0.0007-0.0035	0.85-0.17	0.16	0.5
<i>L</i>	17.5	0.0007	0.43	0.1-0.21	0.5
<i>Y</i>	17.5	0.0007	0.43	0.16	0.25-1.5

Table 3.3. Input conditions for different numerical runs to find the effect of non-dimensional parameters on width curvature correlation. The subscript *i* indicates initial values of parameters that change over time

Figures



Figure 3.1. Meandering river reaches showing width variation. (a) Ob River, Russia. (b) Trinity River, Texas, USA. (c) Vermillion River, Minnesota, USA. Arrows indicate direction of flow. For scale, typical river widths are 150 m, 190 m, and 15 m for cases a), b) and c) respectively.

The images are from Google Earth.

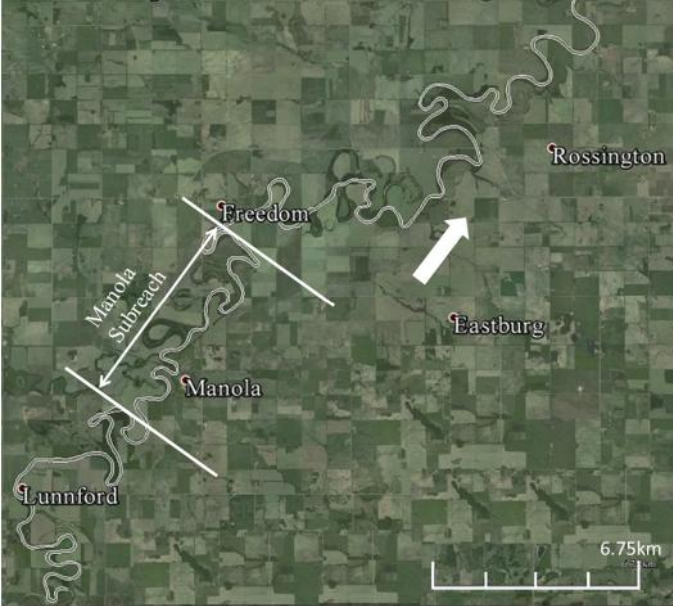


Figure 3.2. Study reach of the Pembina River Reach in Alberta, Canada. The arrow indicates direction of flow.

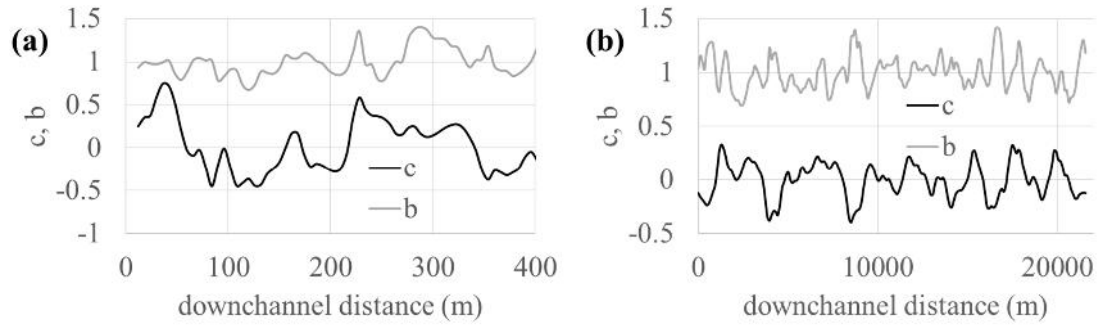


Figure 3.3. Downchannel variation of dimensionless centerline curvature and dimensionless channel half-width: (a) Vermillion River; (b) Trinity River.

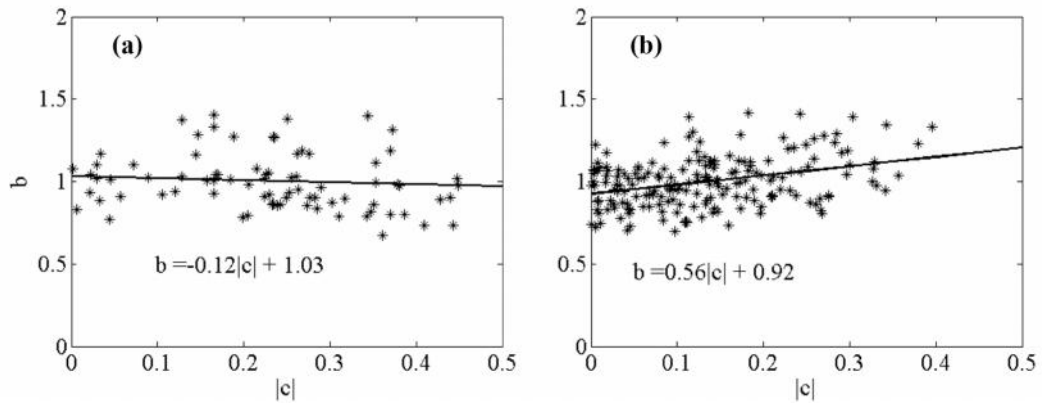


Figure 3.4. Linear regressions of dimensionless channel half-width and dimensionless centerline curvature correlation: (a) Vermillion River; (b) Trinity River. The stars indicate the data.

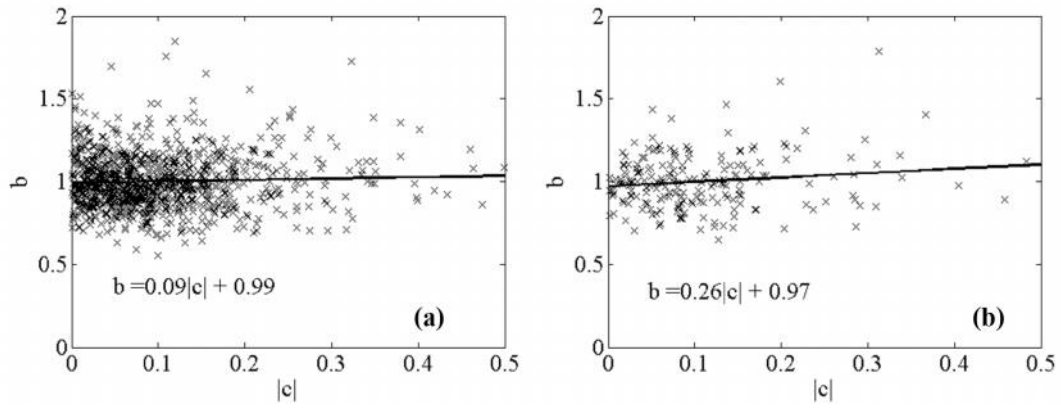


Figure 3.5. Linear Regression of dimensionless channel half-width and dimensionless centerline curvature correlation for the Pembina River. (a) The entire Pembina reach near Rossington (b) Manola subreach. The 'x's indicate the data and the line is a linear fit to the data.

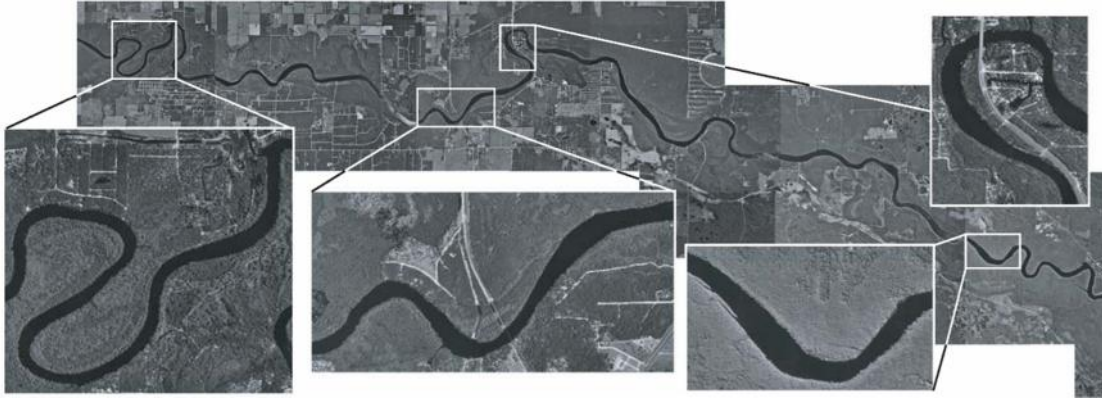


Figure 3.6. View of the study reach of the Suwannee River. Flow is from left to right. The bend in the leftmost insert has a minimum width of 68 meters and a maximum width of 104 meters².

² This figure was compiled by Sun Tao, a co-author of this manuscript

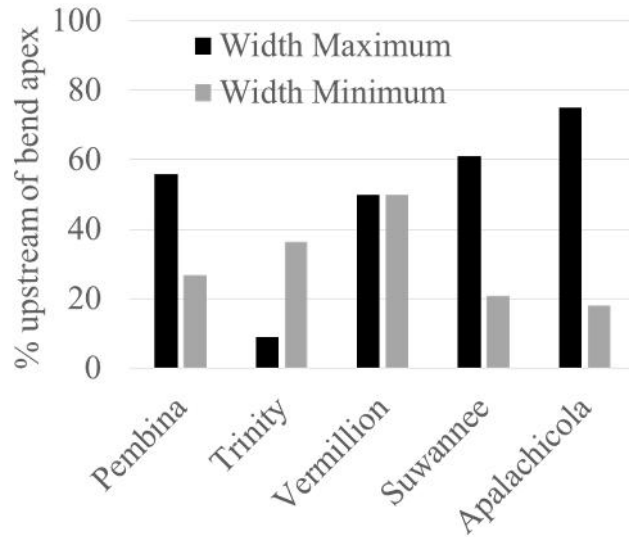


Figure 3.7. Percentage of bends in which the location of the width maximum and width minimum are upstream of the bend apex for five river reaches: the Pembina River, the Trinity River, the Vermillion River, the Suwannee River and the Apalachicola River³

³ Data on the Suwanee and Apalachicola Rivers were compiled by Sun Tao, a co-author of this manuscript

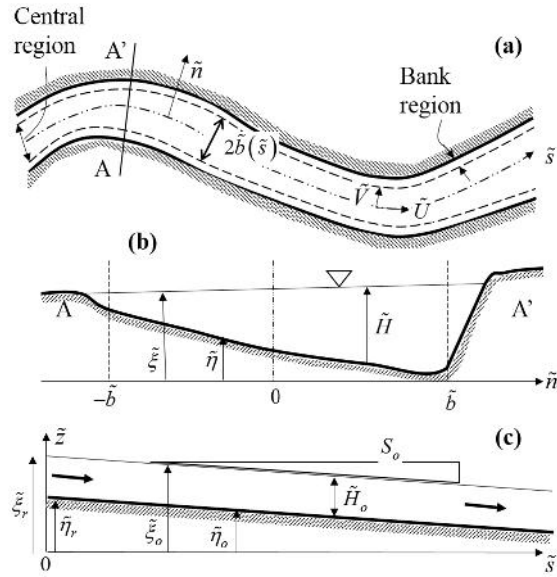


Figure 3.8. Definition sketch of channel (a) Planform (b) cross-section (c) reference straight channel. Modified from Beck (1983).

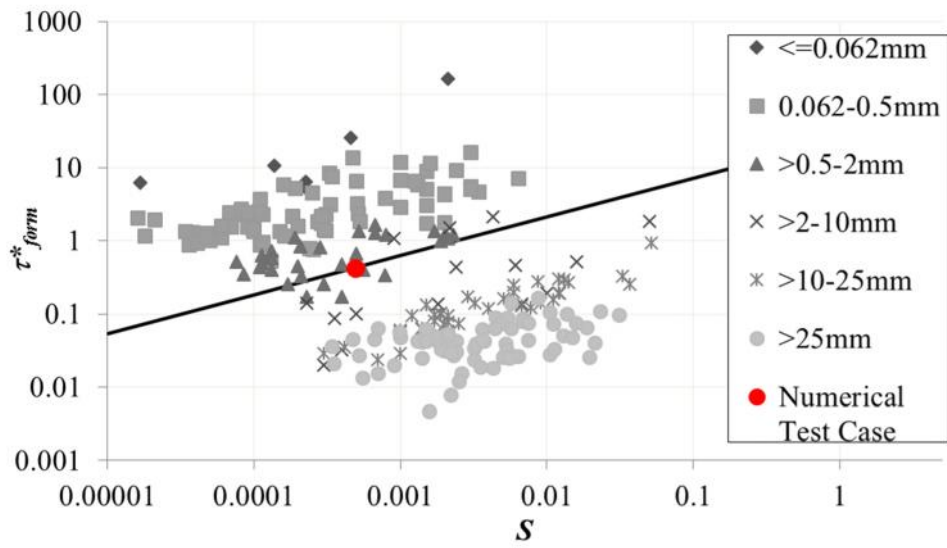


Figure 3.9. Channel forming (bankfull) Shields number versus channel slope S . Dataset for bankfull geometry are from Parker et al. (2007) and Wilkerson and Parker (2010). A point for the numerical test reach considered here, for which $\tilde{D}_s = 2\text{mm}$, has been added to the figure. Also shown is the line corresponding to (3.12).

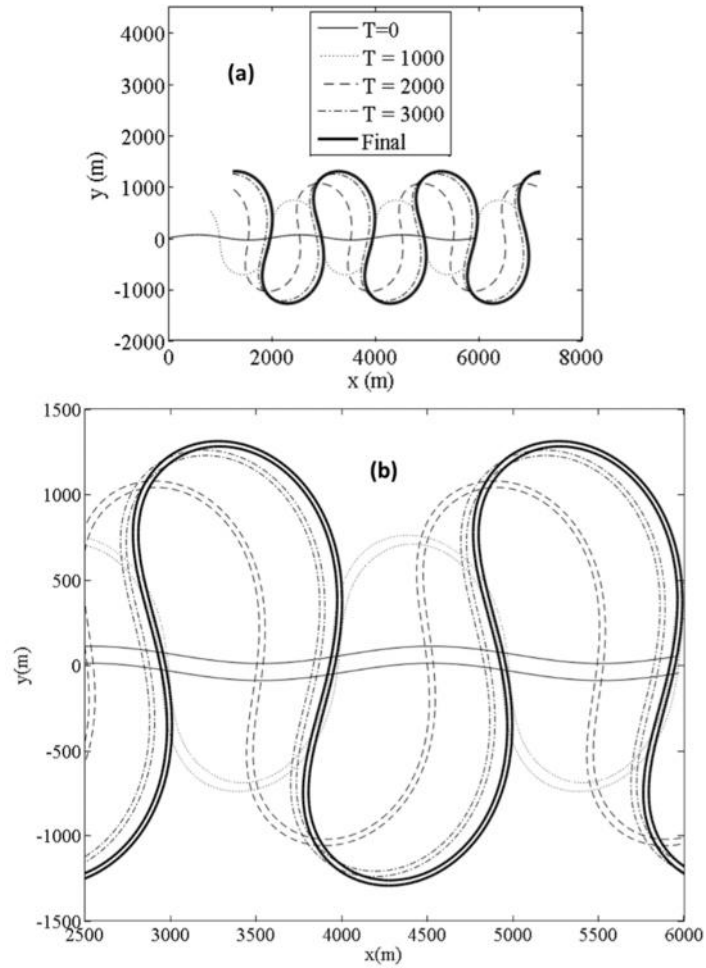


Figure 3.10. An example model simulation of an idealized periodic channel from an initial low amplitude to high amplitude, with constant channel-forming Shields number. (a) Centerline migration over time (b) Planform showing evolution of channel width over time. Time indicated is in years.

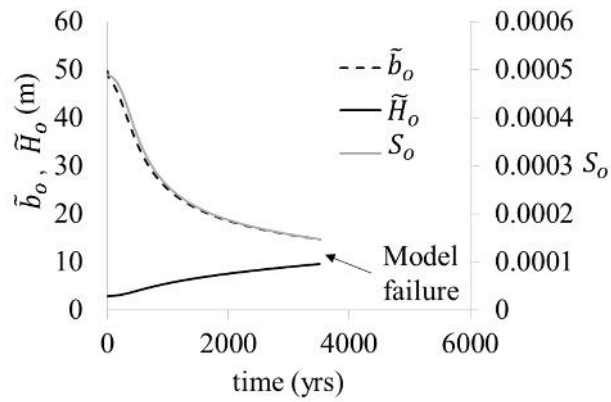


Figure 3.11. Reference channel adjustment over time in response to increasing channel sinuosity.

As slope S_o reduces, the channel half-width \tilde{b}_o reduces and flow depth \tilde{H}_o increases. Model results assume a constant channel-forming Shields number.

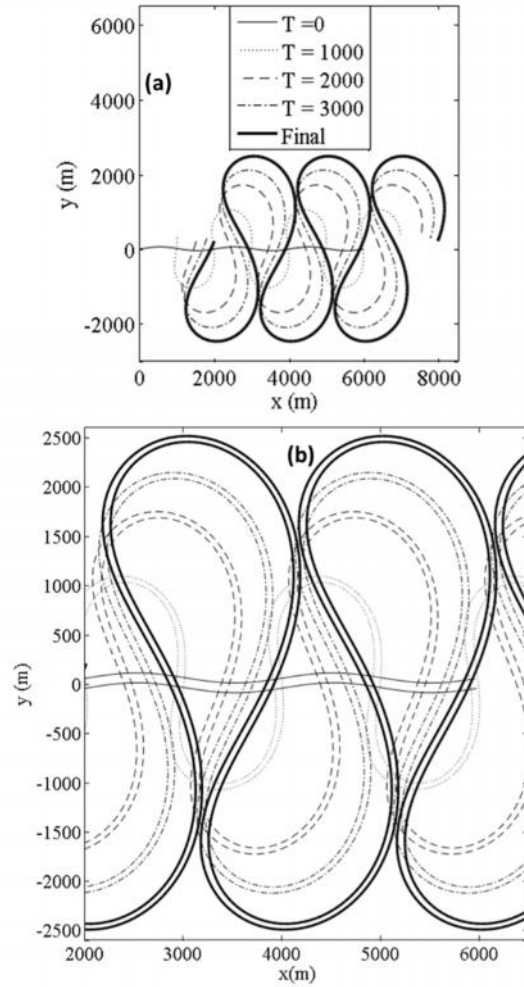


Figure 3.12. An example model simulation of an idealized periodic channel from an initial low amplitude to high amplitude, with slope-dependent channel-forming Shields number. (a) Centerline migration over time (b) Planform showing evolution of channel width over time. Time indicated is in years.

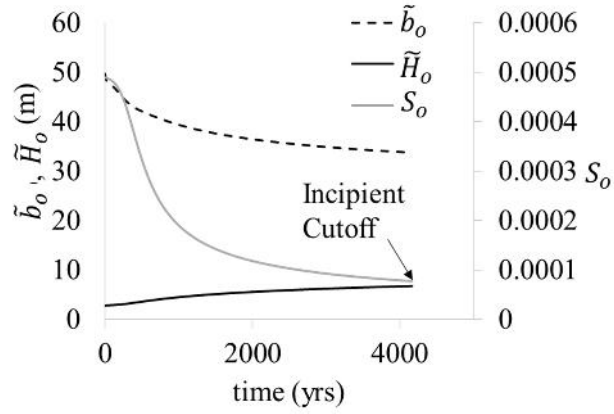


Figure 3.13. Reference channel adjustment over time in response to increasing channel sinuosity.

As slope S_o reduces, the channel half-width \tilde{b}_o reduces and flow depth \tilde{H}_o increases. Model results assume a slope-dependent channel-forming Shields number.

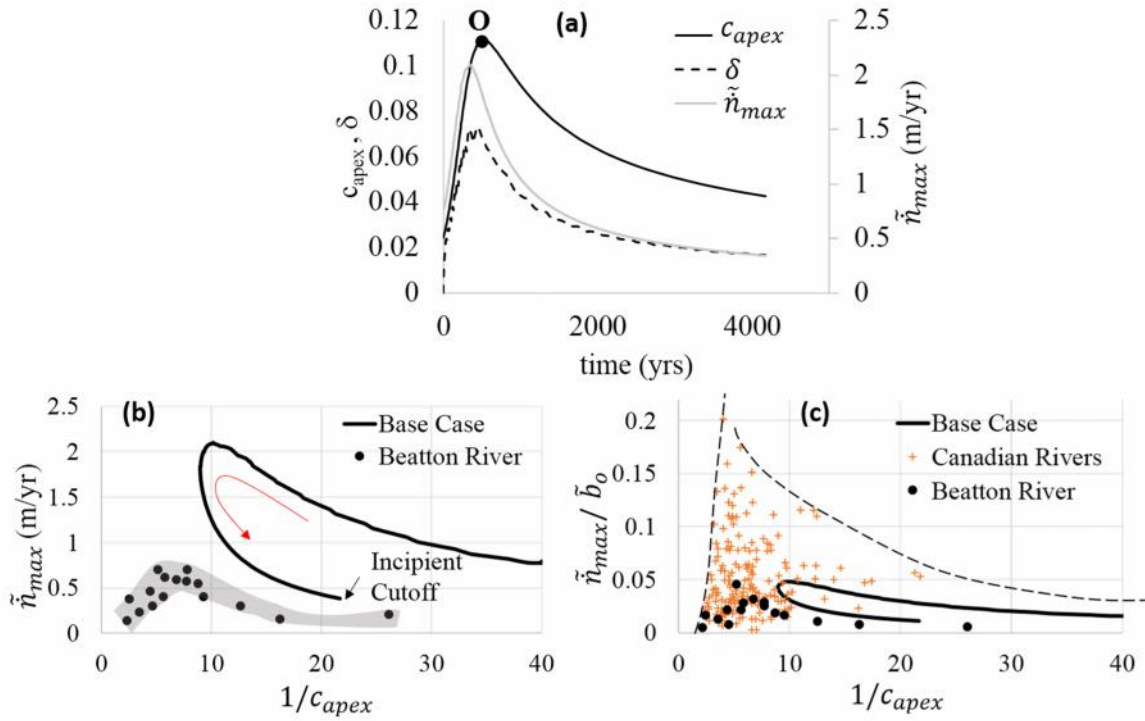


Figure 3.14. Channel evolution characteristics for the base run. (a) variation of peak curvature c_{apex} , centerline migration rate \dot{n}_{max} and width variation amplitude δ over time (b) computed hysteresis loop for centerline migration rate. The arrow indicates direction of trajectory from low amplitude meander to incipient cut-off. Also shown are data from the Beatton River, Canada (c) relation between migration rate and bend curvature, showing the Beatton River and 21 other Canadian rivers. Data shown are from Hickin and Nanson (1984).

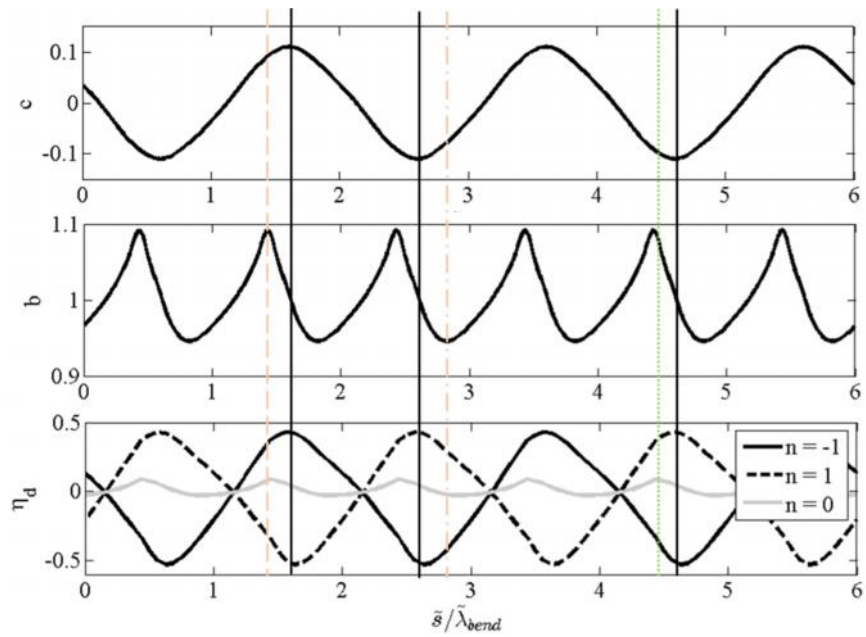


Figure 3.15. Downstream variation in dimensionless curvature c , half-width b and relative bed elevation η_d at time $t = 498$ yrs corresponding to peak bend amplitude (point O in figure 3.14a).

Continuous vertical lines indicate bend apex location, thin red dash lines indicate maximum width, thin red dash-dot lines indicate location of minimum width, and thin green dotted lines indication location of maximum centerline bed elevation.

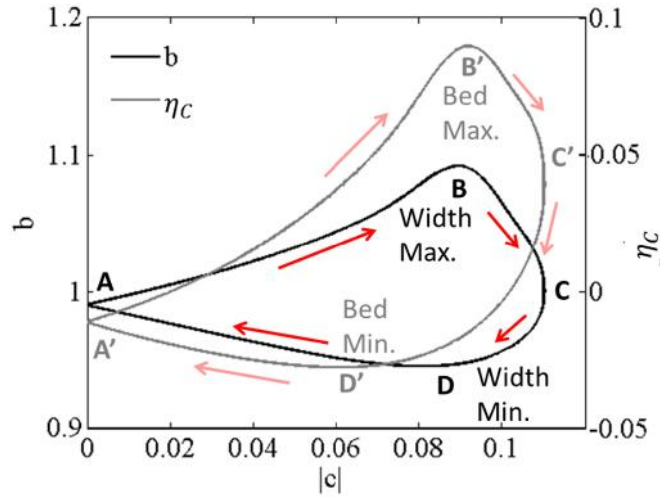


Figure 3.16. Loop curves along a meander bend at $t = 498$ years for width b and deviatoric centerline bed elevation y_c as functions of the absolute value of curvature. The locations A, B, C and D correspond respectively to the inflection point, point of maximum width, point of maximum curvature and point of minimum width along the loop for b . The points A', B', C' and D' correspond respectively to the inflection point, point of maximum deviatoric bed elevation, point of maximum curvature and point of minimum deviatoric bed elevation along the loop for y_c . Arrows indicate direction of trajectory.

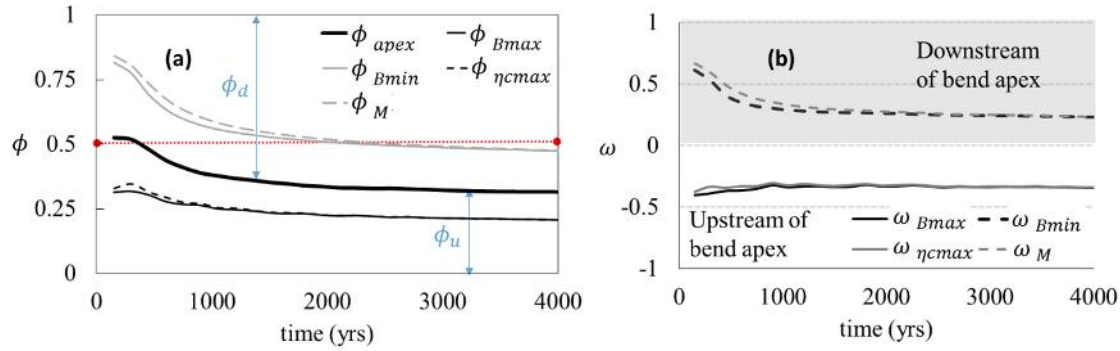


Figure 3.17. Plots of time variation of normalized along-channel location of width maximum (ω_{Bmax} on left, \check{S}_{Bmax} on right), maximum deviatoric centerline bed elevation (ω_{ycmax} on left, \check{S}_{ycmax} on right), width minimum (ω_{Bmin} on left, \check{S}_{Bmin} on right), maximum migration rate (ω_M on left, \check{S}_M on right) and maximum curvature (bend apex: ω_{apex} on left). (a) Variation of ω_{Bmax} , ω_{ycmax} , ω_{Bmin} , ω_M and ω_{apex} , representing phase position downstream of the inflection point. Red dotted line indicates the bend geometric midpoint. (b) Variation of phase distances \check{S}_{Bmax} , \check{S}_{ycmax} , \check{S}_{Bmin} and \check{S}_M , normalized relative to the bend apex.

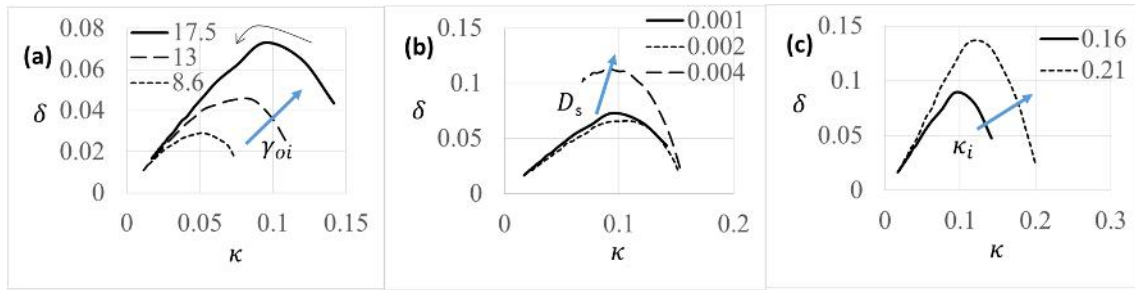


Figure 3.18. Sensitivity of time trajectories of width variation intensity u versus downchannel wavenumber $|\kappa$ to variation in input parameters. (a) Sensitivity to aspect ratio χ_{oi} (b) Sensitivity to dimensionless grain size D_s (c) Sensitivity to initial wavenumber $|\kappa_i$. The thick lines indicate the base run and the straight arrows indicate the direction of increase. Temporal evolution along each curve is from right to left as indicated by the curved arrow in (a)

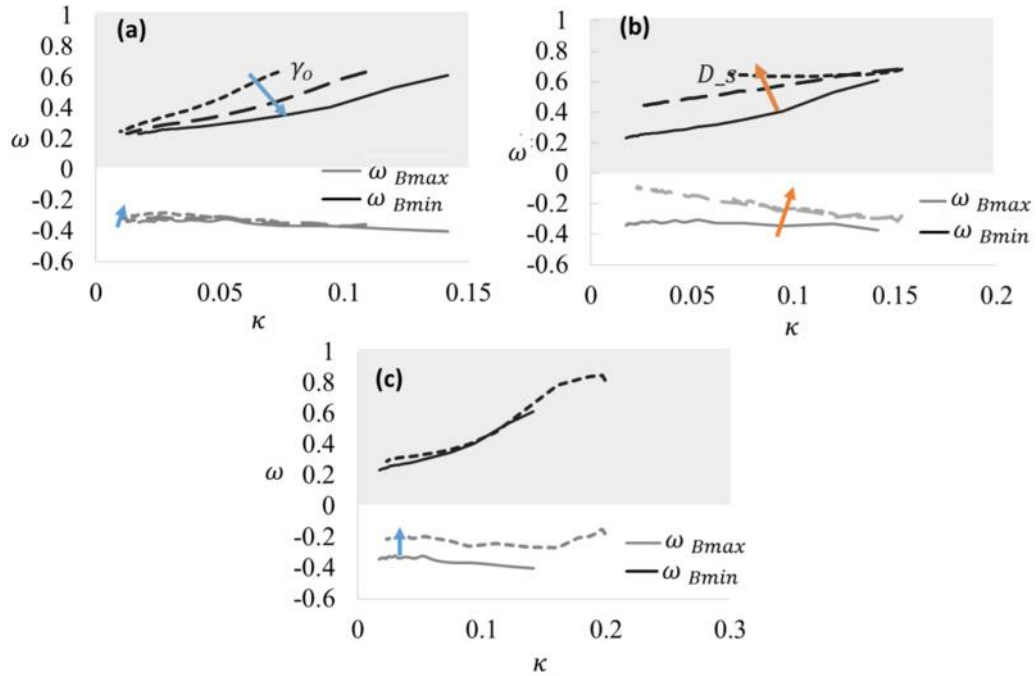


Figure 3.19. Sensitivity of time trajectories of normalized phase relative to bend apex \check{S}_{Bmax} \check{S}_{Bmin} , corresponding to maximum and minimum width versus downchannel wavenumber $|\iota|$, to variation in input parameters. (a) Sensitivity to aspect ratio χ_{oi} . (b) Sensitivity to dimensionless grain size D_s . (c) Sensitivity to initial wavenumber $|\iota|$. The thick lines indicate the base run and the straight arrows indicate the direction of increase. Temporal evolution along each curve is from right to left. The values of χ_{oi} , D_s and $|\iota|$ are the same as in figure 3.18.

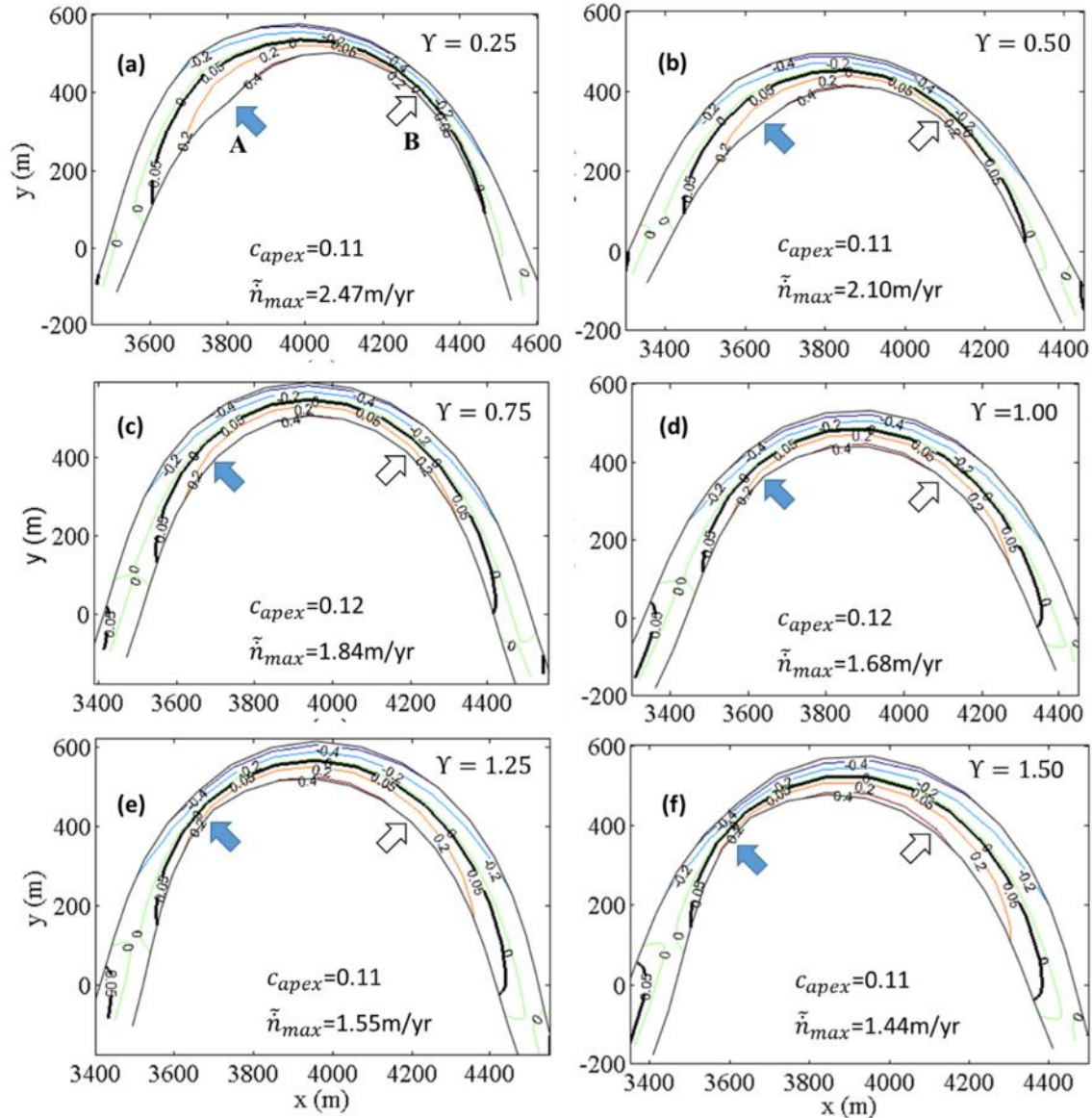


Figure 3.20. Plots of bed topography contours and bank lines illustrating sensitivity variation in the coefficient $\Upsilon = i'_{Eref} / i'_{veg}$. In the plots, i'_{Eref} is held constant at 5m/yr while i'_{veg} is reduced from (a) –(f), so yielding the increasing values of Υ . The bank lines correspond to the bounds of the bank region of figure 3.8. Each plots correspond to the time at which peak bend amplitude was reached. Direction of flow is from left to right in all cases. The filled and white arrows correspond to the location of maximum and minimum width for $\Upsilon=0.25$ respectively. Width deviation has been magnified by 5 for visualization.

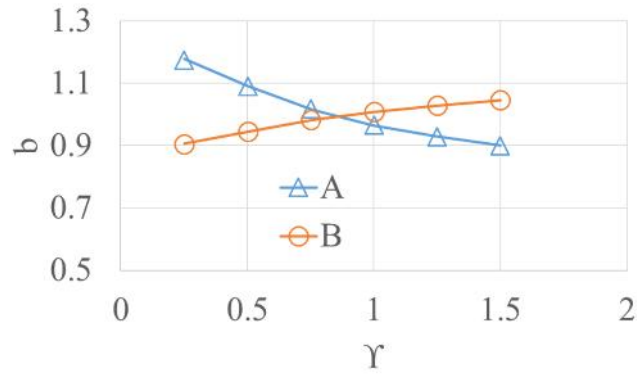


Figure 3.21. Dimensionless half width at a fixed point A upstream of the bend apex and a fixed point B downstream of the bend apex as a function of γ . The positions of these points are depicted in figure 3.20. The values for $\gamma = 0.25$ correspond to maximum width (A) and minimum width (B).

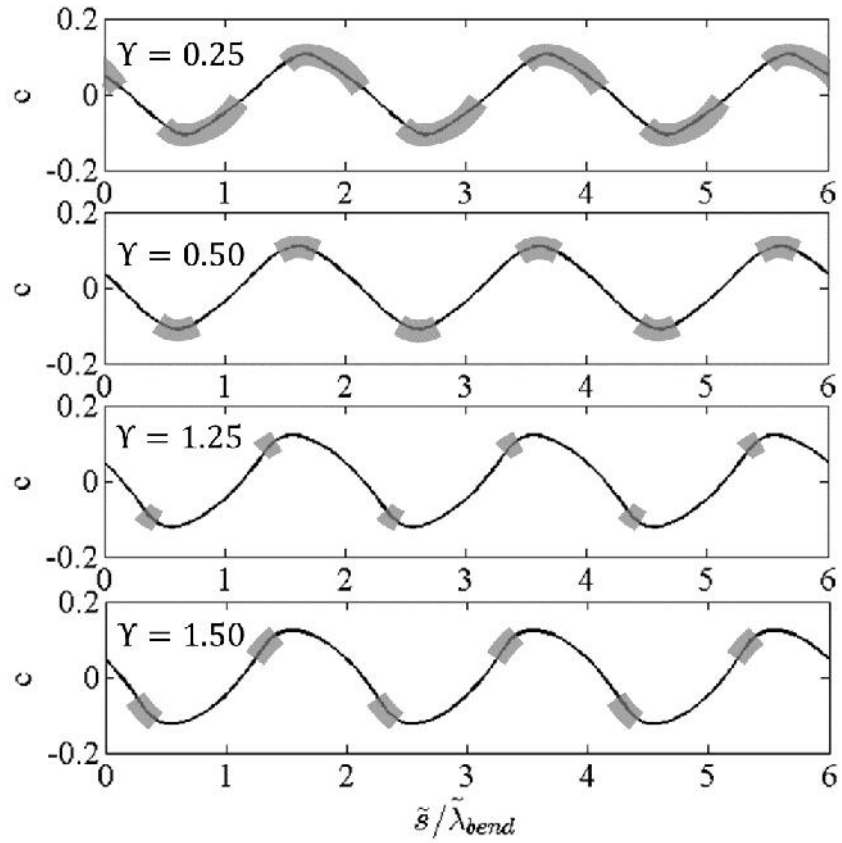


Figure 3.22. Plots showing centerline curvature versus normalized streamwise distance for the values $\gamma = 0.25, 0.5, 1.25$ and 1.50 . The run conditions correspond to those of figure 3.20. Zones of bank pull are marked with shaded regions; the absence of which implies bar push.

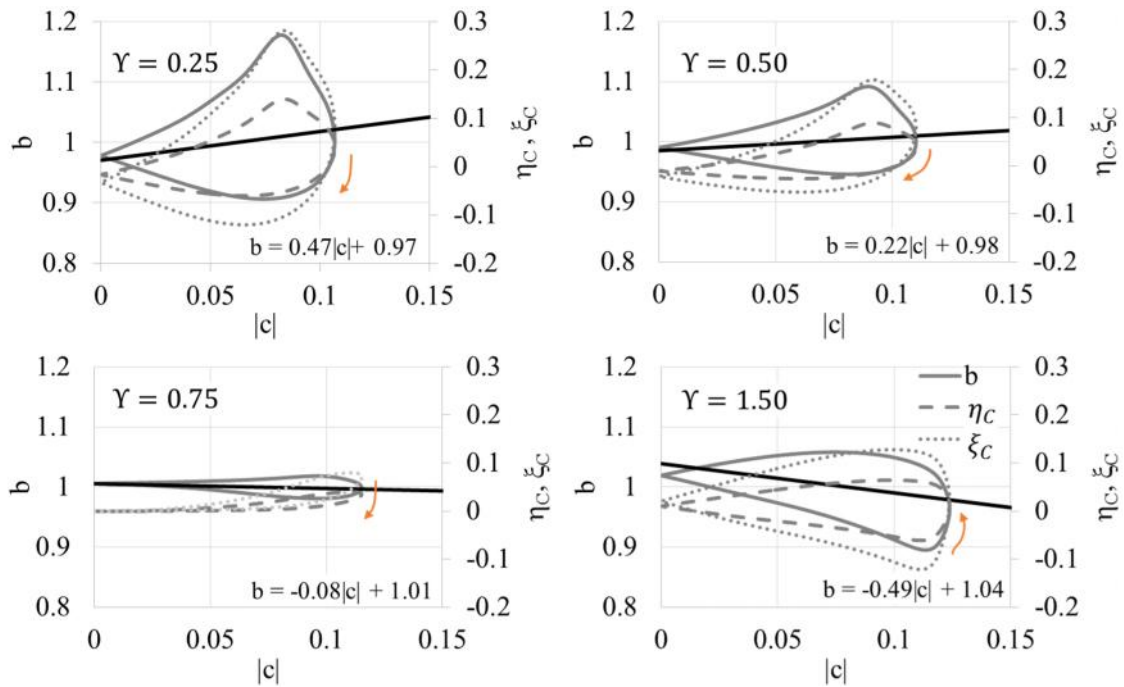


Figure 3.23. Loop curves along a meander bend at the time of maximum apex curvature for width b , deviatoric centerline bed elevation η_C and deviatoric centerline water surface elevation ξ_C as functions of the absolute value of curvature. Results for the four cases $\gamma = 0.25, 0.5, 0.75$ and 1.5 are shown; the base case corresponds to $\gamma = 0.5$. Straight lines indicate the linear regression fit for width and absolute curvature. Arrows indicate direction of trajectory.

Chapter 4

LONG TERM EVOLUTION OF MEANDERING RIVERS WITH WIDTH VARIATION

Abstract

Several numerical models of the long term evolution of meandering rivers have shown a tendency towards a statistical equilibrium achieved through repeated series of channel extension by migration and channel shortening by cutoff. This statistical steady state is often defined by a reach averaged channel wavelength/sinuosity time signal that oscillates about a characteristic mean value. This paper implements a model for meander migration that, for the first time, accounts for the spatio-temporal co-evolution of channel width and curvature and shows that channel width asymptotically achieves a mean value characterizing statistical equilibrium, via repeated series of channel narrowing during extension and widening during cutoff. The paper also explores the local effects of a cutoff, including local width adjustment, and shows both a downstream advection of the disturbance generated at the point of cutoff and a dispersal effect that propagates both upstream and downstream of that point.

4.1. Introduction

Long term meander evolution, herein defined as the evolution of a bend or a series of bends up to and beyond repeated cutoffs, has been a subject of interest over many years dating back to the early-mid 20th century (e.g. Fisk, 1947). The role of cutoffs in particular has been studied, from its role in limiting bend growth to its role in creating floodplain heterogeneity that affects bend

migration patterns (Gunalp and Rhoads, 2011). Cutoffs in nature can occur in the form of neck cutoffs, which result when two points of the river come into contact, or as chute cutoffs in which a new channel diversion is created across low floodplain deposits during floods (Lewis and Lewin, 1983; Gagliano and Howard, 1984; Howard, 1992; Constantine 2010; see Figure 4.1).

Numerous field observations have been useful in describing characteristic features in meandering systems such as the flow structure (e.g. Bridge and Jarvis, 1977; Dietrich and Whiting, 1989; Frothingham and Rhoads, 2003), the complex nature of river planform geometry (e.g. Brice, 1974; Hey, 1976; Hooke, 1995), the nonlinear relationship between channel migration and curvature (e.g. Hickin, 1975 and Hickin and Nanson, 1984, Furbish, 1988), and cut-off dynamics (e.g., Mosley, 1975; Gagliano and Howard, 1984; Hooke, 1995, Gay et al., 1998; Zinger et al., 2011). In numerical modelling, great strides have been made towards understanding long term meander dynamics including the nature and role of cutoffs. Due to the limited understanding of the physical controls governing chute cutoffs, only neck cutoffs are considered in most numerical modelling.

Owing to its simplicity, most long term evolution models capture in-channel flow and bed morphodynamics using linearized “2.5D” flow and bed morphodynamics models (e.g. Ikeda et al., 1981; Parker et al., 1983; Beck et al., 1984; Howard, 1984, 1992, 1996; Stølum, 1996; Sun et al., 1996, 2001b; Camporeale et al., 2005, 2008; Frascati and Lanzoni, 2009; and Motta et al., 2012a,b). Camporeale et al. (2007) classifies the various 2.5D flow models in a hierarchy corresponding to the level of detail they provide.

While flow models may vary, almost all models that capture long term meander dynamics link channel hydrodynamics to bank migration have used a HIPS-type formulation (Hasegawa-Ikeda-Parker-Sawai; e.g. Parker et al, 2011), in which channel width is a prescribed constant and local lateral channel migration is linearly related to near-bank velocity as:

$$b' = E u_b \quad (4.1)$$

where E is a dimensionless erodibility constant and u_b denotes the near bank streamwise velocity deviation from the mean velocity U_o . As an example, for the simplified linear IPS model (Ikeda et al, 1981), this near bank velocity deviation is expressed by the solution:

$$u_b = u_b(0) e^{-\frac{C_f}{H_o} s} + e^{-\frac{C_f}{H_o} s} \int_0^s e^{\frac{C_f}{H_o} s'} \left[C_f \frac{b_o U_o}{H_o} (F_o^2 + A - 1) C - U_o b_o \frac{\partial C}{\partial s} \right] ds' \quad (4.2)$$

where s is the streamwise coordinate, A is the transverse bed slope, C is the local channel centerline curvature, C_f is a constant friction coefficient and b_o , H_o and F_o are the reach averaged channel width, flow depth and Froude number respectively.

These HIPS-type models have been used show, among other things, a) the tendency of a cutoff to trigger a cluster of cutoffs in space and time (e.g. Stølum, 1996), b) the wave-like downchannel propagation of disturbance generated by cutoffs, c) the role of cutoffs in generating flow nonlinearity, and d) their role in reducing geometric nonlinearity by removing the most mature asymmetric bends (e.g. Camporeale et al., 2005, 2008).

A prominent result from numerical modeling is the tendency of a river to achieve a statistical steady state of geometrical characteristics through a balance between channel elongation and cutoff. The work of Howard (1984) was able to show this tendency in the absence of any

external forcings (e.g. discharge fluctuations, vegetation effects, geological and anthropic effects). These findings were confirmed by Stølum (1996) and Camporeale et al. (2005, 2008). Stølum (1996) explained this tendency in terms of self-organization, a concept which originates from the work of Bak et al. (1987). Stolum argued that, for an unconstrained meander, both the processes of channel elongation and cut-off tend to self-organize channel sinuosity into a steady state around a mean value of π (the sinuosity of a circle).

In all of the above contributions, river width is a constant, user-specified input parameter determined externally to the migration process. The question of how this width is determined, however, remains unaddressed. Recent work by Parker et al. (2011) proposes a new physically-based model framework for meander migration in which channel width is determined locally in terms of the migration rate of each bank, which may undergo erosion or deposition. In this model framework, rather than using the HIPS formulation defined in (4.1) to estimate local centerline migration rates, banks are migrated separately using submodels that estimate bank erosion or deposition depending on local conditions near the bank. The model proposed by Parker et al. (2011) has been developed and implemented for short-term migration simulations in Eke et al (2013a,b; Chapters 2 and 3).

Field observations over geomorphic time suggest that although many rivers show systematic patterns of spatial variation in width, they tend to maintain a fairly constant reach-averaged channel width as they migrate (e.g. Lagasse et al., 2004). In this paper, we address the question of how a river is able to achieve this. We postulate that just as a river is able to maintain a statistical equilibrium in sinuosity/wavelength through cycles of channel elongation and cut-offs, a river is similarly able to maintain a statistical equilibrium width through cycles of channel

narrowing during elongation and widening immediately subsequent to cutoffs. We also perform an analysis similar to the work of Sun et al. (2001b) and Camporeale (2008), which focuses on the localized effect of a cutoff. Here, in addition to the localized effect on bed topography and curvature, we also show a localized effect on width, and the streamwise dispersion of this effect over time. We incorporate width evolution by implementing the framework proposed by Parker et al. (2011) and implemented by Eke et al. (submitted a,b; Chapter 2 and 3). A brief description of the formulation is described below.

4.2 River migration modelling incorporating river width adjustment

The recent work of Parker et al. (2011) and Eke et al. (submitted a,b; Chapters 2 and 3) present a new model where the constraint of a constant channel width is removed, so that width is allowed to vary locally as the channel migrates. As shown in the model cross-section depicted in figure 4.2, the model assumes that each channel bank j has a constant slope denoted as $S_{s,j}$, and a composite structure consisting of a non-cohesive sediment layer of thickness $H_{b,j}$, topped by a cohesive layer of thickness, $H_{c,j}$. The latter layer, when eroded, generates slump blocks.

The model replaces the equation of sediment continuity on the bank regions with integral “shock” formulations such that lateral rate of migration of the toe of each bank j i.e. \dot{n}_j is expressed as:

$$\dot{n}_j = \frac{\partial n_{t,j}}{\partial t} \cong \frac{-q_{nb,j} (1 + n_{t,j} C)}{H_{b,j} (1 + \bar{n}_j C) (1 - p_{b,j})} + \frac{1}{S_{s,j}} \frac{\partial y}{\partial t} \Big|_{n=n_{t,j}} \quad (4.3)$$

where t denotes time, n denotes the transverse coordinate defined to be increasing in the direction of the left bank, y denotes channel bed elevation, $n_{t,j}$ denotes the transverse position at the toe of the bank j which is equal to $+b$ at the left bank and $-b$ at the right bank where b is the local channel half-width, \bar{n}_j the transverse position of the center of the bank region j , and $p_{b,j}$ denotes the porosity of the non-cohesive bank material. Finally, $q_{nb,j}$ denotes the transverse bedload transport rate at the toe of the bank. Thus the total lateral migration of the bank toe is a sum of migration due to sediment transport to or from the channel and migration due to near bank aggradation or degradation. In defining closures for the shock formulations, the first term in (4.3) is treated differently depending on whether a bank is eroding or depositing. Thus, for an eroding bank, the lateral migration of the bank toe \dot{n}_E is given as

$$\dot{n}_E \cong 'E + \frac{1}{S_{s,j}} \frac{\partial y}{\partial t} \Big|_{n=n_{t,j}} \quad (4.4)$$

while for a depositing bank,

$$\dot{n}_D \cong 'D + \frac{1}{S_{s,j}} \frac{\partial y}{\partial t} \Big|_{n=n_{t,j}} \quad (4.5)$$

Details on how the erosion and deposition terms $'E$ and $'D$ are modeled are provided in Eke et al. (submitted, Chapter 2). In summary, the erosion term is modelled as bank retreat resulting from non-cohesive sediment transport along a sloping bank $'_{non,E}$ which is slowed down by an armoring coefficient $K_{armor} \ll 1$. Thus

$$'E = K_{armor} I_f '_{non,E} \quad (4.6)$$

The flood intermittency factor I_f represents the portion of time when the river is morphodynamically active. The armoring coefficient K_{armor} may, in principle, represent any form of natural armoring such as tree stumps and roots but in this formulation is modelled considering slump block armoring. The closure for K_{armor} is such that it is a function of a near bank Shields number ratio r i.e.

$$K_{armor} \cong \frac{\epsilon_{Eref}}{I_{f,ref} \left| \epsilon_{non,E} \right|} (r - 1) \quad (4.7)$$

where ϵ_{Eref} and $I_{f,ref}$ are the reference erosion and intermittency factor, respectively, related to slump block decay (Eke et al, submitted; Chapter 2) and r is the ratio of the near bank streamwise Shields number τ_{nb}^* to a formative Shields number τ_{form}^* i.e.

$$r = \frac{\tau_{nb}^*}{\tau_{form}^*} \quad (4.8)$$

Thus for higher near-bank Shields number, the armoring coefficient increases toward unity, and the bank erosion rate correspondingly increases.

For the period of time the flow is not in flood, i.e. frequency $(1 - I_f)$, the deposition term ϵ_D is modelled as:

$$\epsilon_D = \epsilon_{veg} (1 - I_f)(1 - r) \quad (4.9)$$

where r_{veg} is a reference vegetation encroachment rate. Here increasing r characterizes the slowdown of the vegetation encroachment, as the near bank shear stress during floods τ_{nb}^* increases. In this way, higher near-bank shear stress during floods suppresses the deposition rate below the value that would prevail in the absence of floods.

Both models are tied together by a time-varying formative Shields number which is modelled as a function of reach-averaged channel slope. The functional relationship is based on a regression fit to field data (Li et al., submitted), and is such that

$$\tau_{form}^* = f(S_o^{0.53}) \quad (4.10)$$

where S_o is the reach averaged channel slope.

The model is also formulated such that either or both banks may erode or deposit depending on the ratio of the near bank Shields number to the formative Shields number r . For $r > 1$ the bank erodes, for $r < 1$, the bank deposits and for $r = 1$, the bank neither erodes nor deposits. The rate of change of local channel half-width \dot{b} is, thus, given as follows:

$$\dot{b} = \frac{\partial b}{\partial t} = \frac{1}{2}(\dot{n}_{LB} - \dot{n}_{RB}) \quad (4.11)$$

where LB and RB denote left and right bank respectively.

To obtain near bank Shields stresses, the above bank formulations are linked to a nonlinear morphodynamic model. According to the classification of Camporeale et al. (2007), the in-channel model adopted in this work falls under the JP_{4N} (i.e. Johannesson and Parker type, fourth order,

nonlinear model) category in that it is fully nonlinear, adopts a uniform eddy viscosity and constant friction coefficient, captures the interaction between flow and sediment dynamics and incorporates full coupling between the longitudinal and transverse flow momentum. The work of Camporeale et al. (2007) outlines the iterative scheme of the JP_{4N}, model which is an expansion of the previous nonlinear models of Smith and McLean (1984) and Imran et al. (1999). The model used here represents a modified version of the one presented in Camporeale et al. (2007), the modification so as to accommodate width variation; the corresponding form for specified, constant width is given in Yi (2006).

Near bank Shields stresses are functions of the near bank velocity vector u_b . In this nonlinear model, this near bank velocity vector can be expressed in contrast to the IPS model as:

$$u_b = u_b(0)e^{-\frac{C_f}{H_o}s} + e^{-\frac{C_f}{H_o}s} \int_0^s e^{\frac{C_f}{H_o}s} \left[C_f \frac{b_o U_o}{H_o} (F_o^2 + A - 1) C - U_o b_o \frac{\partial C}{\partial s} \right] ds + R \quad (4.12)$$

where R is a residual term, including all nonlinear residuals, obtained via numerical iteration. Details of model formulation are presented in Eke et al (submitted, Chapter 3)

4.3 Long term meander evolution incorporating channel width adjustment

Long term simulations were carried out starting from an initial straight channel of uniform width with a random distribution of lateral displacement along the channel centerline to trigger instability. The model input parameters are loosely based on the Pembina River in Alberta, Canada; with a bankfull discharge of 405m³/s, intermittency factors $I_f = I_{f,ref} = 0.2$, valley slope of 0.00049 and a grainsize of 2mm. To model bank migration, bank side slope $S_{s,j} = 1.5$ is assumed

and an average bank height of 3.75m is adopted, a third of which is assumed to be cohesive material. The vegetation encroachment rate ϵ_{veg} is taken to be 14.9 m/yr (about 15% of an estimated channel straight channel bankfull width of 99m) and the reference erosion rate ϵ_{Eref} based on estimates of slump block characteristics is 3.75 m/yr. More detailed justification of these numbers is presented in Eke et al. (submitted b; Chapter 3).

Figure 4.3 shows the varied stages of meander evolution from amplification of initial perturbations to the development of highly tortuous and complex meanders. The channel becomes narrower over time, with a 25% reduction in width from the initial width of 99 m to an approximate final width of 74 m. This corresponds to a centerline bed slope that declines with increasing sinuosity, so driving channel narrowing (Eke et al., submitted b; Chapter 3). In addition to temporal width adjustment, the development of spatial width oscillations is evident, particularly during the initial stages of meander growth. This spatial width oscillation becomes less pronounced as the river becomes more tortuous.

Focusing on the temporal evolution of mean channel characteristics, Figure 4.4 shows plots of the time evolution of mean absolute curvature, mean channel wavelength, sinuosity and mean channel half-width (the overbar refers to the spatial averaging). The sinuosity here refers to the ratio of the river length to the linear distance between its endpoints, and the channel wavelength is assumed to be equal to twice the along channel distance between the zero crossings of the curvature. In line with the results of Howard (1984), Stolum (1996) and Camporeale et al (2005, 2008), the model arrives at a statistical steady state purely by balance between the processes of channel elongation and cutoff. One key finding in this work is evidence for the role of cutoffs in

maintaining a statistically constant width over time as the river migrates. In Figure 4.4(d), width decreases during early stages of meander development, before the occurrence of cutoffs. With each cutoff, the mean width increases as sinuosity reduces. Over multiple cutoffs, channel width arrives at a statistically steady state, just as with other channel characteristics.

Figure 4.5 compares the above model simulations with simulations carried out with the IPS model described in equations (4.1) and (4.2). A constant half-width equal to 37m is imposed and an erodibility coefficient of $E = 3 \times 10^{-7}$ is used, the latter chosen to give similar migration rates to the above simulation with varying, self-formed width. Camporeale et al. (2005) show that the value of the erodibility coefficient E only affects the timescale of the meandering process. Thus, the differences in spatial characteristics shown in figure 4.5 stem largely from the differences in flow modeling (i.e. IPS versus JP_{4N} with width variation).

A comparison of mean channel characteristics of existing linear models has shown the IPS model to be comparable to other more advanced linear models in its prediction of long term characteristics (Camporeale et al, 2005). Camporeale et al. (2005) refer to three phases in the river evolution process: an initial phase before the occurrence of cutoffs where the differences between models are significant; a middle phase after cutoffs begin to appear; and a third phase where the differences between flow models tend to phase out, and a statistical equilibrium is reached, at which the overall behavior tends to be relatively independent of the morphodynamic model adopted.

The results shown in figure 4.5, appear to be in line with the above observations. The implication of this is that the residual term R in (4.12), which captures, in addition to the full

coupling between flow and sediment transport, flow non-linearity induced by curvature and width variation, may not be essential to the prediction of the statistics of long term dynamics. Thus, while the linearized models may fall short in fully representing short term meander evolution, they may nevertheless give an adequate description of long-term evolution trends.

The work of Eke et al. (submitted b, Chapter 3) demonstrates the presence of spatially varying patterns of local width variation in short-term simulations. i.e. simulations up to cutoff. It is also shown therein that the correlation between width and curvature can vary from a positive correlation, such that the channel is wider just upstream of the bend apex as depicted here in the initial stages (figure 4.3), to a negative one such the channel is wider further downstream of the apex and closer to the inflection points. They show that this correlation shift is largely affected by a dimensionless input parameter Υ which represents the ratio between the reference erosion rate $'_{Eref}$ and the reference vegetation encroachment rate $'_{veg}$. Lower values of Υ show a more positive correlation and higher values of Υ , a more negative correlation.

Figure 4.6 shows scatter plots of dimensionless local channel half-width b^* ($= b/b_o$) and dimensionless absolute curvature C^* ($= C \times b_o$) over time. The value of Υ in this simulation is 0.25. Within the scatter, we observe the width-curvature loops described in Eke et al. (submitted b; Chapter 3). More specifically, Figure 6 demonstrates that at the initial stages prior to cutoff, there is a general trend of positive correlation of width and absolute curvature; meaning that the channel width tends to be greatest where curvature is highest. Over time as the channel evolves, we observe that magnitude of width oscillations diminishes and we eventually get the opposite case, where width and curvature are negatively correlated. This result is significant in so far as it

suggests that cutoffs and resulting meander complexity have an additional role to play in determining the evolution of patterns of local channel width variation over time. For the same ratio Y , we can obtain different width-curvature configurations over time.

As to the nature of width-curvature correlation at equilibrium, we note here that similar simulations were carried using different initial conditions. The general trend at statistical equilibrium was one with diminished width oscillations, with width and curvature are negatively correlated (i.e. width is highest close to the inflection points). While further research would need to be done to make a direct statement towards the general tendency at statistical equilibrium, the results show correspondence in line with the analytical solution of Luchi et al. (2012) for the equilibrium river. In their analysis on periodic bends they show that an equilibrium river tends towards a configuration that is wider near the crossings. In this work we show a similar tendency for highly complex river systems.

4.4 Width adjustment in response to a cut-off

To illustrate channel width adjustment in response to a cut-off, we consider a bend at incipient cutoff. The initial condition is a planform just at neck cutoff, as shown in figure 4.7 by the thin continuous line. The snapshot therein represents the channel configuration at time 2304 years of the simulation of figure 4.3. The location O indicates the point of incipient cutoff, the thick continuous line is the channel immediately following the cut-off and the thick dashed line is the channel 500 years later. Similar to the analysis of Camporeale et al (2008), we use the case in which cutoff is disabled as a reference against which to study the effect of cutoff. In this artificial reference case, the centerline is allowed to overlap without cutoff, as shown by the thin dashed

line in figure 4.7. The assumption in this analysis is that by comparing evolution patterns with and without cutoffs, we can estimate the extent of influence of the perturbation generated by cutoff. In figure 4.7, the downstream end of the zone of influence of the cutoff disturbance is indicated by the point X'.

Figures 4.8, 4.9 and 4.10 show downstream variation of channel centerline curvature, local channel half-width and centerline bed slope, respectively, in the channel segment near the vicinity of a cut-off. The sequential images represent times just after cut-off (about 2 yrs), and 100 years, 300 years and 500 years after cut-off. In the figures, the point O indicates the point of incipient cutoff, the thin line A-A' denotes the artificial channel in which cutoff is disabled, the thick line A-B' denotes the channel with cutoff and the region C-C' denotes the reach of the artificial channel that was eliminated by cut-off. The point demarcating the upstream end of the zone of influence X is determined by comparing the region A-C of the channels with and without cutoff and the downstream zone of influence X' is determined by comparing reach C'-A' of the channel without cutoff to reach C-B' of the channel with cutoff.

The figures show that cutoff generates a wave-like disturbance that that is advected downstream with the channel, eventually being damped out. The peak of the “disturbance wave” is at point O, which is the location of incipient cut-off. As the cutoff-induced disturbance migrates downstream, it also disperses both upstream and downstream, creating an increasing zone of influence bounded by the points X and X' in the figures. This same behavior is apparent in the evolution of the centerline curvature C and centerline slope S_c , as shown in figures 4.8 and 4.9 respectively. The disturbance generated by cut-off is seen as a sharp spike in curvature and slope, denoted by point O, the magnitude of which diminishes over time as it translates downstream. In

the case presented in figures 4.8 and 4.9, the dispersion of the zone of influence appears to be biased toward the upstream side of the point of incipient cutoff.

Figure 4.10 shows the downstream variation of the channel half width b . The figure shows a mean increase in channel width in the times following cutoff, in addition to the noise generated at the point of cutoff. As with curvature and slope, the noise propagates downstream, accompanied by dispersion such that its effect is felt both upstream and downstream of the origin of the disturbance at point O, as well as gradual damping in time.

4.5 Conclusions

Through long term simulations accounting for channel width adjustment via differential bank migration, we are able to show statistical trends towards asymptotically constant reach-averaged channel width, maintained via a balance between channel narrowing during channel elongation and widening during cutoff. Corresponding asymptotic states of statistical equilibrium are observed for the reach-averaged absolute value of centerline curvature, reach-averaged wavelength and channel sinuosity.

For the case studied here, local channel width correlates positively with the absolute value of local centerline curvature up to cutoff. That is, points of higher centerline curvature tend to be wider. After multiple cutoffs have occurred, however, the correlation becomes negative.

We compare our model, which incorporates fully nonlinear bed morphodynamics and self-formed channel width, with a corresponding IPS (e.g. Ikeda et al., 1981) implementation, which uses simplified linear bed morphodynamics and specified channel width. While the two models

show notable difference in details, especially before the first cutoff has occurred, the reach-averaged equilibrium state achieved after many cutoffs appears to be quite similar.

Analysis of the evolution of the channel in the vicinity of one of the cutoffs that evolved in our simulation allows characterization of channel response to cutoff. The perturbation generated by cutoff both migrates downstream and disperses both upstream and downstream, but is eventually damped out. This behavior is reflected in the evolution of local width, the absolute value of local centerline curvature and centerline bed slope.

Our migration model implemented represents a first step towards understanding channel width selection in natural meandering rivers, both at early stages of the evolution of sinuosity and after numerous cutoffs. The present model formulation with user-specified constant bank properties but self-evolving width is useful to isolate width-curvature dynamics. It does not, however, represent the complete picture of long-term dynamics. A more complete bank migration model should incorporate feedback between the channel and its floodplain. As a river migrates back and forth, it builds its floodplain via processes of overbank sedimentation and point-bar deposition; creating a heterogeneous sedimentary environment and heterogeneous bank properties that ultimately affect the river migration pattern. Thus bank height, bank slope, cohesive layer thickness and even slump block characteristics should vary in time as the river migrates. Coupling the present model to a model of floodplain evolution represents a goal for future research.

Acknowledgement

This research represents a contribution of the National Center for Earth-surface Dynamics, a Science and Technology Center funded by the US National Science Foundation (agreement EAR-

0120914). Additional support was provided by the National Science Foundation through agreement EAR-1124482.

Figures

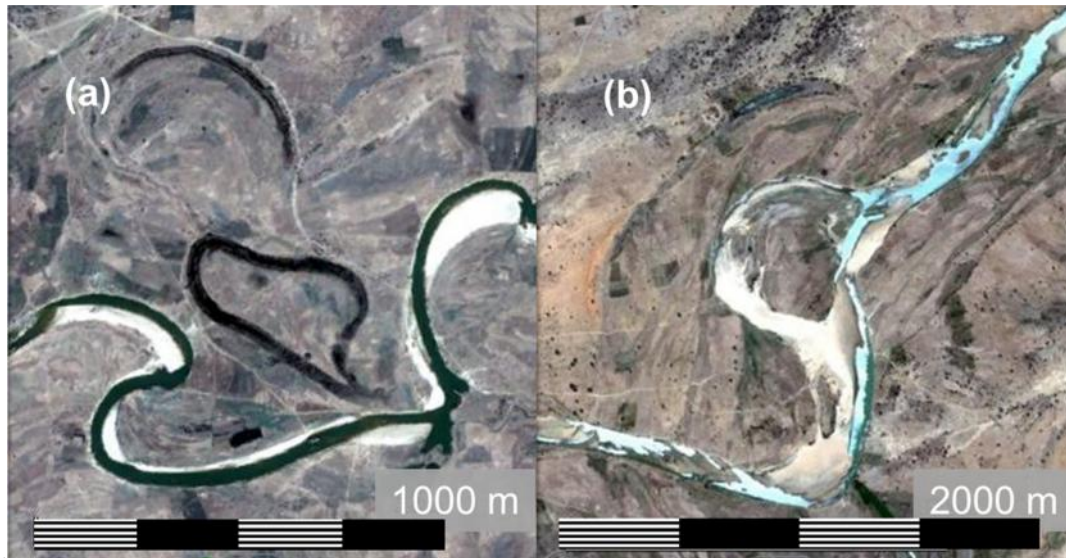


Figure 4.1: Image showing cutoffs (a) Neck Cutoff on the Hadejia River, Yobe, Nigeria (b) Chute Cutoff on the Jama'are River, Bauchi, Nigeria. Flow is from left to right in both cases.

Images are from Google Earth.

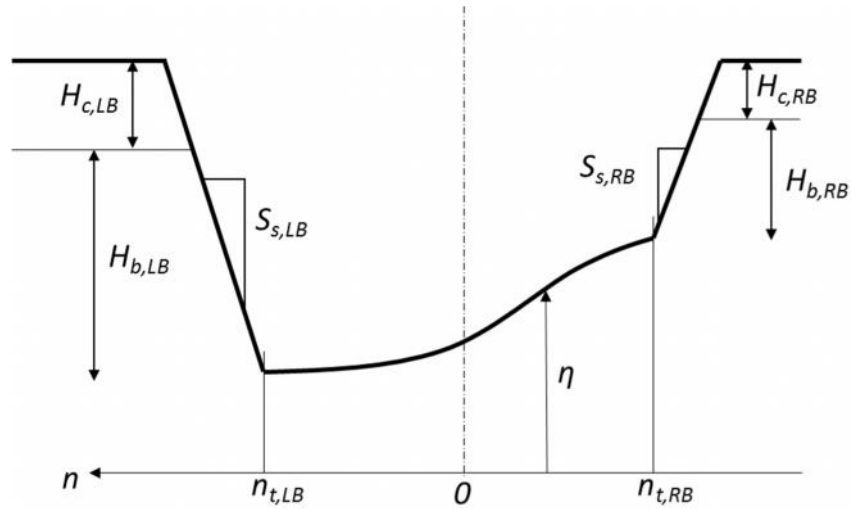


Figure 4.2: Definition sketch of model channel cross-section. The transverse coordinate n is defined such that it is increasing towards the left bank. Subscripts “LB” and “RB” indicate left bank and right bank respectively. The banks are assumed to have a constant transverse slope S_s , and a cohesive layer of thickness H_c overlying a non-cohesive layer of thickness H_b . Also, η denotes the bed elevation and the subscript “t” denotes the bank toe.

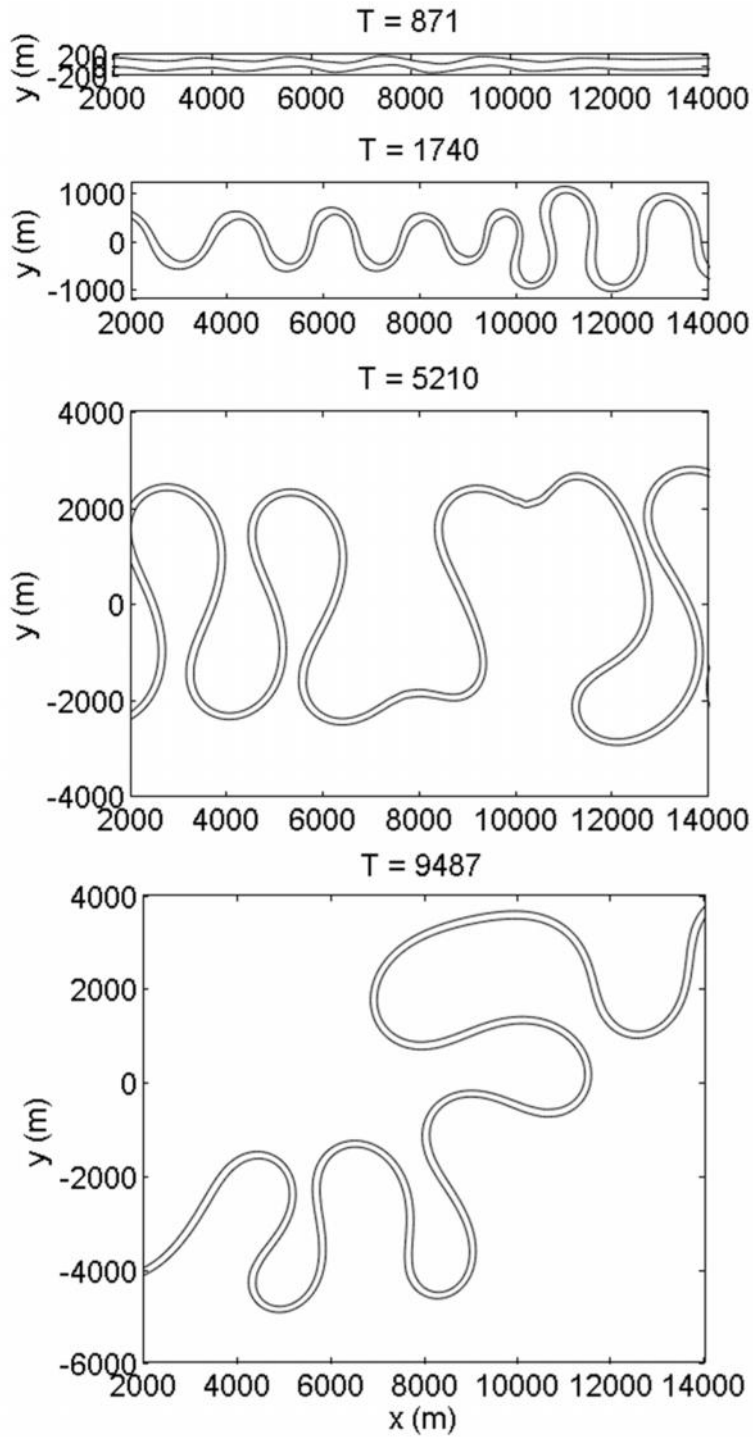


Figure 4.3: Temporal evolution of channel planform. The lines indicate the location of the bank toe i.e $n = \pm b$ where b is the local channel half-width. Flow is from left to right.

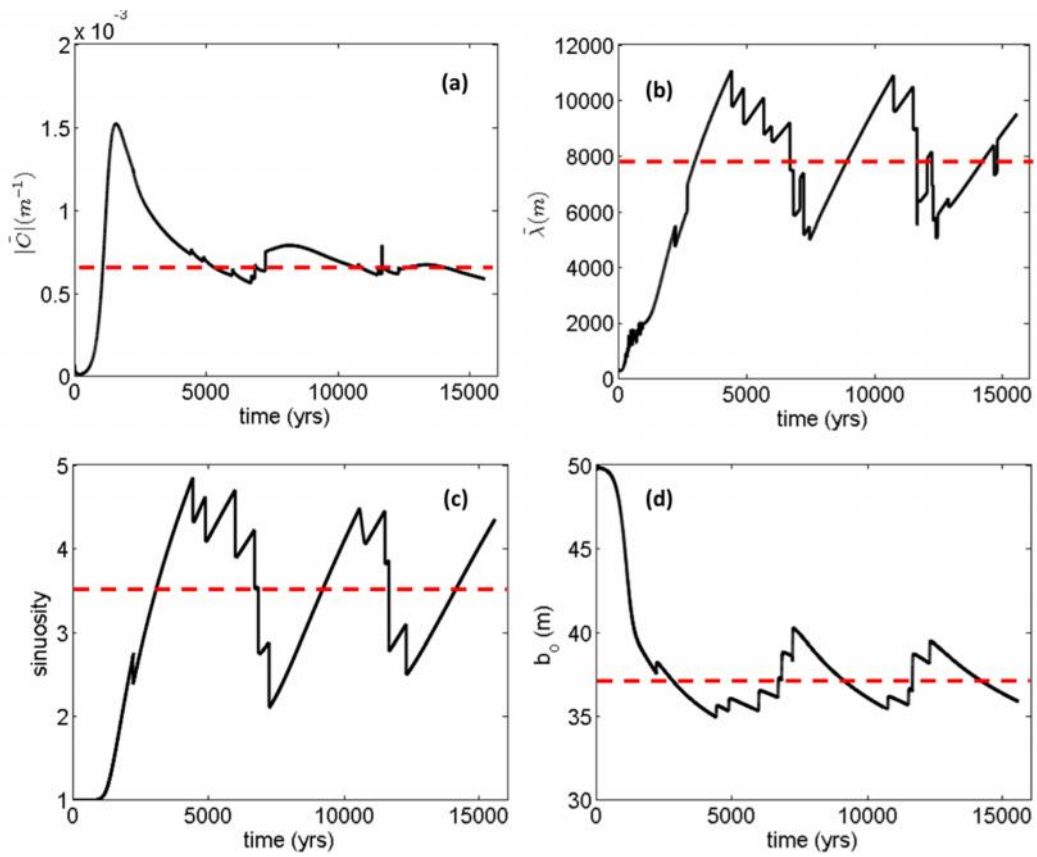


Figure 4.4: Temporal evolution of geometric characteristics. Time series of (a) mean absolute curvature (b) mean wavelength (c) sinuosity (d) mean channel half-width. The dashed lines highlight the stationary part of the time series.

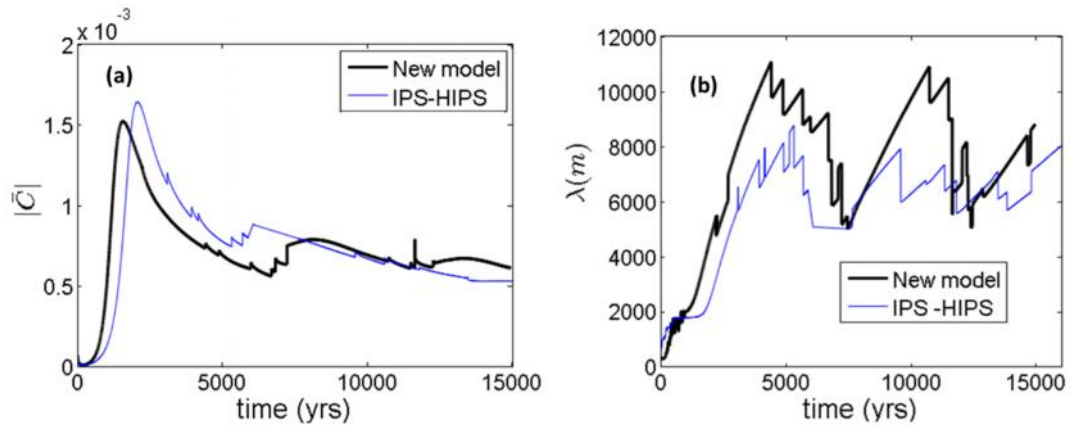


Figure 4.5: Comparing geometric characteristics of IPS-HIPS model with present model. Time series of (a) mean absolute curvature (b) mean wavelength. The thick lines represent new model results from (4.3) and (4.12). The thin lines results from the IPS-HIPS model of (4.1) and (4.2)

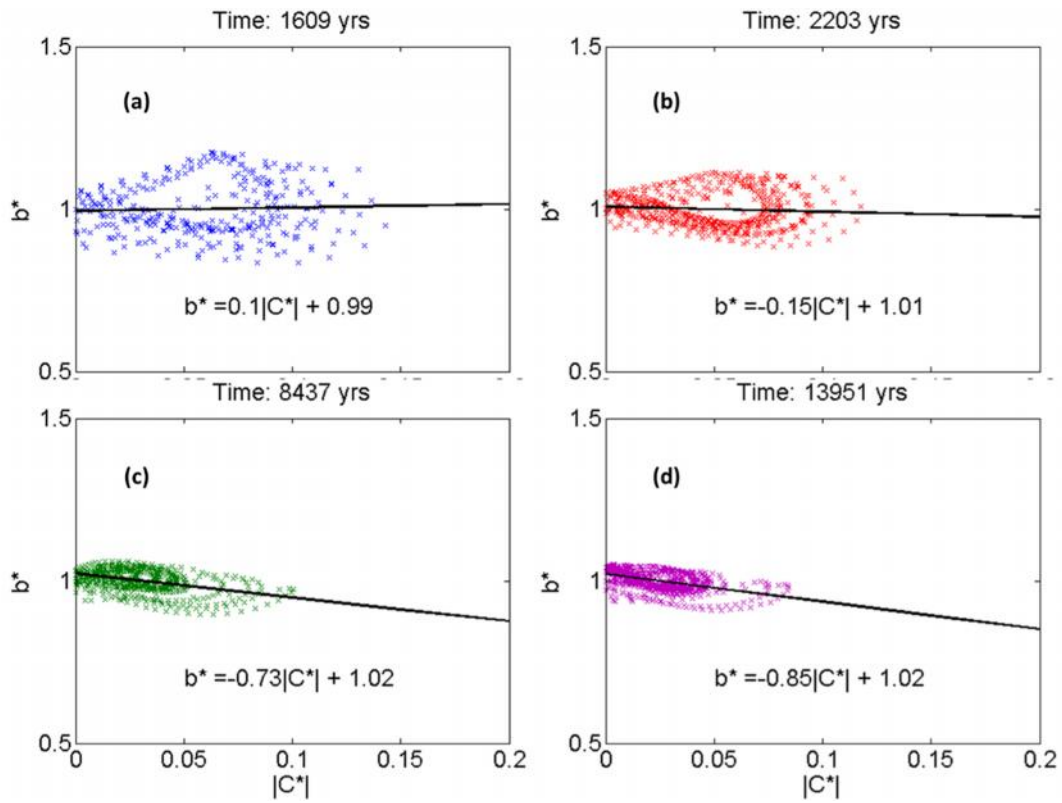


Figure 4.6: Dimensionless half-width b^* versus absolute dimensionless centerline curvature C^* over time. The straight line is a linear fit to the points.

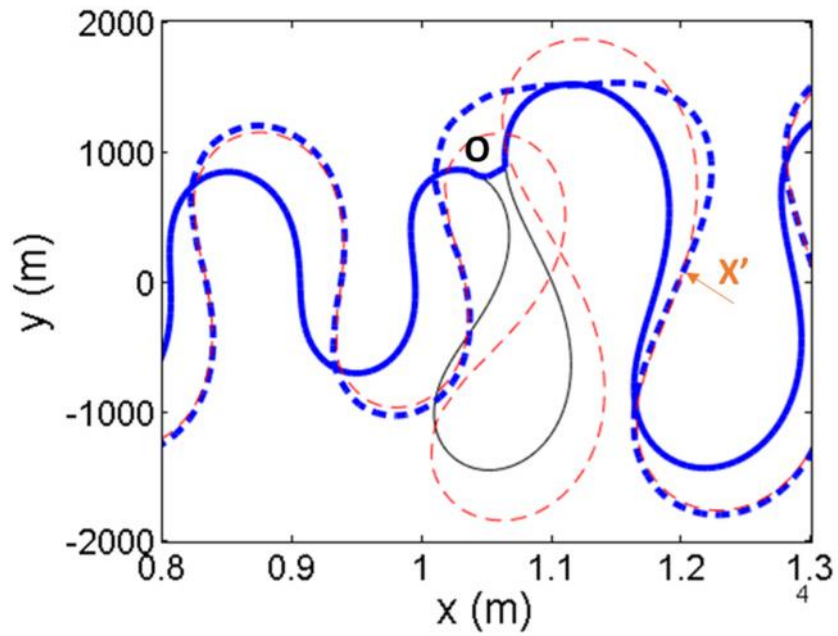


Figure 4.7: Centerline evolution following a cut-off. The thin continuous line indicates the initial configuration of incipient cutoff, the thick continuous line indicates the channel just after cutoff, the thick dashed line is the channel 500 years subsequently, and the thin dashed line is the channel 500 years subsequently, but without cutoff (so that the centerline overlaps). Flow is from left to right

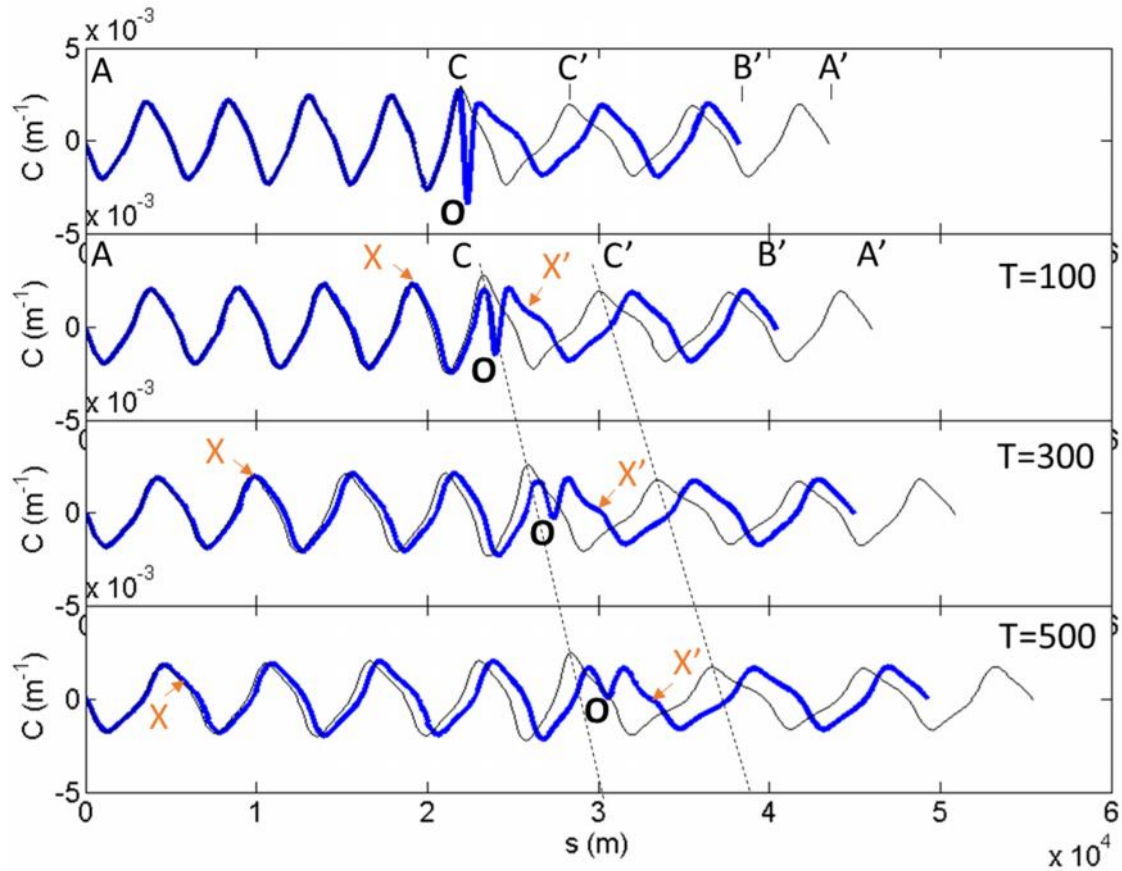


Figure 4.8: Evolution of curvature disturbance generated by cutoff. The thin continuous line indicates the centerline curvature of the channel without cutoff, and the thick continuous line indicates the channel with cutoff. The location of incipient cutoff is denoted by point O . The dashed subvertical lines delineate the region of the channel without cutoff (i.e. the thin continuous line) that would have been removed by cutoff. To determine the zone of influence X' the thick line C - B' must be compared with the thin line $C'A'$.

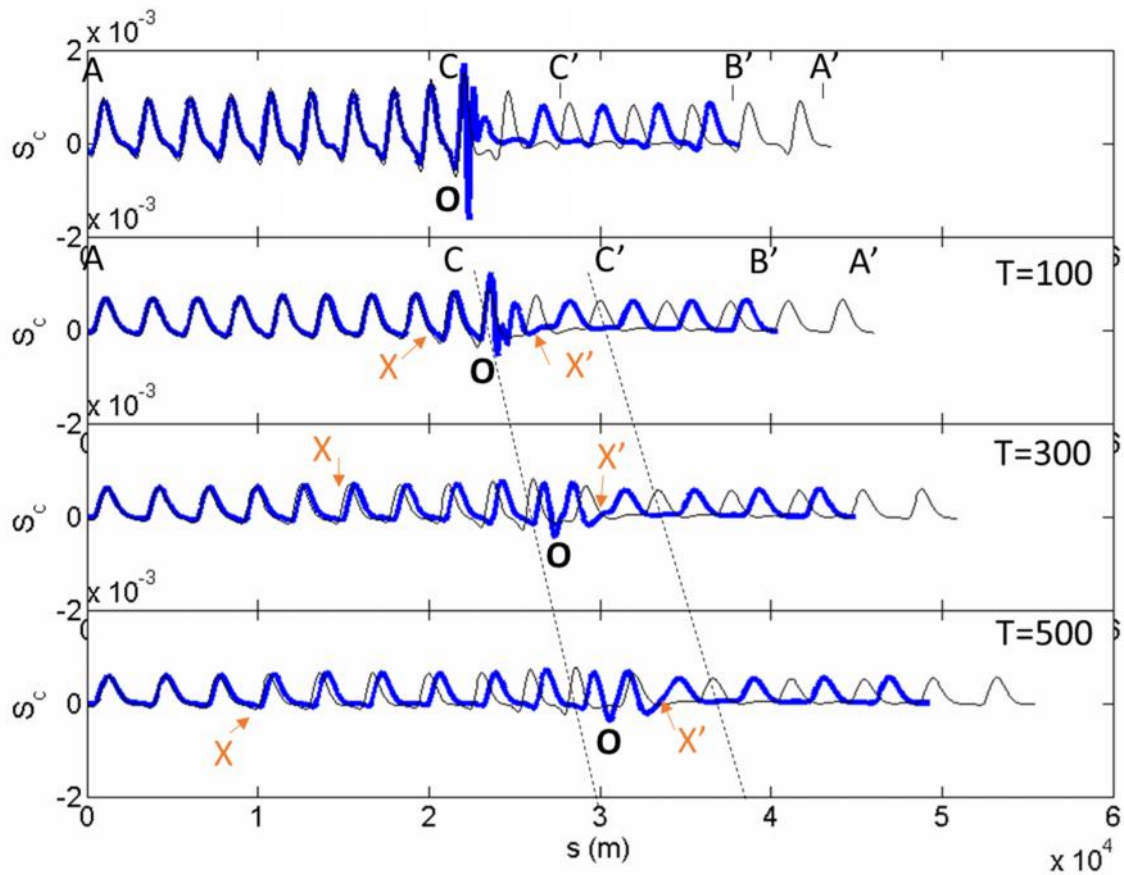


Figure 4.9: Evolution of centerline slope disturbance generated by cutoff. The thin continuous line indicates the centerline slope of the channel without cutoff and the thick continuous line indicates the channel with cutoff. The location of incipient cutoff is denoted by point O. The dashed subvertical lines delineate the region of the channel without cutoff (i.e. the thin continuous line) that would have been removed by cutoff. To determine the zone of influence X' the thick line C-B' must be compared with the thin line C'A'

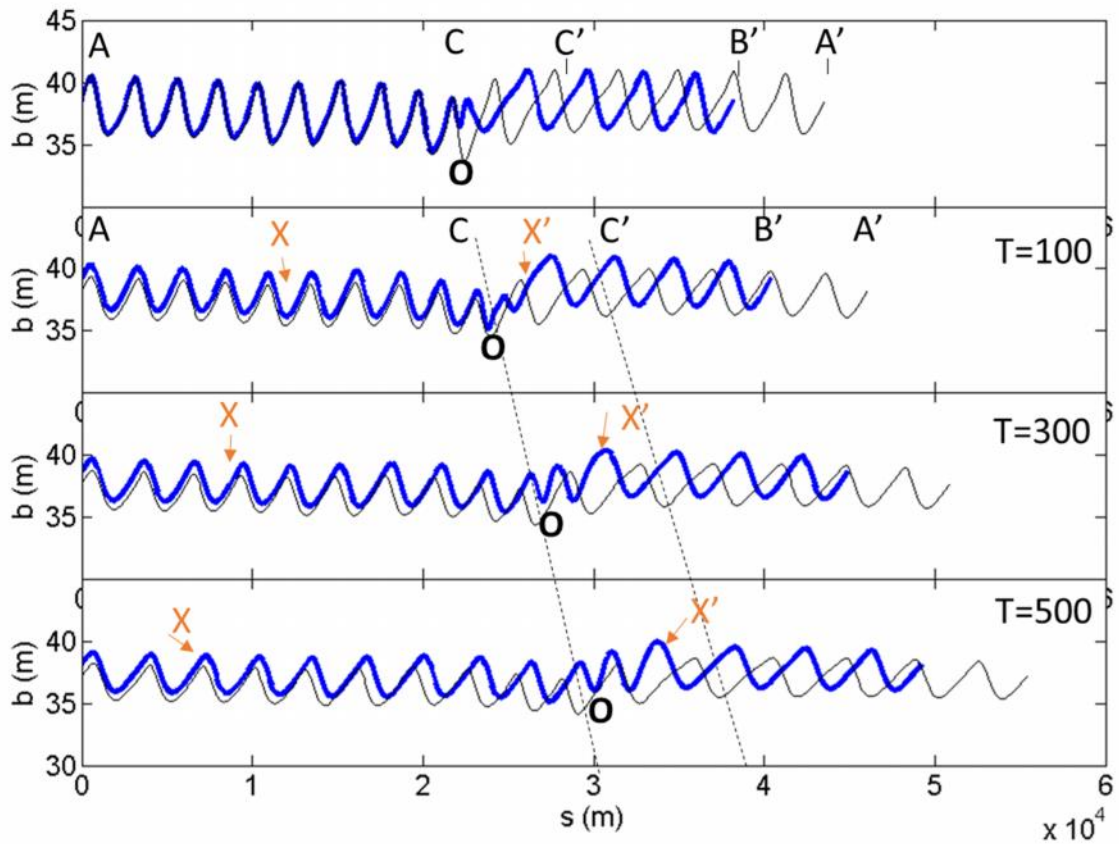


Figure 4.10: Evolution of local channel half-width disturbance generated by cutoff. The thin continuous line indicates the half-width of the channel without cutoff and the thick continuous line indicates the channel with cutoff. The location of incipient cutoff is denoted by point O. The dashed subvertical lines delineate the region of the channel without cutoff (i.e. the thin continuous line) that would have been removed by cutoff. To determine the zone of influence X' the thick line C-B' must be compared with the thin line C'A'

Chapter 5

CONCLUSIONS AND FUTURE WORK

In this study we introduce a bank model formulation, modified from the framework originally proposed by Parker et al. (2011). This formulation includes an erosion submodel based on slump block mitigated natural armoring, a sub-model for the capture of sediment at depositing banks by vegetal encroachment, and a linkage between the two sub-models that allows the model itself to determine, based on local conditions, whether a bank erodes or deposits. The linkage is in the form of a specified threshold formative Shields number which specifies the bankfull hydraulic geometry of a straight channel. If the bed Shields number near a bank exceeds the channel-forming value, the bank erodes; otherwise it deposits.

In its final form, the bank model formulation has three major input parameters which govern bank erosion and depositional processes: a reference erosion rate i'_{Eref} that is a function of measurable bank and slump block parameters; a reference deposition rate i'_{veg} specifying a nominal rate of vegetal encroachment in the absence of floods; and the channel-forming Shields number \dagger^*_{form} that sets both bankfull geometry and the threshold between bank erosion to bank deposition. Near bank shear stresses are computed through a coupled in-channel morphodynamic submodel from which near-bank shear stresses are computed. The in-channel morphodynamics model used is a fully nonlinear flow and bed morphodynamics model based on the iterative solution proposed in Imran et al (2009) and later by Camporeale et al (2007). The model was extended to account for the effects of width variation on flow and bed morphodynamics.

The full model has been applied to the simplified cases of evolution of a straight reach, and evolution of a bend with spatially constant curvature. Input parameters are based on a reach of the Vermillion River, MN, USA. The straight-channel simulations verify that the model overcomes the limitations of the HIPS formulation and predicts the process of channel narrowing (widening) to equilibrium bankfull conditions for an overwide (overnarrow) initial channel. The bend flow simulations show that rather than a final equilibrium, the bend tends towards an asymptotic state where both banks are moving very slowly in the same direction and at nearly the same rate, and bankfull width very slowly declines.

For the bend case, the model identifies 4 possible regimes of channel evolution towards an asymptotic state. These regimes include: both banks eroding, both banks depositing, outward migration with bar push, and outward migration with bank pull. The model shows how, depending upon the choice of \tilde{r}_{Eref} and \tilde{r}_{veg} , an overwide initial channel can first undergo narrowing through deposition at both banks, narrow further by bar push, and then reach the asymptotic state. An overnarrow initial channel can first undergo widening through erosion at both banks, continue widening via bank pull, and then reach the asymptotic state. Increasing \tilde{r}_{Eref} pushes the system toward bank pull, and increasing \tilde{r}_{veg} pushes it toward bar push.

The full model has also been applied to the fully meandering river based loosely on a reach of the Pembina river in Alberta, Canada and the model is able to capture the spatio-temporal co-evolution of curvature, width and bed elevation. The model predicts that up incipient cut-off, the dynamics of curvature and width co-evolution as strongly related to the choice of \tilde{r}_{Eref} and \tilde{r}_{veg} , more specifically, the ratio between these input parameters. A smaller ratio would result in a

configuration where the channel is wider closer to the bend apex, while larger ratios tends towards an opposing configuration where the channel is wider close to the crossing. This changes after cut-off and trends show that over time, regardless of input parameters, the channel approaches a configuration that is narrower closer to the apex and wider closer to the crossing

A key finding in this study is the persistent problem of excessive channel narrowing that follows with the imposition of a constant formative Shields number to describe bankfull characteristics for a migrating river. The problem arises due to the steady reduction in slope as the channel becomes increasingly sinuous. This problem is resolved by appealing to data, which show a clear tendency for the formative Shields number to increase with slope. A slope-dependent relation based on the regression fit of Li et al (submitted, Appendix B) proves sufficient to resolve the problem.

This work represents a first step towards understanding the evolution of width in meandering river systems and has several deficiencies which have been outlined in the study. A future correction would ensure sediment mass balance involve incorporating a source/sink term into the in-channel morphodynamics model that captures material entering and leaving the channel via the channel banks.

A complete model would also to account for the role of washload in meander migration. In the present model, the cohesive layer and bank properties are specified constant over time. The cohesive layer can better be modelled by assumed it to be deposited by overbank sedimentation of fine sediment on the river floodplain. A model that can account for washload would yield realistic

estimates of the cohesive layer producing the slump blocks and thus better modeling bank erosion over time.

REFERENCES

- Abad, J.D. & Garcia, M.H. 2006 RVR Meander: A toolbox for re-meandering of channelized streams. *Computer and Geosciences* **32**, pp. 92-101.
- Allmendinger, N. E., Pizzuto J., Potter N., Johnson T., & Hession W. C. 2007, The influence of riparian vegetation on stream width, eastern Pennsylvania, USA, *Geol. Soc. Am. Bull.*, 117(1/2), 229 – 243, doi:10.1130/B25447.1.
- Asahi, K., Shimizu, Y., Nelson, J. & Parker, G. 2013 Numerical simulation of river meandering with self-evolving banks. *J. Geophys. Res. Earth Surf.* **118**, doi:10.1002/jgrf.20150.
- ASCE Task Committee on Hydraulics, Bank Mechanics and Modeling of River Width Adjustment. 1998 River width adjustment. II: Processes and Mechanisms. *J. Hydr. Eng.* **124**(9), 881-902.
- ASCE Task Committee on Hydraulics, Bank Mechanics and Modeling of River Width Adjustment. 1998 River width adjustment. II: Modeling. *J. Hydr. Eng.* **124**(9), 903-917.
- Bak, P., Tang, C., Wiesenfeld, K. 1987, Self-organised criticality: an explanation of 1/f noise, *Physical Review Letters* **59**, 381-384.
- Beck S, Harrington, R. A. & Andres D.D. 1983 Lateral Channel Stability of the Pembina River near Rossington, Alberta. Alberta Research Council Report No. SWE 83-2.
- Beck S. M. 1988 Computer-Simulated Deformation of Meandering River Patterns, PhD Thesis, University of Minnesota.

- Beeson, C.E. & Doyle P. F. 1995, Comparison of Bank Erosion at Vegetated and Non-vegetated channel bends, *J. Ameri. Water Resour. Assoc.* **31**, 983–990. doi: 10.1111/j.1752-1688.1995.tb03414 .x
- Bittner, L. 1994 River bed response to channel width variation. Master Thesis, Univ. of Illinois.
- Blondeaux, P. & Seminara, G. 1985 A unified bar-bend theory of river meanders. *J. Fluid Mech.* **157**, 449-470.
- Bluck, B. J. 1971 Sedimentation in the meandering River Endrick, Scottish. *J. Geology.***7**, 93-137.
- Braudrick, C. A., Dietrich, W. E., Leverich, G. T. & Sklar, L.S. 2009, Experimental evidence for the conditions necessary to sustain meandering in coarse-bedded rivers, Proceedings of the National Academy of Sciences of the United States of America, 106(40), 16936-16941.
- Brice, J. 1982 Stream channel stability assessment. *Report no. fhwa/rd, Federal Highway Administration, Offices of Research and Development*, 42p.
- Brice, J. 1974 Evolution of meander loops. *Geol. Soc. Am. Bull.* **85**, 215-235.
- Bridge J.S. and Jarvis, J. 1977, Velocity profiles and bed shear stresses over various bed configurations in a river bend. *Earth Surface Processes* **2**, 281-294
- Campbell, J. E. & Hendry, H. E. 1987 Anatomy of a gravelly meander lobe in the Saskatchewan River near Nipawin. In: Ethridge, F. G., Flores, R. M. and Harvey, M. D. (Eds), Recent Developments in Fluvial Sedimentology. Soc. of Economic Paleontologists and Mineralogists Special Publication, 39, 179–190.

- Camporeale, C., Perona, P., Porporato, A. & Ridolfi, L. 2007, Hierarchy of models for meandering rivers and related morphodynamic processes. *Rev. Geophys.* **45**, RG1001, doi:10.1029/2005RG000185.
- Camporeale, C., Perucca, E. & Ridolfi, L. 2008 Significance of cutoff in meandering rivers dynamics. *J. Geophys. Res.* **113**, F01001, doi:10.1029/2006JF000694.
- Colombini, M., Seminara, G. & Tubino, M. 1987 Finite amplitude alternate bars. *J. Fluid Mech.* **181**, 213-232.
- Constantine J.A., S. R. McLean and T. Dunne 2010 A mechanism of chute cutoff along large meandering rivers with uniform floodplain topography, *GSA Bulletin* **122**, no. 5-6; 855-869, doi: 0.1130/B26560.1
- Copeland, R., Soar, P. & Thorne, C. 2005 Channel-forming discharge and hydraulic geometry width predictors in meandering sand-bed rivers, Proc., 2005 World Water and Environmental Resources Congress: Impacts of Global Change (CD-ROM), ASCE, Reston, Va.
- Courant, R.E., Isaacson E. & Rees, M. 1952 On the solution of nonlinear hyperbolic differential equations by finite differences. *J. Communications Pure and Applied Math.* **5**, 243.
- Crosato, A. 1990 Simulation of meandering river processes. Communication on Hydraulic and Geotechnical Engineering, Report 90-3, Delft University of Technology, Delft, NL

- Darby, S.E. & Thorne, C.R. 1996 Development and testing of riverbank stability analysis. *J. Hydraul. Eng.* **122**(8), 443-454.
- Darby, S.E., Alabyan, A.M. & van de Wiel, M.J. 2002 Numerical simulation of bank erosion and channel migration in meandering rivers. *Water Resources Res.* **38** (9), W1163
- Darby, S. E., Rinaldi, M. & Dapporto, S. 2007 Coupled simulations for fluvial erosion and mass wasting for cohesive river banks. *J. Geophys. Res.* **112**, F03022, doi:10.1029/2006JF000722.
- Dietrich, W. E., and P. Whiting, 1989, Boundary shear stress and sediment transport in river meanders of sand and gravel, in River Meandering, Water Resour. Monogr., vol. 12, edited by S. Ikeda and G. Parker, pp. 1– 50, AGU, Washington, D. C.
- Duan, J.G. & Julien, P.Y. 2010 Numerical simulation of meandering evolution. *J. Hydrology* **391**, 34–46.
- Dulal K. P., Kobayashi, K., Shimizu, Y., Parker G. 2010 Numerical computation of free meandering channels with the application of slump blocks on the outer bends. *J. Hydro-environment Res.* **3** (4), 239–246.
- Dulal K.P. & Shimizu, Y. 2010 Experimental simulation of meandering in clay mixed sediments. *J. Hydro-environment Res.* **4**(4), 329–343.
- Einstein, H. A. 1950 The bed-load function for sediment transportation in open channel flows. *Technical Bulletin* 1026, U.S. Dept. of the Army, Soil Conservation Service.

- Eke, E., Shimizu, Y. & Parker, G. 2011 Numerical modeling of meander migration incorporating erosional and depositional bank processes. Proceedings, River, Coastal and Estuarine Morphodynamics Conference, Beijing, China, September 6 – 8, 11 p.
- Eke, E. 2013 Numerical modeling of meander migration incorporating erosional and depositional bank processes, Ph.D. thesis, Dept. of Civil & Environmental Engineering, University of Illinois Urbana-Champaign.
- Eke, E., Parker G. & Shimizu Y. (submitted, a) Numerical modeling of erosional and depositional bank processes in migrating river bends with self-formed width: morphodynamics of bar push and bank pull. *J. Geophys. Res.*
- Eke, E.C, Czapiga, M., Viparelli, E., Shimizu Y., Imran, J., Sun, T., & Parker, G. (submitted, b), Co-evolution of width and sinuosity in meandering rivers. *J. Fluid Mech.*, submitted.
- Engel, F.L. & Rhoads, B.L. 2012 Interaction among mean flow, turbulence, bed morphology, bank failures and channel planform in an evolving compound meander loop. *Geomorphology*, **163–164**, 70–83.
- Engelund, F. 1974 Flow and bed topography in channel bends. *J. Hydraul. Div. ASCE* **100**: 1631-1648.
- Eschner, T., Hadley, R. & Crowley K. 1983 Hydrologic and morphologic changes in channels of the Platte River basin in Colorado, Wyoming, and Nebraska: A historical perspective, U.S. Geol. Surv. Professional Paper 1277-A, A1-A39.

- Evans, M. & Warburton, J. 2001 Transport and dispersal of organic debris (peat blocks) in upland fluvial systems. *Earth Surf. Proc. Landforms* **26**, 1087–1102.
- Ferguson, R. I. 1976 Disturbed periodic model for river meanders. *Earth Surf. Proc.* **1**, 337-347.
- Ferguson, R. I. 1984. Kinematic model of meander migration, in River Meandering, edited by C. Elliot, pp. 942– 951, Am. Soc. of Civ. Eng., New York.
- Fisk, H.N., 1947, Fine-Grained Alluvial Deposits and Their Effects on Mississippi River Activity, Volumes 1 & 2: Vicksburg, Mississippi, Mississippi River Commission, 84 p
- Frascati, A. & Lanzoni, S. 2009 Morphodynamic regime and long-term evolution of meandering rivers. *J. Geophys. Res.* **114**, F02002. doi:10.1029/2008JF001101.
- Frascati, A. & Lanzoni, S. 2010 Long-term river meandering as a part of chaotic dynamics? A contribution from mathematical modelling. *Earth Surf. Proc. Landforms* **35**, 791-802, doi:10.1002/esp.1974.
- Frascati, A. & Lanzoni, S. 2013 A mathematical model for meandering rivers with varying width. *J. Geophys. Res. Earth Surf.* **118**, doi:10.1002/jgrf.20084.
- Frothingham, K. M. and Rhoads, B. L. 2003, Three-dimensional flow structure and channel change in an asymmetrical compound meander loop, Embarras River, Illinois. *Earth Surf. Proc. Landforms* **28**, 625–644, DOI: 10.1002/esp.471.
- Furbish, D.J., 1988, River-bend curvature and migration: How are they related? *Geology* **16**, 752–755, doi: 10.1130/0091-7613.

- Gabet, E. J. 1998 Lateral migration and bank erosion in a saltmarsh tidal channel in San Francisco Bay, California. *Estuaries* **21**(4) 745-753, doi: 10.2307/1353278.
- Gagliano, S. M., & Howard, P. C. 1984. The neck cutoff oxbow lake along the lower Mississippi River, in *River Meandering: Proceedings of the Conference Rivers '83*, edited by C. M. Elliot, pp. 147–158, Am. Soc. Of Civ. Eng., New York.
- Garcia M.H. 2008 *Sediment Transport and Morphodynamics*, Chapter 2, Sedimentation Engineering. ASCE Manual No. 110, American Society of Civil Engineers, M. H. Garcia, ed., ISBN 10 # 0784408149, ISBN 13 # 978078440814: 1050 p.
- Gay, G. R., Gay, H. H., Gay, W. H., Martinson, H. A., Meade, R. H. & Moody, J. A. 1998 Evolution of cutoffs across meander necks in Powder River, Montana, USA. *Earth Surf. Proc. Landforms* **23**, 651– 662.
- Goodwin, C. N., Steidtmann, J. R. 1981 The convex bar: member of the alluvial channel side-bar continuum. *J. Sedimentary Petrology* **51**(1): 129-136.
- Güneralp, I. & Rhoads, B. L. 2011 Influence of floodplain erosional heterogeneity on planform complexity of meandering rivers. *Geophys. Res. Lett.* **38**, L14401, doi:10.1029/2011GL048134.
- Gurnell, A.M., Morrissey, I. P., Boitsidis, A. J., Bark, T., Clifford, N. J., Petts, G. E. & Thompson, K. 2006 Initial adjustments within a new river channel: Interactions between fluvial processes, colonizing vegetation, and bank profile development. *Env. Management* **38**, (4) 580-596.

- Hack, J.T. 1965 Post-glacial drainage evolution and stream geometry in the Ontonagon area, Michigan. *U.S. Geol. Surv. Prof. Paper* no 504-13.
- Hasegawa, K. 1977 Computer simulation of the gradual migration of meandering channels. In *Proc. of the Hokkaido Branch, Japan Society of Civil Engineering*, pp. 197-202, in Japanese.
- Hey, R. D. 1976, Geometry of river meanders. *Nature* **262**, 482-484.
- Hickin, E. J. 1974 The development of meanders in natural river channels. *Amer. J. of Science* **274**, 414–442.
- Hickin, E. J. & Nanson G 1975 The character of channel migration on the Beatton River, northeast British Columbia, Canada. *Bulletin of the Geol. Soc. of America* **86**, 487–494.
- Hickin, E. J. & Nanson, G. 1984 Lateral migration rates of river bends. *J. Hydraul. Eng.* **110**, 1557–67.
- Hooke, J. M. 1980, Magnitude and distribution of rates of river bank erosion, *Earth Surf. Proc. Landforms* **5**, 143–157.
- Hooke, J.M., 1995, River channel adjustment to meander cutoffs on the River Bollin and River Dane, northwest England: *Geomorphology* **14**, 235–253, doi: 10.1016/0169-555X(95)00110-Q.

- Hooke, J.M., and Redmond, C.E., 1992, Causes and nature of river planform change, in Billi, P., Hey, R.D., Thorne, C.R., and Tacconi, P., eds., *Dynamics of Gravel-Bed Rivers*: New York, John Wiley & Sons, p. 557–571.
- Hooke, J. 2003 River meander behaviour and instability: a framework for analysis. *Trans Inst Br Geogr NS* 28 238–25.
- Hooke, J.M. 2007 Spatial variability, mechanisms and propagation of change in an active meandering river. *Geomorphology* **84**, 277-296.
- Hooke, J.M. 2008 Temporal variations in fluvial processes on an active meandering river over a 20-year period. *Geomorphology* **100**, 3-13.
- Howard, A. D. & Knutson, T. R. 1984 Sufficient conditions for river meandering: A simulation approach. *Water Res. Res.* **20**, 1659-1667.
- Howard, A. D. 1984, Simulation model of meandering, in *River Meandering: Proceedings of the Conference Rivers '83*, edited by C. M. Elliott, pp. 952– 963, Am. Soc. of Civ. Eng., New York.
- Howard, A. 1992 Modelling channel evolution and floodplain morphology. In *Floodplain Processes* edited by M.G. Anderson, D.E. Walling and P.D. Bates, pp. 15-62, John Wiley, New York.

- Howard, A. D. 1996 Modeling channel migration and floodplain sedimentation in meandering streams. In *Lowland floodplain rivers: Geomorphological perspectives* edited by P.A. Carling and G.E. Petts pp. 2-41, John Wiley, NY.
- Huang, H. Q., & Nanson, G. C. 1997 Vegetation and channel variation; a case study of four small streams in South(eastern Australia). *Geomorphology* **18**, 237–249.
- Hupp, C.R. & Simon, A. 1991 Bank accretion and the development of vegetated depositional surfaces along modified alluvial channels. *Geomorphology* **4**, 111-124.
- Ikeda, S., Hino, M. & Kikkawa, H. 1976 Theoretical study on the free meandering of rivers. *Proc. Japan Soc. Civ. Engrs.* **255**, pp. 63 – 74 (in Japanese).
- Ikeda, S., Parker, G. & Sawai, K. 1981 Bend theory of river meanders. Part 1. Linear development. *J. Fluid. Mech.* **112**, 363-377.
- Imran, J., Parker, G. & Pirmez, C. 1999 A nonlinear model of flow in meandering submarine and subaerial channels, *J. Fluid Mech.* **400**, 295–331.
- Johannesson, H. & Parker, G. 1989 Linear theory of river meanders. In *River Meandering, Water Resources Monograph* **12**, 181-213, S. Ikeda and G. Parker ed. American Geophysical Union.
- Karlstrom, L., Gajjar, P. & Manga, M. 2013 Meander formation in supraglacial streams, *J. Geophys. Res. Earth Surface*, published online: 17 Sep., DOI: 10.1002/jgrf.20135

Kean, J. W., & Smith, J. D. Form drag in rivers due to small-scale natural topographic features:

1. Regular sequences. *J. Geophys. Res.* **111**, F04009, doi:10.1029/2006JF000467.

Kitanidis, P. K. & Kennedy, J. F. 1984 Secondary current and river meander formation. *J. Fluid Mech.* **144**, 217-229.

Konsoer, K. M, Rhoads, B. L., Langendoen, E. J., Johnson, K. & Ursic, M. 2012 Influence of riparian vegetation on near-bank flow structure and erosion rates on a large meandering river. *Abstract EP43C-06*, 2012 Fall Meeting, AGU, San Francisco, Calif., 3-7 Dec.

Konsoer K., Zinger, J. & Parker, G. 2013 Bankfull hydraulic geometry of submarine channels created by turbidity currents: relations between bankfull channel characteristics and formative flow discharge. *J. Geophys. Res. Earth Surface*, **118**(1), 216–228, doi:10.1029/2012JF002422.

Lagasse P., Spitz, W., Zevenbergen, L. & Zachmann, D. 2004 Handbook for predicting stream meander migration. NHCRP Report 533, National Cooperative Highway Research Program, 107 pp.

Lancaster, S.T., & Bras, R. L. 2002 A simple model of river meandering and its comparison to natural channels. *Hydrological Processes* **16**, 126

Lane, E. W. 1955 Design of stable channels, *J. Hydr. Eng.* **120**, 1234 – 1279.

Langendoen, E. J., and Simon, A. 2008 Modeling the evolution of incised streams. II: Streambank erosion, *J. Hydraul. Eng.* **134**(7)

- Lanzoni, S. & Seminara, G. 2006 On the nature of meander instability. *J. Geophys. Res.* **111**, F04006, doi:10.1029/2005JF000416.
- Lauer, J.W. & Parker G. 2008 Net local removal of floodplain sediment by river meander migration, *Geomorphology* **96**, 123-149.
- Leopold, L. B. & Maddock, T.J. 1953 Hydraulic geometry of stream channels and some physiographic implications. U. S. Geological Survey Professional Paper 252, 55 p.
- Leopold L. B. & Wolman, M.G. 1960 River Meanders. *Geol. Soc. of America* **71**, 6, 769-793.
- Lewis, G.W., and Lewin, J., 1983, Alluvial cutoffs in Wales and Borderlands, in Collinson, J.D., and Lewin, J., eds., Modern and Ancient Fluvial Systems. *Intl Association of Sedimentologists Special Publication* **6**, p. 145–154.
- Li, C., Czapiga, M.J, Eke, E.C., Viparelli E. & Parker, G. 2013 River bankfull geometry: Shear velocity is viscosity-dependent but grain size-independent. *Nature Geosciences*, submitted.
- Luchi, R., Zolezzi, G. & Tubino. M. 2010 Modelling mid-channel bars in meandering channels. *Earth Surf. Proc. Landforms* **35**, 902–917.
- Luchi, R., Zolezzi, G. & Tubino, M. 2011, Bend theory of river meanders with spatial width variations. *J. Fluid Mech.* **681**, 311–339, doi:10.1017/jfm.2011.200.
- Luchi, R., Bolla Pittaluga, M. & Seminara, G. 2012 Spatial width oscillations in meandering rivers at equilibrium. *Water Resour. Res.* **48**, W05551, doi:10.1029/2011WR011117

- MacDonald, T. Parker, G. & Leuthe, D. 1991 Inventory and analysis of stream meander problems in Minnesota. Project Report, St. Anthony Falls Hydraulic Laboratory, University of Minnesota.
- Matsubara, Y., Howard, A. D., Burr, D. M., Williams, R. M. & Moore, J. M. 2012 Meandering Channels in a Non-Vegetated Area: Quinn River, NV as a Martian Analog. *Lunar and Planetary Institute Science Conference Abstracts* **43**, 2534.
- Micheli, E. R. & Kirchner, J. W. 2002 Effects of wet meadow riparian vegetation on streambank erosion: 2. Measurements of vegetated bank strength and consequences for failure mechanics. *Earth Surf. Proc. Landforms* **27**, 687–697.
- Moorman, R. K. 1990 An investigation into the uses and usefulness of R I Ferguson's simple kinematic model in the study of meander behaviour and development BSc Dissertation Department of Geography, Portsmouth Polytechnic.
- Mosley, M. P. 1975. Meander cutoffs on the River Bollin, Cheshire, in July 1973. *Revue de Geomorphologie Dynamique* **24**(1), 21–31.
- Mosselman, E. 1998 Morphological modeling of rivers with erodible banks. *Hydrol. Proc.* **12**, 1357-1370.
- Motta D., Abad, J.D., Langendoen, E.J & Garcia, M.H. 2012a A simplified 2-D model for meander migration with physically based bank evolution. *Geomorphology* 163–164, 10–25.

- Motta D., Abad, J.D., Langendoen, E.J & Garcia, M.H. 2012b The effects of floodplain soil heterogeneity on meander planform shape. *Water Resour. Res.* **48**, W09518, doi:10.1029/2011WR011601.
- Murgatroyd A. & Ternan, J. 1983 The impact of afforestation on stream bank erosion and channel form, *Earth Surf. Proc. Landforms* **8**, 357-369.
- Nagata, N., Hosoda, T. & Muramoto, Y. 2000 Numerical analysis of river channel processes with bank erosion. *J. Hydraul. Eng.* **126**(4), 243–251.
- Nelson, J. M. & Smith, J. D. 1989 Evolution and stability of erodible channel beds. In *River Meandering, Water Resources Monograph* **12**, 321-377, S. Ikeda and G. Parker ed., American Geophysical Union.
- Page, K.J., Nanson, G.C., & Frazier, P.S. 2003 Floodplain formation and sediment stratigraphy resulting from oblique accretion on the Murrumbidgee River, Australia. *J. Sed. Res.* **73**, 5-14.
- Paola, C., Heller, P. L., & Angevine, C. L. 1992 The large-scale dynamics of grain-size variation in alluvial basins, 1: Theory. *Basin Research* **4**, 73-90.
- Parker, G 1976 On the cause and characteristic scales of meandering and braiding in rivers. *J. Fluid Mech.* **76** (3), 457–480, doi:10.1017/S0022112076000748.
- Parker, G. 1978 Self-formed straight rivers with equilibrium banks and mobile bed. Part 2, the gravel river, *J. Fluid Mech.* **89**, 127-146.

- Parker, G. 1979 Hydraulic geometry of active gravel rivers. *J. Hydraul. Eng.* **105**(9), 1185-1201.
- Parker, Sawai, K. & Ikeda, S. 1982 Bend theory of river meanders: Part II, Nonlinear deformation of finite-amplitude bends. *J. Fluid Mech.* **115**, pp. 303-314.
- Parker, G., Diplas, P. & Akiyama, J. 1983 Meander bends of high amplitude. *J. Hydraul. Eng. ASCE* **109**, 1323-1337.
- Parker, G. & Andrews E. D 1985 Sorting of bed load sediments by flow in meander bends. *Water Res. Res.* **21**, 1361-1373.
- Parker, G. & Andrews, E. D. 1986 On the time development of meander bends. *J. Fluid Mech.* **162**, 139-156.
- Parker, G., Paola, C. Whipple, K. X. & Mohrig, D. 1998 Alluvial fans formed by channelized fluvial and sheet flow: Theory. *J. Hydraul. Eng.* **123**, 985-995.
- Parker, G., Paola, C., Whipple, K. X., Mohrig, D., Toro-Escobar, C. M., Halverson, M., & Skoglund, T.W 1998b Alluvial fans formed by channelized fluvial and sheet Flow. II: Applications. *J. Hydraul. Eng.* **124**(10), 996-1004.
- Parker, G. 2004 1D Sediment Transport Morphodynamics with applications to rivers and turbidity currents. E-book downloadable at <http://hydrolab.illinois.edu/people/parkerg//?q=people/parkerg/>.

- Parker, G., Wilcock, P.R., Paola, C., Dietrich, W. E. & Pitlick, J. 2007 Physical basis for quasi-universal relations describing bankfull hydraulic geometry of single-thread gravel bed rivers. *J. Geophys. Res.* **112**, F04005, doi:10.1029/2006JF000549.
- Parker, G., Muto, T., Akamatsu, Y., Dietrich, W.E. & Lauer, J.W. 2008 Unraveling the conundrum of river response to rising sea level: from laboratory to field. Part II. The Fly-Strickland River System, Papua New Guinea. *Sedimentology* **55**(6), 1657-1688.
- Parker, G., Shimizu, Y., Wilkerson, G. V., Eke, E. C., Abad, J. D., Lauer, J. W., Paola, C., Dietrich, W. E. & Voller, V. R. 2011 A new framework for modeling the migration of meandering rivers. *Earth Surf. Proc. Landforms* **36**, 70–86. doi: 10.1002/esp.2113.
- Parker, G, Eke, E., Asahi, K., Shimizu, Y. & Nelson, J.M. 2013 Vegetal encroachment on point bar deposits as a control on width variation in meandering, Eos Trans. AGU, 93, Fall Meet. Suppl., Abstract EP53H-01.
- Perucca, E., Camporeale, C. & Ridolfi, L. 2006 Influence of river meandering dynamics on the riparian vegetation pattern formation. *J. Geophys. Res.* **111**, G01001, doi:10.1029/2005JG000073.
- Perucca, E., Camporeale, C. & Ridolfi, L. 2007 Significance of the riparian vegetation dynamics on meandering river morphodynamics. *Water Resour. Res.* **43**, W03430, doi:10.1029/2006WR005234.
- Peyret, A. B. 2011 Morphodynamics and geometry of channels, turbidites and bedforms. Doctoral dissertation, University of Texas at Austin.

- Pizzuto J. E 1984 Bank erodibility of shallow sandbed streams. *Earth Surf. Proc. Landforms* **9**, 113–124.
- Repetto, R., Tubino, M. & Paola, C. 2002 Planimetric instability of channels with variable width. *J. Fluid Mech.* **457**, 79–109.
- Rinaldi, M., Mengoni, B., Luppi, L., Darby, S.E. & Mosselman, E. 2008 Numerical simulation of hydrodynamics and bank erosion in a river bend. *Water Resour. Res.* **44** (9), W09428
- Rozovskii, I. L. 1957 Flow of Water in Bends of Open Channels. Academy of Sciences of the Ukrainian SSR, Kiev (translated from Russian by the Israel Program for Scientific Translations, Jerusalem, 1961), 233 pp.
- Rüther N. & Olsen, N.R.B. 2007 Modelling free-forming meander evolution in a laboratory channel using three-dimensional computational fluid dynamics. *Geomorphology* **89**, 308–319.
- Seminara, G., Zolezzi, G., Tubino, M. & Zardi, D. 2001 Downstream and upstream influence in river meandering, Part 2. Planimetric development. *J. Fluid Mech.* **438**, 213-230.
- Seminara G. 2006 Meanders. *J. Fluid Mech.* **554**, 271-297 doi:10.1017/S0022112006008925
- Simon A., Curini, A., Darby, S.E., & Langendoen, E. 1999 Streambank mechanics and the role of bank and near bank processes in incised channels. Incised channels: processes, Forms, Engineering and Management, Darby S.E., Simon A. (eds). Wiley: Chichester; 123-152.

- Simon, A., & Collison, A.J.C. 2002 Quantifying the mechanical and hydrologic effects of riparian vegetation on streambank stability. *Earth Surf. Proc. Landforms* **27**, 527-546.
- Smith, C. E. 1998 Modeling high sinuosity meanders in a small flume. *Geomorphology* **25**,19–30.
- Smith D. & McLean, S. R. 1984 A model of flow in meandering streams. *Water Resour. Res.* **20**, 1301-1315.
- Smith V. B. 2012 Geomorphology of a coastal sand-bed river: Lower Trinity River, Texas. Doctoral Dissertation, University of Texas at Austin.
- Solari, L. & Seminara, G. 2005 On width variations in river meanders. In *Symp. on River, Coastal and Estuarine Morphodynamics*, Urbana, Illinois, 4–7 October.
- Stillwater Science 2007 Physical Modeling Experiments to Guide River Restoration Projects: Channel-floodplain Redesign Experiments. Report prepared for CALFED Ecosystem Restoration Program (Contract No. ERP-02D-P55), 40p.
- Stolum, H.H. 1996 River meandering as a self-organized process. *Science* **271**, 1710-1713.
- Stolum, H. H. 1998 Planform geometry and dynamics of meandering rivers, *Geological Society of America Bulletin* **110** 1485–98.
- Stott, T.A. 1997 A comparison of stream bank erosion processes on forested and moorland streams in the Balquhidder catchments, Central Scotland. *Earth Surf. Proc. Landforms* **22**(4), 383–401.

- Struiksmā, N., Olesen, K. W., Flokstra, C. & De Vriend, H. J. 1985 Bed deformations in curved alluvial channels, *J. Hydraul. Res.* **23**, 57-79.
- Sun, T., Meaking, P., Jossang, T. & Schwarz, K. 1996 A simulation model for meandering rivers. *Water Resour. Res.* **32**(9), 2937-2954.
- Swenson, J.B., Voller, V. R., Paola, C., Parker, G., & Marr, J. 2000 Fluvio-deltaic sedimentation: a generalized Stefan problem. *European J. Applied Math.* **11**, 433-452.
- Tal, M., & Paola, C. 2010 Effects of vegetation on channel morphodynamics: results and insights from laboratory experiments. *Earth Surf. Proc. Landforms* **35**, 1014-1028. doi: 10.1002/esp.
- Thorne, C. R 1990 Vegetation and Erosion, Thornes, J. B (ed), Wiley, Chichester 125-144.
- Thorne, C.R. & Lewin, J. 1979 Bank processes, bed material movement and planform development in a meandering river. In Rhodes, D.D. and Williams, G.P. (eds.) *Adjustments of the Fluvial System*, Debuque, Iowa: Kendall/Hunt, p. 117-137.
- Thorne, C. R., & Tovey, K. 1981 Stability of composite river banks. *Earth Surf. Proc. Landforms* **6**, 469–484.
- Tsujimoto T. 1999 Fluvial processes in streams with vegetation. *J. Hydraul. Res.* **37**(6), 789-803.
- van Dijk W. M., van de Lageweg, W. I. & Kleinhans M. G. 2013 Formation of a cohesive floodplain in a dynamic experimental meandering river. *Earth Surf. Proc. Landforms*, DOI: 10.1002/esp.3400

- de Vries, M. 1965 Considerations about non-steady bed-load transport in open channels. In *Proc. of 11th Congress, International Association for Hydraulic Research, Leningrad*, pp. 381-388.
- Wilkerson G. V. & Parker, G. 2010 Physical basis for quasi-universal relations describing bankfull hydraulic geometry of sand-bed rivers, *J. Hydraul. Eng.* doi:10.1061/(ASCE)HY.1943-7900.0000352.
- Wolman, M.G., & Leopold, L. B. 1957 River Flood Plains: Some Observations on their Formation. *U.S.G.S. Professional Paper 282-C*, 30p.
- Wood A. L, Simon, A., Downs, P. W. & Thorne, C. R. 2001 Bank-toe processes in incised channels: the role of apparent cohesion in the entrainment of failed bank materials. *Hydrol. Proc.* **15**, 39–61.
- Wu, F.-C., & Yeh, T.-H. 2005 Forced bars induced by variations of channel width: Implications for incipient bifurcation. *J. Geophys. Res.* **110**, F02009, doi:10.1029/2004JF000160.
- Wu, F.-C., Shao Y.-C. & Chen, Y.-C. 2011 Quantifying the forcing effect of channel width variations on free bars: Morphodynamic modeling based on characteristic dissipative Galerkin scheme. *J. Geophys. Res.* **116**, F03023, doi:10.1029/2010JF001941.
- Yi, A. 2006 Modeling of flow and migration of subarctic and submarine meandering channels. PhD thesis, University of South Carolina.

Zinger, J.A, B.L. Rhoads, J.L. Best. 2011 Extreme sediment pulses generated by bend cutoffs along a large meandering river. *Nature Geosciences* **4**, 675-678

Zolezzi, G. & Seminara, G. 2001 Downstream and upstream influence in river meandering. Part 1. General theory and application of overdeepening. *J. Fluid Mech.* **438**, 183–211.

Zolezzi, G., Luchi, R. & Tubino, M. 2012 Modeling morphodynamic processes in meandering rivers with spatial width variations. *Rev. Geophys.* **50**: doi: 10.1029/2012RG000392. issn: 8755-1209.

Appendix A

NONLINEAR FLOW MODEL SOLUTION

A1. “D” SOLUTIONS

Integrating the continuity equation (3.17) from the left bank $n = -1$ to n subject to the boundary conditions in (3.28), we get the following solution for the transverse velocity in integral form, i.e.

$$v_d = -\frac{\partial b_d}{\partial s} - (n+1) \left(\frac{\partial u_{dc}}{\partial s} + \frac{\partial \zeta_{dc}}{\partial s} - \frac{\partial y_{dc}}{\partial s} \right) - \frac{\partial}{\partial s} \int_{-1}^n (u_{dd} + h_{dd}) dn' + R_1 \quad (\text{A.1})$$

where

$$\begin{aligned} R_1 = & -\frac{\partial}{\partial s} \int_{-1}^n (h_{do} + \zeta_d - y_d)(u_{do} + u_d) dn' - v_d [h_{do} + \zeta_d - y_d + nbcH] \\ & - \frac{\partial}{\partial s} b_d \int_{-1}^n ((u_{do} + u_d)H + h_{do} + \zeta_d - y_d) dn' + n((u_{do} + u_d)H + h_{do} + \zeta_d - y_d) \frac{db_d}{ds} \end{aligned} \quad (\text{A.2})$$

The streamwise momentum equation (3.18) can be rewritten as follows:

$$\begin{aligned} & \frac{\partial (u_{dd} + u_{dc})}{\partial s} + 2v(u_{do} + u_{dd} + u_{dc}) - v(h_{do} + \zeta_{dc} + \zeta_{dd} - y_{dc} - y_{dd}) \\ & - vS_{do} + F_o^{-2} \frac{\partial (\zeta_{dd} + \zeta_{dc})}{\partial s} + vnC = R_2 \end{aligned} \quad (\text{A.3})$$

where $v = \chi_o C_f$ and

$$\begin{aligned}
R_2 = & v(1 + b_d S_{do}) - \frac{v_d}{N} \frac{\partial u_{dd}}{\partial n} - U \left(b_d \frac{\partial (u_{dc} + u_{dd})}{\partial s} - n \frac{db_d}{ds} \frac{\partial u_{dd}}{\partial n} \right) \\
& - (u_{do} + u_{dc} + u_{dd}) \frac{\partial (u_{dc} + u_{dd})}{\partial s} - bcU(v_d + 2\xi) \\
& - \frac{1}{HN} \frac{\partial HU\xi}{\partial n} - F_o^{-2} \left(b_d \frac{\partial (\zeta_{dd} + \zeta_{dc})}{\partial s} - n \frac{\partial b_d}{\partial s} \frac{\partial \zeta_{dd}}{\partial n} \right) \\
& - b\kappa_o \frac{\dagger_n}{HN} + v \left[2(u_{do} + u_{dc} + u_{dd}) - (h_{do} + \zeta_{dc} + \zeta_{dd} - y_{dc} + y_{dd}) + nc + b_d \right]
\end{aligned} \tag{A.4}$$

Integrating (A3) from the left bank to the right bank, we get:

$$\frac{\partial u_{dc}}{\partial s} - v S_{do} + 2v(u_{do} + u_{dc}) - v(h_{do} + \zeta_{dc} - y_{dc}) + F_o^{-2} \frac{\partial \zeta_{dc}}{\partial s} = R_{21} \tag{A.5}$$

where

$$R_{21} = \frac{1}{2} \int_{-1}^1 R_2 dn \tag{A.6}$$

Further integrating (A5) in the streamwise direction from 0 to L, we get:

$$-S_{do} + 2u_{do} - h_{do} = R_{22} \tag{A.7}$$

where

$$R_{22} = \frac{1}{\sqrt{L}} \int_0^L R_{21} ds \tag{A.8}$$

Thus, the solution to the “D” components of the streamwise velocity is obtained in integral form by subtracting (A5) from (A3) i.e.:

$$u_{dd} = u_{dd}(0, n)e^{-2vs} + e^{-2vs} \int_0^s e^{2vs} \left[v \langle_{dd} - y_{dd} - F_o^{-2} \frac{\partial \langle_{dd}}{\partial s} - vnc + R_{23} \right] ds' \quad (\text{A.9})$$

where the periodic upstream boundary condition in (A9) is given as:

$$u_{dd}(0, n) = \frac{1}{(e^{2vL} - 1)} \int_0^L e^{2vs} \left[\langle_{dd} - y_{dd} - nc - F_o^{-2} \frac{\partial \langle_{dd}}{\partial s} + R_{23} \right] ds' \quad (\text{A.10})$$

In the above relation,

$$R_{23} = R_2 - \frac{1}{2} \int_{-1}^1 R_2 dn \quad (\text{A.11})$$

From equation (19) we get the solution for the “D” component of the water surface elevation, i.e.

$$\langle_{dd} = F_o^2 cn - F_o^2 \int_{-1}^n R_3 dn' + F_o^2 \frac{1}{2} \int_{-1}^1 \int_{-1}^n R_3 dn' dn'' \quad (\text{A.12})$$

where

$$R_3 = -v_d \frac{\partial v_d}{\partial n} - UbL_{sn}(V) - \frac{1}{H} bL_{sn}(UH\{\}) - cNb(2v_d\{\} + \mathbb{E} - U^2) + c - 2 \frac{1}{H} \frac{\partial HV\{\}}{\partial n} - \frac{1}{H} \frac{\partial H\mathbb{E}}{\partial n} - b \frac{x_o \ddagger_n}{H} \quad (\text{A.13})$$

And finally the “D” solution for the bed elevation perturbation is obtained from equation (22),

i.e.

$$y_{dd} = \frac{x_o \sqrt{\ddagger_{so}}}{r} \left[\left(\frac{\partial b_d}{\partial s} + \frac{G(0)}{tv} c \right) n + \int_{-1}^n \Lambda dn' - \frac{1}{2} \int_{-1}^1 \int_{-1}^n \Lambda dn' dn'' + \int_{-1}^n R_4 dn' - \frac{1}{2} \int_{-1}^1 \int_{-1}^n R_4 dn' dn'' \right] \quad (\text{A.14})$$

where

$$\Lambda = M \frac{\partial \int_{-1}^n (u_{dd} + u_{dc}) dn'}{\partial s} + v_d \quad (\text{A.15})$$

and

$$\begin{aligned} R_4 = & \frac{\partial}{\partial s} \left(b_d \int_{-1}^n (M(U-1) + R_q) dn \right) + \frac{\partial}{\partial s} \int_{-1}^n R_q dn' - n \frac{db_d}{ds} (M(U-1) + R_q) \\ & + q_n (1 + nbc) - v_d - \frac{G(0)}{tv} c + \frac{r}{\chi_o \sqrt{\ddagger_o^*}} \frac{\partial y_{dd}}{\partial n} \end{aligned} \quad (\text{A.16})$$

A2. "O" and "C" SOLUTIONS

Substituting the decompositions (34) and (35) into the constant discharge and sediment transport conditions of (30) and (31), we get, respectively

$$\begin{aligned} u_{do} + u_{dc} + h_{do} + h_{dc} - y_{dc} + b_d &= R_5 \\ u_{do} + u_{dc} + \frac{b_d}{M} &= R_6 \end{aligned} \quad (\text{A.17})$$

where

$$R_5 = -(1 + b_d)(u_{do} + u_{dc})(h_{do} + h_{dc}) - b_d [h_{do} + h_{dc} + u_{do} + u_{dc}] - (1 + b_d) \frac{1}{2} \int_{-1}^1 u_{dd} h_{dd} dn' \quad (\text{A.18})$$

$$R_6 = -(u_{do} + u_{dc})b_d - (1 + b_d) \frac{1}{2M} \int_{-1}^1 R_q dn \quad (\text{A.19})$$

Integrating (A17) in the streamwise direction from 0 to L , and considering (A7) we get the “O”

Solutions:

$$\begin{aligned}
 u_{do} &= -\frac{1}{ML} \int_0^L b_d ds + R_{61} \\
 h_{do} &= \left(\frac{1-M}{M} \right) \frac{1}{L} \int_0^L b_d ds + R_{51} - R_{61} \\
 S_{do} &= -\left(\frac{3-M}{M} \right) \frac{1}{L} \int_0^L b_d ds - R_{51} + 3R_{61} - R_{22}
 \end{aligned} \tag{A.20}$$

The “C” solutions are obtained from (A17) and considering (A5), we find that

$$\begin{aligned}
 u_{dc} &= -\frac{1}{M} \left(b_d - \frac{1}{L} \int_0^L b_d ds \right) + R_{62} \\
 \langle_{dc} &= \langle_{dc}(0) + F_o^2 \int_0^s \left[\frac{1}{M} \frac{\partial b_d}{\partial s} - v \left(\frac{1+M}{M} \right) \left(b_d - \frac{1}{L} \int_0^L b_d ds \right) - v (3R_{62} - R_{52}) + R_{24} - \frac{\partial R_{62}}{\partial s} \right] ds' \\
 y_{dc} &= \langle_{dc} + \left(\frac{M-1}{M} \right) \left(b_d - \frac{1}{L} \int_0^L b_d ds \right) + R_{62} - R_{52}
 \end{aligned} \tag{A.21}$$

where

$$\begin{aligned}
 R_{51} &= \frac{1}{L} \int_0^L R_5 ds'; \quad R_{61} = \frac{1}{L} \int_0^L R_6 ds' \\
 R_{24} &= R_{21} - R_{22}; \quad R_{52} = R_5 - R_{51}; \quad R_{62} = R_6 - R_{61}
 \end{aligned} \tag{A.22}$$

The upstream boundary condition in (3.35) is obtained using the condition defined in (3.20) so that

$$\langle_{dc}(0) = -F_o^2 \frac{1}{L} \int_o^L \int_o^s \left[\frac{1}{M} \frac{\partial b_d}{\partial s} - v \left(\frac{1+M}{M} \right) \left(b_d - \frac{1}{L} \int_0^L b_d ds \right) + R_{24} - 3v R_{62} + v R_{52} - \frac{\partial R_{62}}{\partial s} \right] ds' ds''$$

(A.23)

It should be noted here that the character of the “C” problem has changed completely compared to that described in Imran et al., (1999) for the case of flow over a fixed bed. The computation of \langle_{dc} in the case of a fixed bed is dependent on whether the flow is Froude-supercritical or Froude-subcritical. The integration must be performed from upstream when the Froude number is greater than one, but from downstream when the Froude number less than one. Now by relaxing the fixed-bed condition, with this new formulation there is no need to consider the direction of integration in accordance with the Froude number for the “C” problem.

Appendix B

RIVER BANKFULL GEOMETRY: SHEAR VELOCITY IS VISCOSITY-DEPENDENT BUT GRAIN SIZE-INDEPENDENT

C. Li^{1*}, M. Czapiga¹, E.C. Eke^{1,2}, E. Viparelli³, G. Parker^{1,4}

¹Department of Civil and Environmental Engineering, University of Illinois Urbana-Champaign,
Urbana IL 61801 USA

²Department of Geography and Environmental Engineering, Johns Hopkins University,
Baltimore MD 21218 USA

³Department of Civil and Environmental Engineering, University of South Carolina, Columbia
SC 29208, USA

⁴Department of Geology, University of Illinois Urbana-Champaign, Urbana IL 61801 USA

*Correspondence to: chuanli2@illinois.edu

Abstract

The bankfull geometry of alluvial rivers is thought to be controlled by water and sediment supply, and characteristic sediment size. Here we demonstrate a result that flies in the face of a half-century of river research: bankfull shear velocity and bankfull depth are, to first order, independent of bed material grain size. We demonstrate this using similarity collapse for bankfull Shields number as a function of slope and grain size, obtained with data for 230 rivers ranging from silt-bed to cobble-

bed. We interpret this behavior via a hidden parameter: the grain size characterizing the floodplain material. Our analysis shows that bankfull Shields number increase with slope to about the half power. Our results have applicability to field scale morphodynamic modeling of rivers and deltas.

Main Text

The bankfull geometry of alluvial rivers is characterized in terms of bankfull width B_{bf} , bankfull depth H_{bf} and bankfull discharge Q_{bf} (1). The physics behind these relations also involve characteristic bed material grain size D , submerged specific gravity of sediment R (~ 1.65 for quartz), water viscosity ϵ , bed slope S and total volume bed material load (bedload plus suspended bed material load) Q_{tbf} at bankfull flow (2, 3).

A central question of fluvial geomorphology is how channel characteristics vary with flood discharge, sediment supply and sediment size. The problem can be characterized in terms of relations for B_{bf} , H_{bf} and S as functions of Q_{bf} , Q_{tbf} and D . Earlier attempts to specify closures for these relations have assumed a specified formative (bankfull) channel Shields number τ_{bf}^* (4-6), i.e. a constant value of 0.042 (5) or 0.049 (7) for gravel-bed rivers, and 1.8 (6) or 1.86 (7, 8) for sand-bed rivers.

This assumption has been combined with a) normal-flow momentum balance, b) a specification for channel resistance, and c) a total bed material transport relation to study e.g. how rivers respond to basin subsidence and rising base level (4, 7, 8) and how deltas evolve (9).

Here we rely on two compendiums of data on bankfull characteristics of single-thread alluvial channels to revisit the empirical formulation for bankfull Shields number (2, 3). The data base includes 230 river reaches, with Q_{bf} varying from 0.34 to 216,340 m³/s, B_{bf} varying from 2.3 to 3,400 m, H_{bf} varying from 0.22 to 48.1 m, S varying from 8.8×10^{-6} to 5.2×10^{-2} , and D varying from 0.04 to 168 mm.

We estimate bankfull boundary shear stress \dagger_{bf} using the normal flow approximation for momentum balance:

$$\dagger_{bf} = \dots g H_{bf} S, \quad (\text{B. 1})$$

where \dots is water density and g is gravitational acceleration. The dimensionless Shields number is

$$\dagger_{bf}^* = \frac{\dagger_{bf}}{\dots R g D}. \quad (\text{B. 2})$$

Here $R = 1.65$ is the specific weight for quartz submerged in water. Between Eq. B1 and Eq. B2,

$$\dagger_{bf}^* = \frac{H_{bf} S}{R D}. \quad (\text{B. 3})$$

We define dimensionless grain size D^* as (10)

$$D^* = \frac{(Rg)^{1/3}}{\epsilon^{2/3}} D. \quad (\text{B. 4})$$

Figure B.1a shows a plot of \dagger_{bf}^* versus D^* in the form of a Shields diagram (11), with lines indicating the approximate inception of bedload transport and the initiation of significant

suspension. The data have been stratified into five grain size ranges: 0.04 – 0.062 mm (silt), 0.062 – 0.5 mm (very fine to medium sand), 0.5 – 2 mm (coarse to very coarse sand), 2 – 25 mm (fine to coarse gravel) and 25 – 168 mm (coarse gravel to cobbles). The data cover the range from suspended load-dominated rivers to bedload-dominated rivers. The figure shows a consistent trend, with \dagger_{bf}^* decreasing with increasing D^* , that has been noted earlier (12).

Figure B.1b shows a corresponding plot of \dagger_{bf}^* versus bed slope S , with the same grain size discrimination: \dagger_{bf}^* is an increasing function of S through every grain size range. While a tendency for critical Shields number (corresponding to the onset of motion) to increase with S has been reported previously (13, 14), here we demonstrate for the first time this tendency for bankfull Shields number as well.

Figure B.1 suggests the use of similarity collapse to obtain a universal relation for \dagger_{bf}^* as a function of S and D^* . We did this by seeking an exponent m in the relation $\dagger_{bf}^* \sim S^m$, applicable to all grain sizes, and then performing a power regression analysis of \dagger_{bf}^* / S^m versus the D^* . The relation so obtained is $\dagger_{bf}^* = 1223(D^*)^{-1.00} S^{0.534}$, with a coefficient of determination $R^2 = 0.948$, as shown in Fig. B.2. Rounding appropriately,

$$\dagger_{bf}^* = s (D^*)^{-1} S^m, \quad (\text{B. 5})$$

where $s = 1220$ and $m = 0.53$

The value of the exponent of D^* in Eq. B.5, i.e. -1 , has an unexpected consequence. The definition for \ddagger_{bf}^* of Eq. B.2 is such that it varies as D^{-1} , but the right-hand side of Eq. B.5 also varies as D^{-1} . Defining bankfull shear velocity u_{*bf} as

$$u_{*bf} = \left(\frac{\ddagger_{bf}^*}{\dots} \right)^{1/2}, \quad (\text{B. 6})$$

it follows that bed material grain size precisely cancels out in the relation for bankfull shear velocity from Eq. B.2, B.5 and Eq. B.6. With the aid of Eq. B.5, Eq. B.3 can be solved for H_{bf} ; the bed material grain size cancels out again in the relation for bankfull water depth.

The present analysis thus yields a remarkable, and indeed counterintuitive result: bankfull shear velocity and bankfull depth do not depend on the characteristic grain size of the bed material, as shown by the resulting dimensionless relations,

$$\tilde{u}_{*bf} = 35.0 S^{0.26}, \quad \tilde{H}_{bf} = 1220 S^{-0.47}, \quad (\text{B.7a, b})$$

where the dimensionless shear velocity \tilde{u}_{*bf} and depth \tilde{H}_{bf} are

$$\tilde{u}_{*bf} = \frac{u_{*bf}}{(Rg\epsilon)^{1/3}}, \quad \tilde{H}_{bf} = \frac{H_{bf} g^{1/3}}{(R\epsilon)^{2/3}}. \quad (\text{B.8a,b})$$

Equation B.7a and Eq. B.7b, which are compared against the original data set in Fig. B.3a and Fig. B.3b, are of a curious form. Firstly, they specify bankfull shear velocity and bankfull depth independent of characteristic bed grain size across the entire grain size range studied here (0.04 mm – 168 mm). Secondly, they show a dependence on kinematic viscosity across the same grain size range, and across the entire range of flow discharges (0.34 m³/s to 216,000 m³/s).

In so far as Eq. B.2 and Eq. B.5 both depend upon D^{-1} , the absence of grain size dependence in Eq. 8A and Eq. 8B might be the result of spurious correlation. This, however, is not the case. Eq. B.7b defines a relation between two independent dimensionless groupings, i.e. $H_{bf} g^{1/3} (R\epsilon)^{2/3}$ and S . As shown in Fig. B.3b, a direct regression of the data yields a relation that differs little from Eq. B.7b.

The conclusions that bankfull shear velocity and bankfull depth are (to first approximation) independent of grain size and dependent on the kinematic viscosity of water (in addition to slope) fly in the face of a half-century of research on sediment transport dynamics and river morphology. The resolution to the conundrum of kinematic viscosity dependence is likely related to the existence of the floodplain itself. Bankfull depth is not set solely by the characteristic size of the bed material D , but also involves finer material emplaced by floodplain deposition from wash load (15).

There is likely at least one “hidden” variable in the data of Fig. B.2, which gives rise to Eq. B.5, an appropriate candidate being the characteristic size D_w of sediment suspended in the upper layer of the water column that spills onto the floodplain when the river goes overbank. As seen from Fig. B.1, this size is likely to be less than 0.5 mm, and indeed may correspond most closely to wash load. It is thus in a grain size range where fall velocity is a strong function of Reynolds number. More specifically, dimensionless fall velocity $v_w / (RgD_w)$, where v_w is the fall velocity associated with a characteristic diameter of the finer suspended sediment D_w , is related to $D_w^* = (Rg)^{1/3} D_w / \epsilon^{2/3}$ through standard relations for fall velocity (16).

For example, Eq. B.7a can be rewritten as

$$\frac{u_{*bf}}{\sqrt{RgD_w}} = 35.0(D_w^*)^{-1/2} S^{0.26}, \quad (\text{B. 9})$$

thus illustrating how viscosity can enter the problem across scales. Further analysis of this issue is beyond the scope of this contribution, in that sizes D_w are not available for the data set analyzed here.

The characteristic grain size of the bed material D , however, does indeed enter the picture through predictive relations for H_{bf} , B_{bf} , and S as functions of Q_{bf} and Q_{ibf} . Such relations can be derived by augmenting Eq. 5 with a) momentum balance as approximated by Eq. B.1; b) the continuity relations

$$Q_{bf} = U_{bf} H_{bf} B_{bf} \quad , \quad Q_{ibf} = q_{ibf} B_{bf} \quad , \quad (\text{B.10a, b})$$

where U_{bf} is bankfull flow velocity and q_{ibf} is volume bed material transport rate per unit width at bankfull flow; c) the definition of the dimensionless Chezy resistance coefficient C_z :

$$C_z = \frac{U_{bf}}{\sqrt{\tau_{bf} / \dots}} = \frac{U}{u_{*bf}} \quad ; \quad (\text{B.11})$$

d) a specification of C_z ; and e) a predictor for q_{ibf} .

The calculations can be performed for any pair of relations for C_z and q_{ibf} . The case of sand-bed rivers is pursued here because the Engelund-Hansen total bed material load relation (17),

$$q_{ibf} = r_{EH} C_z^2 \sqrt{RgD} D (\dagger_{bf}^*)^{5/2}, \quad r_{EH} = 0.05 \quad (\text{B.12a, b})$$

is accurate for sand transport (18) and allows solution in closed form.

The resistance coefficient C_z is often specified with a set value of Manning's n , but this is not reliable for e.g. rivers dominated by bedform resistance (19). The subset of the data used here corresponding to grain sizes between 0.0625 mm to 2 mm is thus used to find an empirical relation between C_z at bankfull flow and bed slope S . Figure B.4 shows C_z versus S for the entire data set, as well as the regression relation

$$C_z = r_R S^{-n_R} \quad (\text{B.13})$$

where $r_R = 2.53$ and $n_R = 0.19$, determined for the indicated subset.

Three relations for bankfull characteristics of sand-bed streams with characteristic bed size ranging from very fine to medium sand result:

$$\frac{B_{bf}}{D} = \frac{(D^*)^{2.5}}{r_{EH} \sqrt{R} r_R^2 S^{2.5} \left[\frac{RD^*}{r_{EH} r_R S} \right]^{2.5m-2n_R} \left(\frac{Q_{ibf}}{Q_{bf}} \right)^{\frac{2.5m-2n_R}{1+m-n_R}}} \frac{Q_{ibf}}{\sqrt{gD} D^2} \quad (\text{B.14})$$

$$\frac{H_{bf}}{D} = \frac{r_{EH} r_R S^2}{(D^*)^2} \left[\frac{RD^*}{r_{EH} r_R S} \right]^{\frac{2m-n_R}{1+m-n_R}} \left(\frac{Q_{ibf}}{Q_{bf}} \right)^{\frac{2m-n_R}{1+m-n_R}} \frac{Q_{bf}}{Q_{ibf}}, \quad (\text{B.15})$$

$$S = \left[\frac{RD^*}{r_{EH} r_R S} \right]^{\frac{1}{1+m-n_R}} \left(\frac{Q_{ibf}}{Q_{bf}} \right)^{\frac{1}{1+m-n_R}}. \quad (\text{B.16})$$

Evaluating the exponents in the above relations using $m = 0.53$ and $n_r = 0.19$,

$$\begin{aligned}
 B_{bf} &\sim Q_{bf}^{0.71} Q_{tbf}^{0.29} D^{0.29} \\
 H_{bf} &\sim Q_{bf}^{0.35} Q_{tbf}^{-0.35} D^{-0.35} \\
 S &\sim Q_{bf}^{-0.75} Q_{tbf}^{0.75} D^{0.75}
 \end{aligned}
 \tag{B.17 a, b, c}$$

Thus a) bankfull width increases with increasing flood discharge, sand supply and sand size; b) bankfull depth increases with increasing flood discharge, and decreasing sand supply and sand size; and c) slope increases with decreasing flood discharge, and increasing sand supply and sand size. We note that although Eq. B.17c and Fig. B.3 show that slope is dependent on grain size, bankfull shear velocity and bankfull depth remains independent on grain size, as shown in Eq. B.7a, b; Eq. B.8a, b; and Fig B.3.

These relations have a better physical basis than corresponding relations presented elsewhere (5, 7, 8), where e.g. bankfull width increases with increasing flood discharge but is invariant to sand supply. They have been used for a model of co-evolving river width and sinuosity in meandering rivers (20), and can be used as the basis for improved morphodynamic models of channel-floodplain8 or channel-delta co-evolution (9).

References and Notes:

1. L. B. Leopold, T. Maddock, Jr., "The hydraulic geometry of stream channels and some physiographic implications" (Professional Paper 252, U.S. Geological Survey, Washington, DC. 1953).

2. G. Parker, P. Wilcock, C. Paola, W. E. Dietrich, J. Pitlick, Quasi-universal relations for bankfull hydraulic geometry of single-thread gravel-bed rivers. *Journal of Geophysical Research Earth Surface*, **112**(F4), 21 p (2007).
3. G. V. Wilkerson, G. Parker, Physical basis for quasi-universal relationships describing bankfull hydraulic geometry of sand-bed rivers. *Journal of Hydraulic Engineering* **7**(1), 739-753 (2011).
4. C. Paola, P. L. Heller, C. L. Angevine, The large-scale dynamics of grain-size variation in alluvial basins, 1: Theory. *Basin Research* **4**, 73-90 (1992).
5. G. Parker, C. Paola, K. X. Whipple, D. Mohrig, Alluvial fans formed by channelized fluvial and sheet flow. I: Theory. *Journal of Hydraulic Engineering* **124**(10), 985-995 (1998).
6. G. Parker, C. Paola, K. X. Whipple, D. Mohrig, C. M. Toro-Escobar, M. Halverson, T. W. Skoglund, Alluvial fans formed by channelized fluvial and sheet Flow. II: Applications. *Journal of Hydraulic Engineering* **124**(10), 996-1004 (1998).
7. G. Parker, *1D Sediment Transport Morphodynamics with applications To Rivers and Turbidity Currents of Rivers and Turbidity Currents* (E-book, 2004; <http://vtchl.uiuc.edu/people/parkerg/>).
8. G. Parker, T. Muto, Y. Akamatsu, W. E. Dietrich, J. W. Lauer, Unraveling the conundrum of river response to rising sea level: from laboratory to field. Part II. The Fly-Strickland River System, Papua New Guinea. *Sedimentology*, **55**(6), 1657-1688 (2008).
9. W. Kim, D. Mohring, R. Twilley, C. Paola, G. Parker, Is It feasible to build new land in the Mississippi River delta? *EOS* **90**(42), 373-374 (2009).
10. L. C. van Rijn, Sediment transport, Part II: Suspended load transport. *Journal of Hydraulic Engineering* **110**(11), 1613-1641 (1984).

11. G. Parker, in *Sedimentation Engineering processes: Measurements, modeling and practice*, M. H. Garcia, Ed., (ASCE, Reston, VA. 2008) chap. 3, 165-251.
12. W. B. Dade, P. F. Friend, Grain-size, sediment-transport regime, and channel slope in alluvial rivers. *Journal of Geology* **106**, 661-675 (1998).
13. M. P. Lamb, W. E. Dietrich, J. G. Venditti, Is the critical Shields stress for incipient sediment motion dependent on channel-bed slope? *Journal of Geophysical Research* **113**(F02008) (2008).
14. A. Recking, Theoretical development on the effects of changing flow hydraulics on incipient bedload motion. *Water Resources Research* **45**, W04401: 16.doi:10.1029/2008WR006826 (2009).
15. G. Parker, Y. Shimizu, G. V. Wilkerson, E. Eke, J. D. Abad, J. W. Lauer, C. Paola, W. E. Dietrich, V. R. Voller, A new framework for modeling the migration of meandering rivers. *Earth Surface Processes and Landforms* **36**, 70–86 (2011).
16. W. E. Dietrich, Settling velocity of natural particles. *Water Resources Research* **18**(6), 1615-1626 (1982).
17. F. Engelund, E. Hansen, “A Monograph on Sediment Transport in Alluvial Streams” (Technisk Vorlag, Copenhagen, Denmark, 1967)
18. W. R. Brownlie, “Prediction of flow depth and sediment discharge in open channels” (Report No. KH-R-43A, W. M. Keck Laboratory of Hydraulics and Water Resources, California Institute of Technology, Pasadena, California, USA, 1981; <http://caltechkhr.library.caltech.edu/7/01/KH-R-43A.pdf>).
19. R. Ferguson, Time to abandon the Manning equation? *Earth Surface Processes and Landforms* **35**, 1873-1876 (2010).

20. E. C. Eke, thesis, University of Illinois Urbana-Champaign, USA. (2013)

Acknowledgments: The data reported in this paper are presented in (2, 3).

This research was supported by the United States National Science Foundation, through Award Numbers 1209427 (WSC-Category 2) 1135427 (FESD Type I) and DGE 11-44245 (Graduate Research Fellowship Program).

C. Li and M. Czapiga performed the data analysis and derived the equations; E. Eke tested the results; E. Viparelli motivated the analysis and G. Parker provided the concept.

Figures

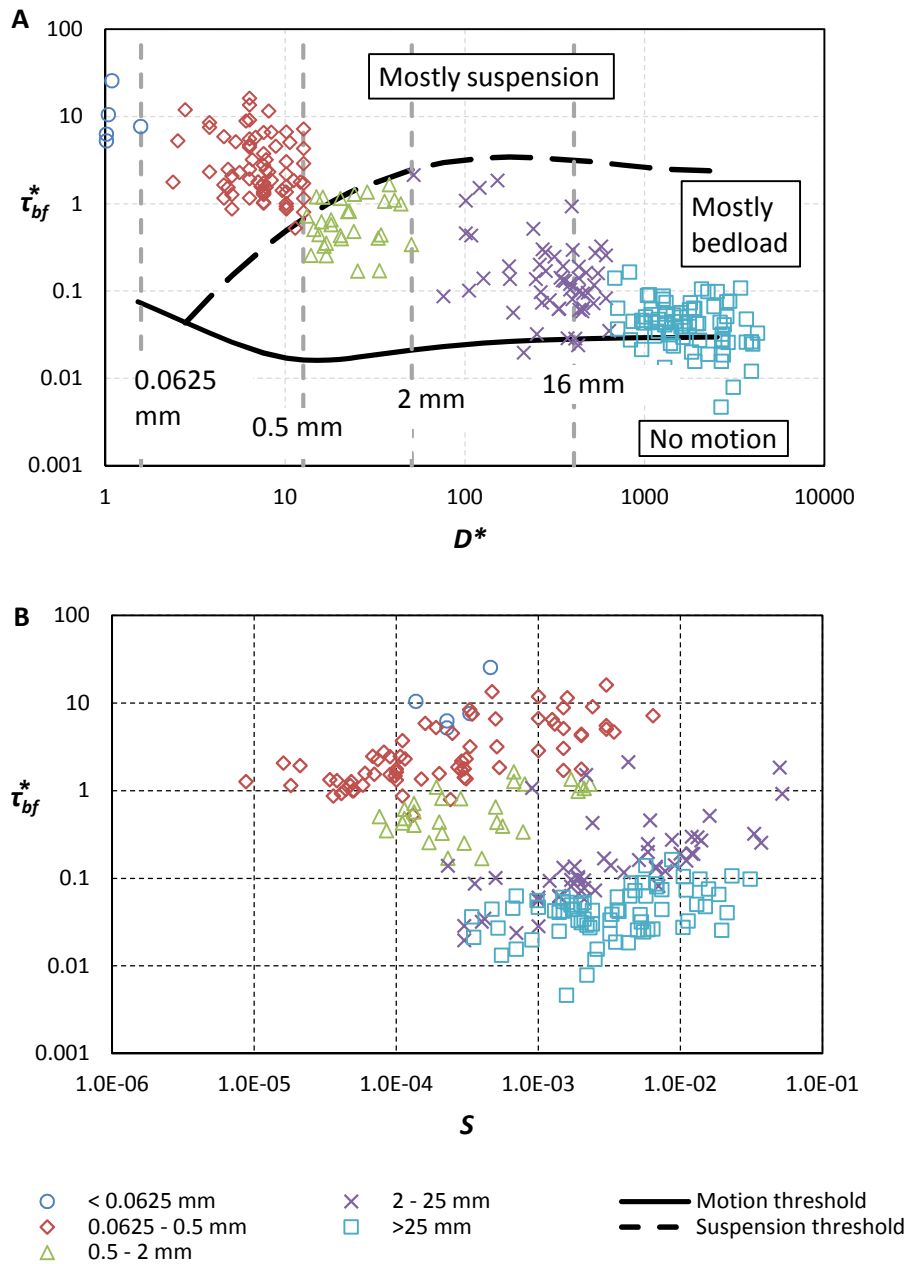


Figure B.1. Bankfull Shields number τ_{bf}^* versus A) dimensionless grain size D^* ; and B) bed slope S for rivers ranging from silt-bed to cobble-bed. The data are stratified into five grain size ranges. Note that τ_{bf}^* increases with slope for every grain size range. Also shown in a) are lines denoting the onset of bed motion and the onset of significant sediment suspension.

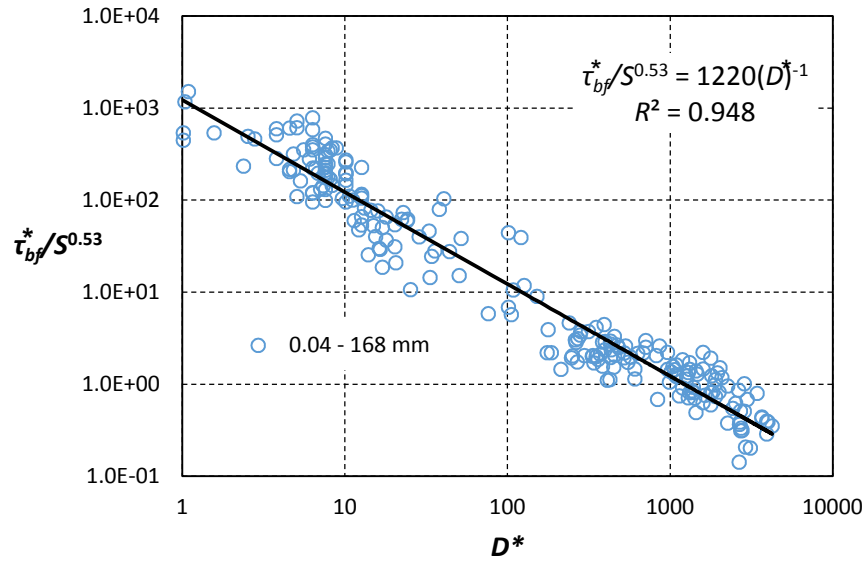


Figure B.2. Similarity collapse for τ_{bf}^*/S^m versus D^* . The regression relation, i.e. Eq. B.5, is shown in the plot.

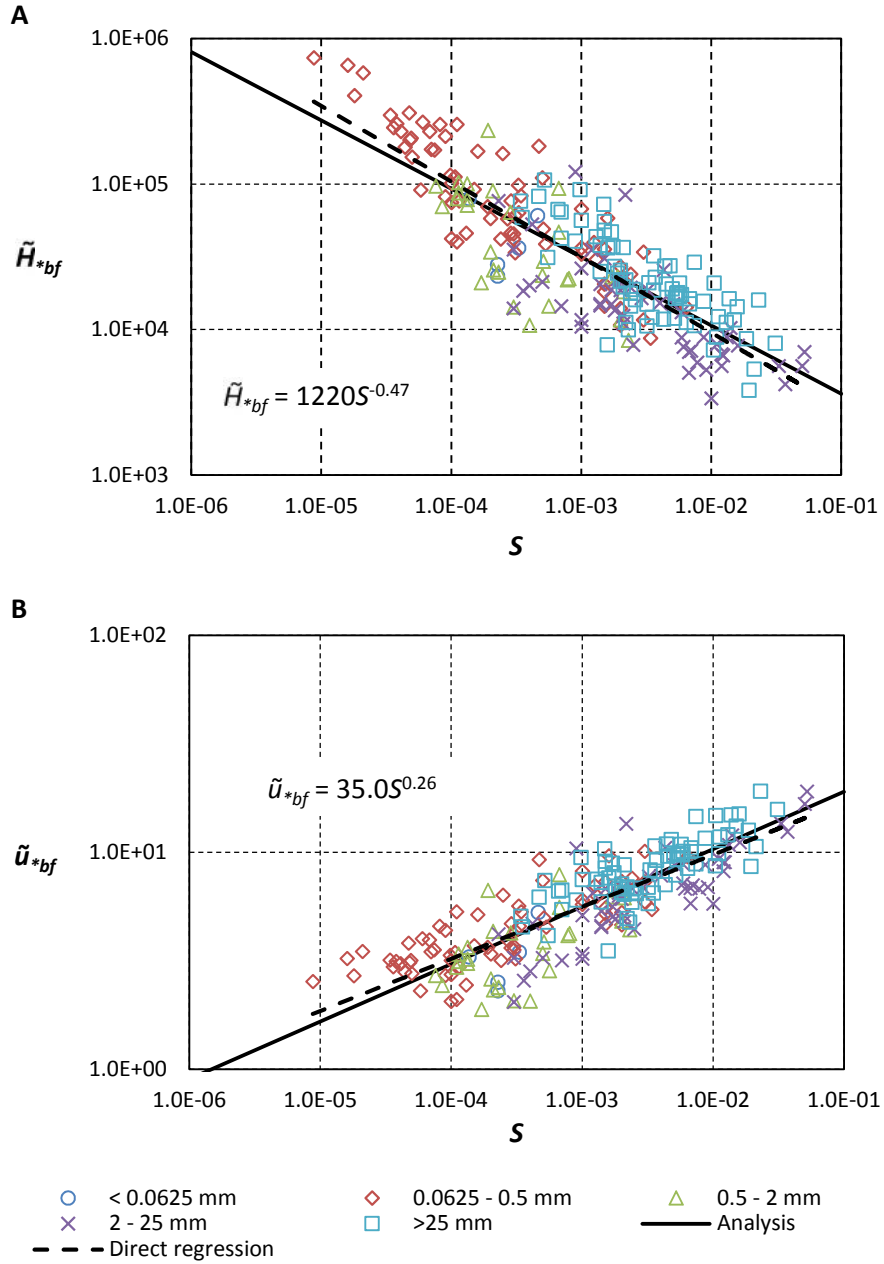


Figure B.3. A) Dimensionless bankfull shear velocity $\tilde{u}_{*bf} = u_{*bf} / (Rg\epsilon)^{1/3}$ and; B) dimensionless bankfull depth

$\tilde{H}_{bf} = H_{bf} g^{1/3} / (Rn)^{2/3}$ versus bed slope. Also included are Eq. B.7A and Eq. B.7B resulting from the regression relation Eq. B.5.

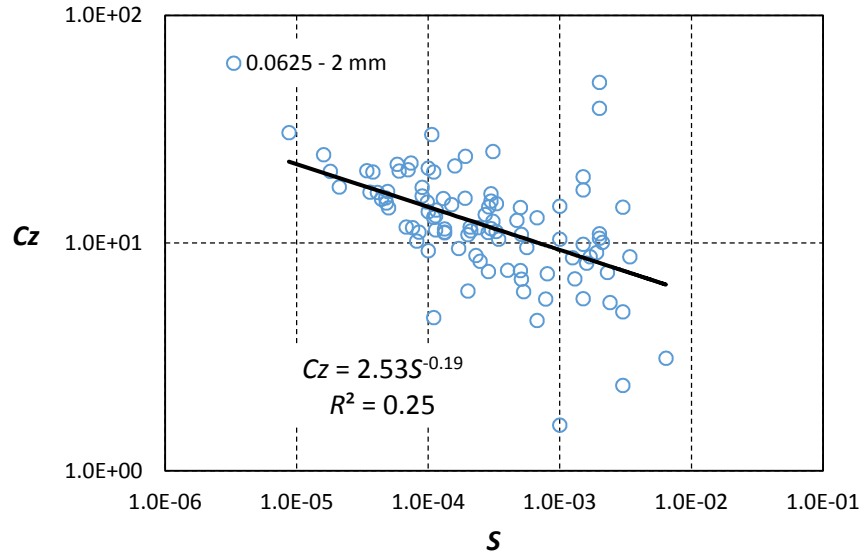


Figure B.4. Plot of dimensionless Chezy resistance coefficient Cz at bankfull flow versus slope S . Data are shown for all five grain size ranges of Fig. B.1 and Fig. B.2. The regression relation shown in the figure, i.e. Eq. B.13, was obtained only using data for $D = 0.0625$ mm to 2 mm, i.e. very fine to medium sand.